# Towards Ultrafast and Ultrasmall

Construction of a THz-STM
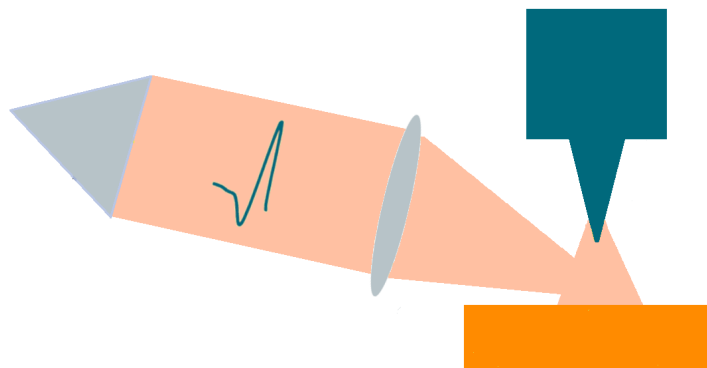
Dissertation

zur Erlangung des Grades eines
Doktors der Naturwissenschaften

am Fachbereich Physik
der Freien Universität Berlin

vorgelegt von
Nils Bogdanoff

Berlin, 2022

Die in dieser Arbeit beschriebenen Experimente wurden in der Arbeitsgruppe von Frau Prof. Dr. Katharina Franke am Fachbereich Physik der Freien Universität Berlin durchgeführt und von ihr betreut.

KURZFASSUNG

Die Kombination hoher räumlicher und zeitlicher Auflösung ist nach wie vor ein limitie-render Faktor bei der experimentellen Erforschung der physikalischer Phänomene an Ober-flächen. Erst vor wenigen Jahren wurde ein neuer vielseitiger Ansatz vorgestellt, der durch Kombination von ultrakurzen Terahertz (THz)-Laserpulsen mit der hohen räumlichen Auflösung der Rastertunnelmikroskopie (STM) entsprechende Beobachtungen ermöglicht: Das sogenannte THz-STM [1]. Hierbei agieren die Laserpulse als ultraschnelle Änderung der Bias-Spannung und ermöglichen so im Rahmen von Pump-Probe Experimenten die Untersuchung ultraschneller lokalisierter Oberflächenprozesse.

Im Rahmen der vorliegenden Arbeit beschreiben wir das Design, den Aufbau und erste Experimente dieses neuartigen Systems in der Arbeitsgruppe. Hierbei diskutieren wir die Neueinrichtung der Laborräume, die konzeptionelle Auslegung und Errichtung der THz-Quelle sowie deren Charakterisierung mittels elektrooptischer Abtastung. Anschließend beschreiben wir die erfolgten Modifikation eines vorbestehenden STMs, die die Einkopp-lung von THz Strahlung ermöglichen.

Das so aufgebaute THz-STM wurde in mehreren Szenarien geprüft und seine Möglichkeiten herausgearbeitet. Hierbei präsentieren wir zunächst Daten basierend auf Photoelektrone-nemission, um die Einkopplung ultrakurzer Pulse zu bestätigen. Anschließende Messungen mit THz-Pulsen an Feldemissionsresonanzen zeigen unter kryogenen Bedingungen und klei-nen Spitze-Probe Abständen eindrucksvoll die Stabilität und Empfindlichkeit des Systems. Experimente unter Verwendung der Kondo-Resonanz von Punktdefekten in MoS_2 Monola-gen belegen die hohe Empfindlichkeit unseres THz-STMs auch bei kleinen Nichtlinearitäten und zeigen beispielhaft erste ortsaufgelöste Daten. Abschließend stellen wir, im Rahmen eines Ausblicks, vorläufige Ergebnisse zu zeitaufgelösten Prozessen unter Nutzung unseres neuen THz-STMs vor.

ABSTRACT

The combination of high spatial and temporal resolution is still a limiting factor in the field of surface science. Only very recently, a novel experimental approach has been presented that allows versatile access to this regime by combining ultrafast Terahertz (THz) pulses with the extraordinary spatial resolution of scanning tunneling microscopy (STM): The so-called THz-STM [1]. In this device, the THz pulses act as ultrafast transient bias voltage and hence allow to unravel the ultrafast physics of highly localized electronic states via pump-probe experiments.

In this thesis, we describe the process of establishing this novel technique in our group. We firstly discuss the new configuration of the designated lab, the design and alignment of our THz-source as well as its characterization using electro-optic sampling. Subsequently we describe the modifications performed on the preexisting STM to facilitate the coupling of THz radiation.
The THz-STM was thoroughly tested in different scenarios showcasing its capabilities. We initially present data originating from optical-pump, THz-probe measurements based on photoelectron emission, confirming the successful coupling of ultrashort THz pulses into the STM. Subsequent measurements using field emission resonances show the stability of our system under cryo conditions and using junctions at tunneling distances. Experiments involving Kondo resonances of point defects in MoS_2 prove the sensitivity of our THz-STM when used with small nonlinearities and are used to perform exemplary spatially resolved measurements. Finally we present preliminary time-resolved data as part of an outlook.

CONTENTS

CHAPTER 1

INTRODUCTION

Objectifying the world around us by reproducible measurements is at the core of natural science. Especially observing and understanding what can not be perceived directly by our natural senses has always been intriguing. For example, time measurements in form of calendars based on astronomical observations have been performed for many thousand years [2, 3] and were of high practical relevance e.g. in agriculture [3] . With the advances of technology, different kind of clocks got more and more precise. With every leap in precision they enabled potential advances in practical fields, such as revolutionizing navigation in the form of Harrison's clock [4], but also in every fundamental scientific experiment that includes a temporal component, which can be as simple as linear mechanical motion. The ultrafast timescales accessible today via modern laser physics, revolutionized the way we perform physical experiments. While the measurement of time had and has very practical implications on daily life, another question remained more philosophical for a long time: The fundamental structure of matter.

Although the first known idea of elementary particles tracks back to ancient Greek times when Leucippus and his student Democrictus proposed the non-dividable atoms [5, 6], their length scale remained out of experimental reach for thousands of years. In more modern times, different observations, such as chemical stoichiometry or spectral emission lines validated and improved the atomic theory [6]. Other experiments, for example crystal symmetry or reciprocal space techniques such as X-ray diffraction, helped disentangle how those atoms form the condensed matter around us [7]. But directly accessing the atomic length scale on extended condensed matter surfaces was impossible until 1981. In this year, Gerd Binning and Heinrich Rohrer presented a new technique that earned them a Nobel Prize only five years later: scanning tunneling microscopy (STM) [8]. This microscope allowed to routinely access electronic properties on conducting surfaces in real-space with atomic-scale resolution. In the following years it spawned a variety of other similar scanning

1

probe techniques for different sample types and questions and hence greatly enabled the field of modern nanosciences.

Combining these two major areas of extraordinary temporal and spatial resolution is hence a promising, albeit challenging, step towards further understanding of condensed matter physics. Many approaches have been taken in this direction in order to investigate different kinds of systems. In the area of electronic surface science, efforts have been taken to couple laser pulses to an STM already shortly after its invention in the hope of combining their high temporal and spatial resolution. For example, photoconductive switches have been added to STM samples [9–11] and direct illumination with laser pulse trains has been attempted [10, 12]. Albeit undeniably pushing the limits in STM time resolution, these approaches suffered from problems with thermal load, restrictive sample requirements [10, 13, 14] and being difficult to interpret. Only very recently a new and encouraging temporal extension of STM emerged that is fundamentally avoiding many of these problems: The so-called THz-STM has been shown to be able to access ultrafast timescales with atomic-scale resolution [1] in a versatile way by coupling Terahertz (THz) radiation into a STM junction. In this thesis we will present our take on constructing and operating such a novel measurement system.

CHAPTER 2

THEORETICAL AND EXPERIMENTAL BACKGROUND

In order to understand the principle of THz-STM and the process of setting up one in our lab, some theoretical fundamentals need to be discussed. Since knowledge from two very different fields, STM and laser physics, is required, this chapter will individually cover the basics of both.

2.1 Scanning Tunneling Microscopy

Scanning Tunneling Microscopy [8] is a surface-sensitive technique to analyze conducting condensed matter samples. In contrast to many other surface science techniques such as angle-resolved photoemission spectroscopy (ARPES), low-energy electron diffraction (LEED) or X-ray photoelectron spectroscopy (XPS), the Scanning Tunneling Microscope (STM) operates in real space and is hence able to measure highly local, non-periodic features. It operates based on the quantum mechanical tunneling effect.

2.1.1 Quantum Tunneling

In order to understand the working principle of STM, one first needs to understand the underlying quantum mechanical tunneling effect. Classically, dealing with a particle encountering an energy barrier, e.g. a charged particle encountering an electric field, is simple: If the particles energy is greater than the energy of the barrier, it can overcome the barrier. Otherwise it can not penetrate and will e.g. be elastically reflected.

In quantum mechanics, this is a bit more complicated since we need to treat the question if a particle can penetrate a potential barrier in terms of quantum mechanical probability densities. In order to understand the principle, we do not need a full derivation at this point and will only follow a heuristic argument to motivate the tunneling effect. The fol-

lowing motivation is loosely based on [15].

Lets imagine a particle of mass m in 1D in presence of a potential step. The stationary Schroedinger equation of such a particle would read

$$\hat{H}\Psi(x) = E\Psi(x) \Rightarrow \frac{\hbar^2}{2m}\frac{\partial^2}{\partial x^2}\Psi(x) + (E - V)\Psi(x) = 0, \tag{2.1}$$

where our potential energy is represented by

$$V(x) = \begin{cases} 0 & x < 0 \\ V & x \geq 0 \end{cases}. \tag{2.2}$$

We can directly see from the fact that the double derivative of $\Psi(x)$ again yields something proportional to $\Psi(x)$ that an exponential ansatz is promising. Using $\Psi_A = e^{ikx}$ in eq. 2.1 we get

$$-\frac{\hbar^2 k^2}{2m}\Psi_A(x) + (E - V)\Psi_A(x) = 0. \tag{2.3}$$

So we see that our ansatz is a good starting point for a solution with

$$k = \sqrt{\frac{2m}{\hbar^2}(E - V)}. \tag{2.4}$$

Lets first look a $x < 0$, where $V = 0$. We can now easily construct a more general solution from our ansatz and find

$$\Psi_{x<0}(x) = Ae^{ik_{x<0}x} + Be^{-ik_{x<0}x}. \tag{2.5}$$

In this area we easily find from eq. 2.4 that $k_{x<0} = \sqrt{\frac{2m}{\hbar^2}E} > 0$ since $E, m > 0$. This can be interpreted as two planes waves traveling in different x-directions, albeit we omitted time-dependence earlier. So there is a component associated with the incoming wave/particle (amplitude A) and one for the one reflected on the potential (amplitude B).

We can now proceed to look which solutions are available for $x \geq 0$. If $V < E$ we can basically follow the same argument as before, just with a different numerical value for k, and see that the particle can proceed to travel freely.

Up until here no cases emerged that would not have been possible classically. But if we now have a look at the solutions for $V < E$, there is a surprise. Since $(E - V)$ is now negative in eq. 2.4 we find $k_{x\geq0} = i\sqrt{\frac{2m}{\hbar^2}(|V - E|)}$ to be imaginary. The ansatz 2.5 would in this case hence lead to

$$\Psi_{x<0}(x) = Ae^{-|k_{x\geq0}|x}, \tag{2.6}$$

where we set $B = 0$ to fulfill the normalizability condition of wavefunctions. We see there is a finite amplitude and hence probability density to find the particle inside the classically forbidden area, which decays exponentially with penetration depth. We could now start

calculating the coefficient from boundary conditions, but since their value is not relevant for the general understanding, we will forgo to do so.

It is now easy to imagine what happens if we choose the potential barrier to be of finite width in space: Since there is a component of the wavefunction decaying into the forbidden area, there is also a finite probability that the particle leaves the potential on the other side and can continue to travel freely (fig. 2.1). This possibility of particles to *tunnel* through an otherwise energetically forbidden area is called *quantum mechanical tunneling effect*. Since, as motivated in eq. 2.6, the decay of the wavefunction is exponential inside the potential area exponential, the amplitude of particles passing through the barrier is not only dependent on the potential height and the particle mass, but also exponentially dependent on the barrier width. Only very thin barriers hence offer the possibility to tunnel through.
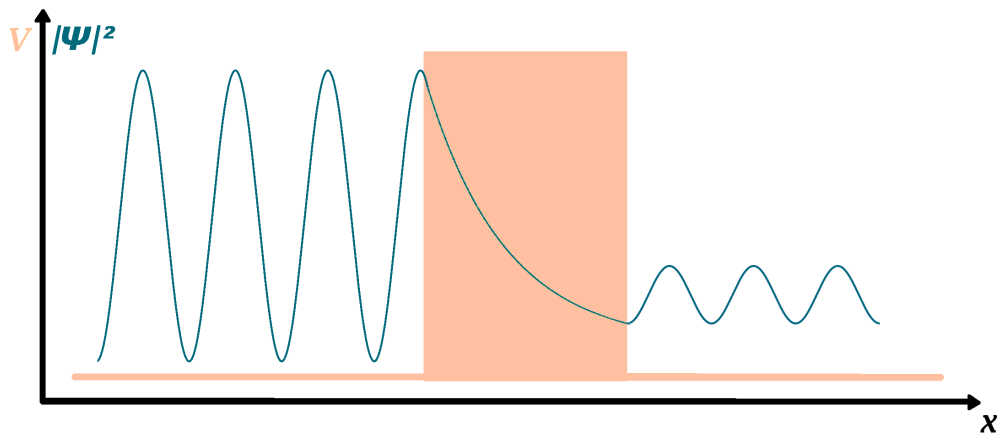
Figure 2.1: A wavefunction encountering a potential barrier (indicated by orange box). Quantum mechanics allows an evanescent state inside the barrier, leaving a finite possibility for incoming particles to pass the classically forbidden region. This phenomenon is called *quantum mechanical tunneling effect.*

2.1.2   Working Principle

Scanning Tunneling Microscopy is based on the aforementioned tunneling effect. A thin conducting needle, called *tip* is brought into close proximity of a conducting sample surface without touching it (fig. 2.2). Electrons can now tunnel between tip and sample and a so called *tunneling current* will start to flow. As motivated in sec. 2.1.1, this current is ex-

ponentially dependent on the tip sample distance. It is therefore highly sensitive to height changes and enables STM to routinely resolve differences on sub-atomic length scales. In order to generate an extended image of the surface, the tip needs to be moved over the surface with high precision. This is realized with piezoelectric actuators. This scanning motion of the tip is giving the STM the first part of its name. Another piezo in z-direction allows for precise adjustments of the tip-sample distance.
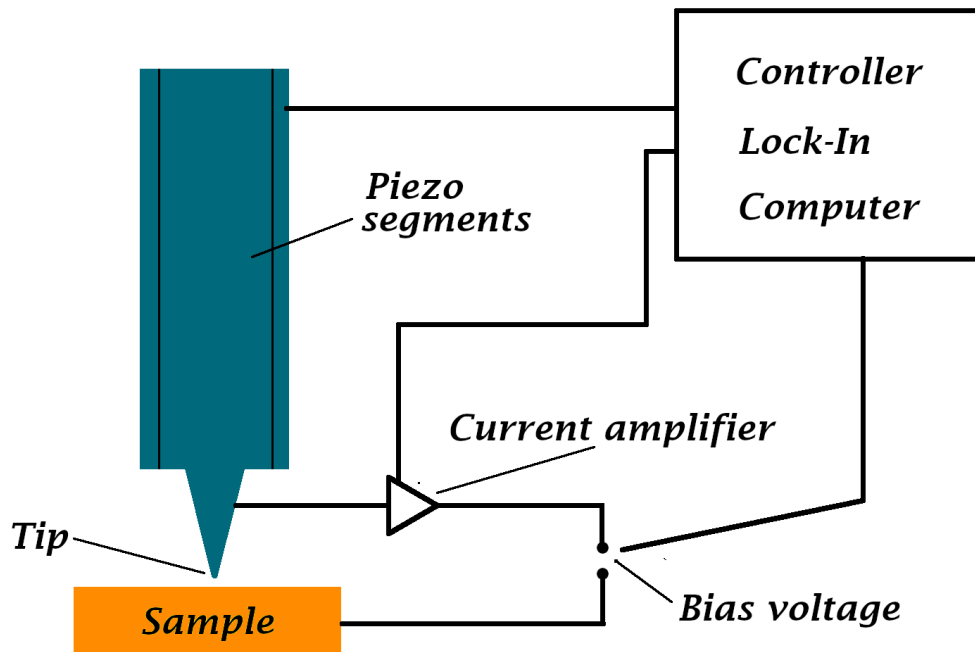
Figure 2.2: Schematics of a scanning tunneling microscope. A small tip, freely movable using piezoelectric elements, is brought into close proximity of a conducting sample. When applying a bias voltage, the tunneling effect allows a small current to flow. This current is detected using a current amplifier. A measurement computer and feedback loop control the experiment. Figure adopted from [16]

There are mainly two different ways how to scan the tip for image generation: Constant-current and constant-height mode (fig. 2.3).

Constant-height mode is in some sense the straightforward way of doing so. The z-position of the tip is kept constant during scanning and the tunneling current, which contains the
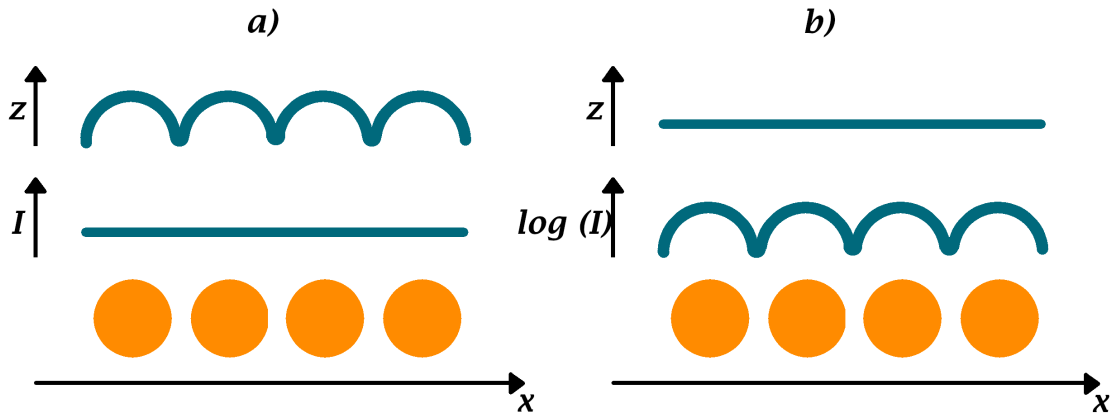
Figure 2.3: Two different scanning approaches are typically used in STM: In constant current mode (**a**), a feedback loop modifies the tip height (z) to keep the current (I) constant. The signal is then read from the z-channel. In constant height mode (**b**), the tip is kept at constant z and the current is being recorded. Figure adopted from [16].

height information, is being recorded. This has the advantage of being very simple in execution and hence not convolving the measurement with additional error sources. The speed of the measurement is essentially only limited by the necessary averaging time to beat the noise level, the ramp speed supported by the piezos and the amplifier bandwidth. There are several disadvantages to this technique though. Due to the strong dependence of tunneling current and distance, there is only a small area which allows for small enough currents to not damage the tip and still deliver a signal. Hence, if the sample is not nearly perfectly flat, there will be either areas without signal or one risks crashing the tip into the sample if being too close. Another problem is the assumption of a constant tip position: Piezo creep, mechanical vibrations and thermal drift change the tip height over time and are not corrected for in constant-height mode.

In contrast, constant-current mode takes care of many of these problems. A feedback loop, using a proportional-integral (PI) controller, constantly adjusts the z-piezo in order to keep the tunneling current constant. In this case, the recorded z-channel contains the signal being directly readable as a quasi-topographic map of the sample. It makes it possible to scan rougher surfaces without crashing or loosing signal. On the downside, the small bandwidth of the feedback loop greatly reduces the possible scan speed. In this thesis, topography measurements are mostly performed in constant-current mode.

2.1.3 Physics of Scanning Tunneling Microscopy

In sec. 2.1.1 we effectively looked at tunneling between areas of free electrons separated by a barrier. In an STM tip and sample are conductive condensed matter systems imposing many restrictions on the available electronic states. Additionally, in contrast to the macroscopic world, on a microscopic level the notion of topography or even tip-sample distance is less clear. We hence need to clarify a bit more how the signals measured by an STM actually arise.

A well known approach to write the STM tunneling current has been justified by J. Bardeen [17–19]. He based his Hamilton operator on the assumption of non-interacting tip and sample states as well as a single particle hopping Hamiltonian as interaction. Without going into the details, following this approach leads to the well known result of Fermis golden rule [20, 21] with which we can as well start here:

$$\lambda_{\mu \to v} = \frac{2\pi}{\hbar} |M_{\mu \to v}|^2 \delta(E_\mu - E_v). \tag{2.7}$$

Here, $\lambda_{\mu \to v}$ is the transition rate for electrons between the μ and v state of tip and sample. The tunneling matrix element $M_{\mu \to v} = \langle \Psi_\mu | \hat{V} | \Psi_v \rangle$ is given by the mixing of tip and sample states due to the scattering potential of the hopping theory in the Bardeen approach. We can easily see, that tunneling will only happen if tip and sample states align in energy. Those processes are hence called elastic tunneling.

From this we can easily find a resulting net current by multiplying with the elementary charge and integrating over all available states for both tunneling directions [22]:

$$I(V) = \frac{4\pi e}{\hbar} \int_{-\infty}^{\infty} (f(E_F + \epsilon) - f(E_F - eV + \epsilon))$$
$$\cdot \rho_S(E_F + \epsilon)\rho_T(E_F - eV + \epsilon) |M_\epsilon|^2 \, d\epsilon. \tag{2.8}$$

Here, $\rho_{S/T}$ is the density of states (DoS) of sample and tip, $f(E)$ is the Fermi-Dirac distribution, E_F is the Fermi energy and V is the applied voltage between tip and sample. We assumed that there is an effective energy dependent value M_ϵ for the state-dependent transition matrix elements $M_{\mu \to v}$

For further simplification, some experimental assumptions can be made. If the temperature is low, as it is typically the case in STM, the Fermi-Dirac distribution approaches a simple Θ-step function. For those cases eq. 2.8 reduces to [22]

$$I(V) = \frac{4\pi e}{\hbar} \int_0^{eV} \rho_S(E_F + \epsilon)\rho_T(E_F - eV + \epsilon) |M_\epsilon|^2 \, d\epsilon. \tag{2.9}$$

While this is already very instructive in showing the characteristics of the tunneling current, it is of limited use when interpreting STM images due to the unknown values and dependencies of M. Ab initio calculations of the complex tip and sample system to evaluate this transition matrix would be extremely demanding.

Tersoff and Hamann [18, 21] proposed a simplification avoiding this problem. Their approach assumes that on a STM tip only the lowest atom contributes meaningfully to the overall tunneling current. This is justified due to the strong exponential z-dependence of tunneling. Furthermore they assume this atom is contributing only with an s-orbital. Lastly, the wavefunction of a flat metallic surface can be expanded in terms of Bloch waves. Using these wavefunctions to determine M, plugging it into eq. 2.7 before integration and assuming voltages small enough that the density of states around the Fermi level looks constant, we find [23]

$$I(V) \propto V \rho_S(z, E_F) \approx V \rho_S(0, E_F) e^{-2\kappa z}. \tag{2.10}$$

Here, $\rho_S(r, E)$ is the local density of states (LDOS) at distance r and energy E, $r = z$ is the position of the tip, $r = 0$ is directly at the surface and E_F is the Fermi energy. The decay constant of the sample states into the vacuum is $\kappa = \frac{\sqrt{2m\Phi}}{\hbar}$, Φ being the work function of the sample.

This result finally allows us to understand images generated by low-bias STM scans. Beside the exponential height dependence, the LDOS of the sample at Fermi energy contributes to the measured tunneling current. Depending on the tip sample distance changes in the LDOS might be a considerable factor beside topography in the generated lateral contrast. Hence STM images need to be interpreted very carefully.

2.1.4 Scanning Tunneling Spectroscopy

While imaging the aforementioned quasi-topography at the atomic scale is fascinating in itself and helps understanding sample structures and defects, it carries little quantifiable information about the electronic structure and hence behavior of the examined systems. There is a way to gather data about the local electronic structure though: Scanning tunneling spectroscopy (STS), a technique performed with the same measurement setup and hence going hand in hand with STM.

We have already seen in eq. 2.9 that the tunneling current is related to the electronic DoS of tip and sample (see fig. 2.4). But the integral makes it difficult to extract the sample DoS from a measurement. In order to make this more accessible, we need to get rid of the integral and hence take the derivative of eq. 2.9 [23] . Using Leibniz integral rule we arrive at

$$\begin{aligned}
\frac{dI}{dV}(V) \propto\ & \rho_T(E_F)\rho_S(E_F + eV)\left|M_{eV}\right|^2 \\
& + \int_0^{eV} \rho_S(E_F + \epsilon)\rho_T(E_F - eV + \epsilon)\frac{d\left|M_\epsilon\right|^2}{dV}d\epsilon \\
& - e\int_0^{eV} \rho_S(E_F + \epsilon)\frac{d\rho_T(E_F - eV + \epsilon)}{dV}\left|M_\epsilon\right|^2 d\epsilon.
\end{aligned} \tag{2.11}$$

9
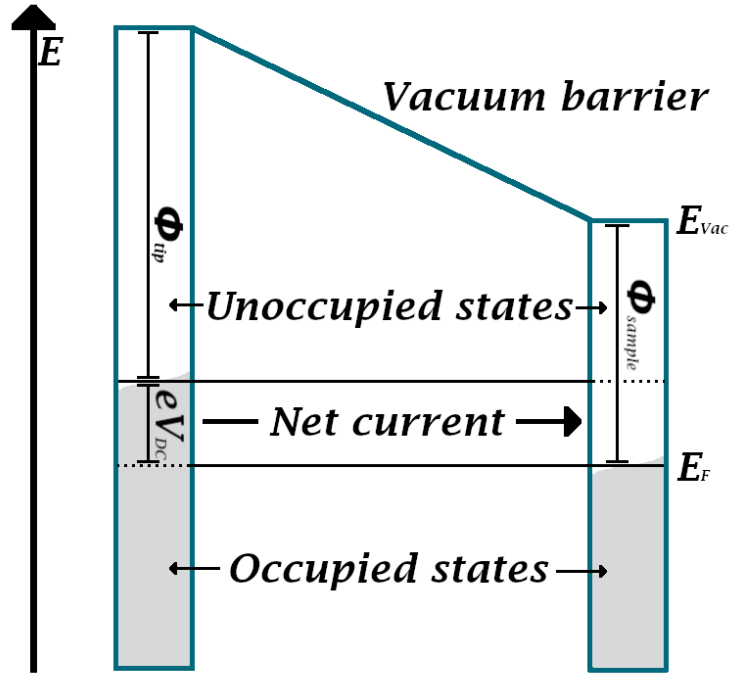
Figure 2.4: Schematic energy diagram of a STM junction. A triangular interpolation between the work functions (Φ) of tip and sample approximates the vacuum barrier between the leads. While tunneling can occur between all energetically aligned states, a net electron current will only flow from occupied to unoccupied states. Such an occupation difference can e.g. be generated by biasing the tunneling junction with a voltage V.

Assuming that M is independent of V [23], the second term of the sum can be dropped. This is sensible since we do not change the tip position and the overlap of the tip and sample wavefunctions should in first order not depend strongly on the perturbing electrical field for small voltages.

Secondly we assume that the DoS of the tip is nearly constant, which is a good approximation for metallic tips, and can drop the last integral. This leaves us only with the first term, which does not contain a convolution anymore [23]:

$$\frac{dI}{dV}(V) \propto \rho_S(E_F + eV). \tag{2.12}$$

This is equation is at the core of STS. By sweeping the bias and deriving the measured

tunneling current around Fermi at a constant tip height, we can easily unravel the local distribution of electronic states of the sample. These so called dI/dV-spectra can e.g. be used to find how defects produce local bound states or how the orbitals of adsorbed molecules change depending on their surroundings.

2.1.5   Lock-In Amplifier

Scanning tunneling spectroscopy is performed at extremely low currents of a few picoamp. Hence techniques for the reduction of noise need to be applied. Beside different design approaches and filter to reduce mechanical and electronic noise in the microscope (see sec. 3.2) a lock-in amplifier can be used. This device is used to extract signals with a small bandwidth around a given frequency and neglect all other contributions.
Technically a lock-in amplifier (fig. 2.5) consists of a frequency mixer and a low pass filter [24, 25]. A measurement signal with frequency f_m and a reference signal with f_r get mixed and (having the same phase) produce signals with sum frequency $f_r + f_m$ and difference frequency $f_r - f_m$. If we now apply a low-pass filter strict enough to cut off all sum frequencies (cut-off frequency $< f_r$) only the difference frequencies $f_r - f_m$ remain. We now easily see that we get a DC response if and only if $f_r = f_m$ [25, 26]. By tuning the low-pass filters cut-off frequency we we can configure how small the resulting effective bandpass around f_r is. A perfect DC-filter would result in only signals with exactly f_m passing. Beside not being possible from a technical viewpoint, a certain bandwidth is desirable: Usually a measurement consists of more than one data point resulting in a desired change with the frequency of the experimental change of input parameters. Therefore the strictness of noise rejection and the temporal response of a lock-in amplifier are in trade-off and parameters need to be chosen carefully.

In STS, lock-in amplification is used by modulating the bias voltage with a sinusoidal signal of small amplitude. Since the tunneling current is a function of the bias voltage, the modulation gets imprinted on the measured signal. We can quantify this by using a Taylor expansion assuming the modulation amplitude is small:

$$I\left(V + V_r * sin(2\pi f_r t)\right) \approx I(V) + \frac{dI}{dV}(V)V_r sin(2\pi f_r t). \tag{2.13}$$

We see that the resulting component of frequency f_r that will be picked up by the lock-in amplifier is of amplitude $\frac{dI}{dV}(V)V_r$. Remembering eq. 2.12 we see that the lock-in amplifier signal is directly proportional to the desired DoS of the sample. Beside noise rejection, this intrinsic calculation of the derivative is a nice extra benefit of applying lock-in techniques in STS.
In the last sections, we have discussed some fundamental aspects of STM/STS. Combined with the following segment, concerning the optical parts of the experiments, it lays the basis for understanding the experiments performed in this thesis.
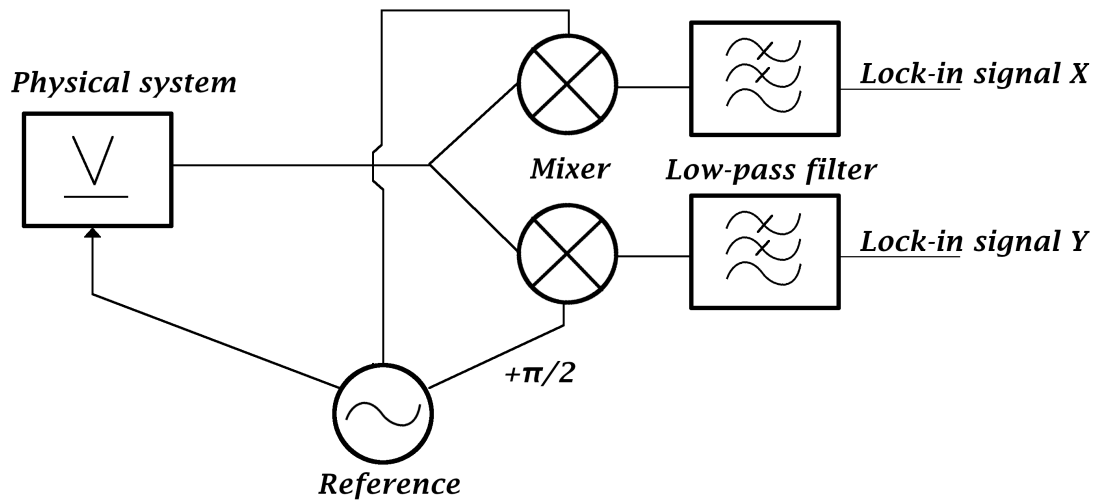
Figure 2.5: A lock-in amplifier can be used to effectively reject noise. A reference signal gets imprinted on a system. Using a frequency mixer and a low-pass filter, the lock-in can filter for signals aligned in frequency and phase to the reference. Hereby all other unwanted components get rejected and the signal to noise ratio increases strongly. Figure inspired by [25]

2.2 Light, Optics and Lasers

As hinted at before, experimental insight can be driven via high spatial resolution, but also by increased time resolution. While there was a huge step from measuring with mechanical clocks to electronic timekeeping, the maximum time resolution achievable by measurements with electronic circuits is not without limit. Due to e.g. stray capacitance, Inductance and wire ends the bandwidth of cables is limited and they tend to work as an antenna at a given point. Overall even dedicated electronics will usually not be able to resolve signals that are well below the nanosecond range [11]. While this is extremely fast and sufficient for many macroscopic applications, when examining on the atomic length scale as done with STM this is rather slow. Chemical reactions [27], lattice [28] and molecular vibrations [29] or spin flips [30] are examples for microscopic phenomena that can occur on timescales of few picoseconds down to the attosecond regime.

In order to resolve processes occurring on these ultrafast timescales, the measurement system needs to be at least equally fast. Physically, the fastest possible phenomena is light. Its speed, the so called speed of light, is limited to about $c = 3 \cdot 10^8 \frac{m}{s}$ according to the theory of relativity and can generally speaking not be surpassed. Therefore in modern ultrafast physics experiments, light is used as a measurement tool to achieve the desired temporal resolution. In order to understand how this is done and how it is used in this thesis, some fundamentals need to be clarified first.

2.2.1 Light as electromagnetic waves

While light and optics have been of scientific interest (e.g. for magnifying devices) for a very long time, it took until the 19th century for James Clerk Maxwell to realize that light is an electromagnetic wave [31] and describe those with a theory consisting of four equations the so called Maxwell equations [32]:

$$\boldsymbol{\nabla} \times \vec{E} = -\frac{\partial \vec{B}}{\partial t},$$
(2.14)

$$\boldsymbol{\nabla} \times \vec{B} = \mu_0 \vec{j} + \frac{1}{c^2}\frac{\partial \vec{E}}{\partial t},$$
(2.15)

$$\boldsymbol{\nabla} \cdot \vec{E} = \frac{\rho}{\epsilon_0},$$
(2.16)

$$\boldsymbol{\nabla} \cdot \vec{B} = 0.$$
(2.17)

In these equations, $\vec{E}$ is the electric field, $\vec{B}$ is the magnetic flux density, μ_0 is the magnetic vacuum permeability, $\vec{j}$ is the displacement current, ρ is the charge density and ϵ_0 is the dielectric vacuum permittivity. In combination with the Lorentz force, they describe

classical electrodynamics entirely.

As mentioned, light is not an electrostatic phenomenon, but classically best described by an electromagnetic transversal wave. To further understand what this description implies, we hence best start by taking the rotation of eq. 2.14 and inserting 2.15:

$$\boldsymbol{\nabla} \times \boldsymbol{\nabla} \times \vec{E} = \boldsymbol{\nabla} \times \left(-\frac{\partial \vec{B}}{\partial t} \right)$$

$$\boldsymbol{\nabla} \times \boldsymbol{\nabla} \times \vec{E} = -\frac{\partial}{\partial t} \left(\mu_0 \vec{j} + \frac{1}{c^2} \frac{\partial \vec{E}}{\partial t} \right). \tag{2.18}$$

Using the well known identity for double curl $\boldsymbol{\nabla} \times \boldsymbol{\nabla} \times \vec{a} = \boldsymbol{\nabla}\boldsymbol{\nabla} \cdot \vec{a} - \Delta\vec{a}$ as well as eq. 2.16 and restricting ourselves to electric fields in vacuum, meaning $\vec{j}{=}0$ and $\rho = 0$, we find a fundamental equation relating temporal and spatial derivatives of electric fields:

$$\Delta\vec{E} = \frac{1}{c^2} \frac{\partial \vec{E}}{\partial t}. \tag{2.19}$$

For solutions of the electric field, the corresponding perpendicular magnetic component of electromagnetic waves can then be calculated via eq. 2.14.

An important set of solutions useful for describing light are the periodic plane waves. They are restricted to traveling in one plane in space and are oscillating periodically with a frequency f:

$$\vec{E} = \vec{E_0}cos(\vec{k} \cdot \vec{r} - \omega t). \tag{2.20}$$

Here, $|k| = \frac{2\pi}{\lambda}$ is the wavevector pointing along the propagation direction with $\vec{E_0} \cdot \vec{k} = 0$ and $\omega = 2\pi f$ is the angular frequency of the field oscillation at a given point in space. The quantity λ is the wavelength. Wavelength and frequency are fundamentally related by the speed of light:

$$c = \lambda f \tag{2.21}$$

The wavelength/frequency has an important impact on our daily real-life contact with light: The different wavelengths is what we perceive as colors in the narrow range of frequencies our eyes are able to detect (2.6).

Up until here we only discussed electromagnetic fields in vacuum. Since this is largely untrue for the planned setup, we will give a quick remark on the interaction with matter [33]: When an electric field is present in matter with non-free charges (dielectric material), those charges can be separated and lead to a polarization $\vec{P}$ of the material. The overall flux density is then given by the dielectric displacement

$$\vec{D} = \epsilon_0\vec{E} + \vec{P}. \tag{2.22}$$

14
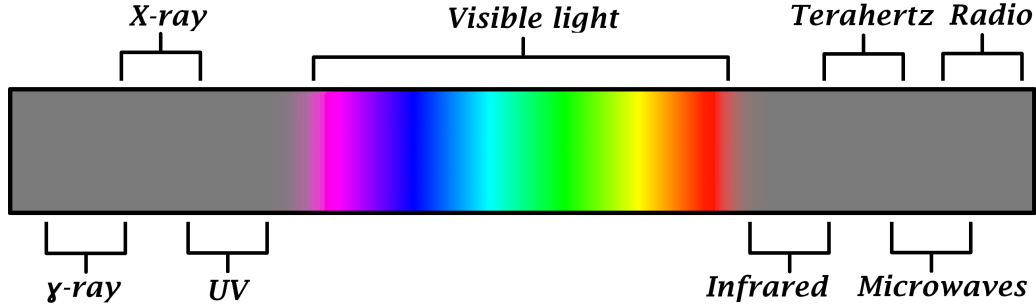
Figure 2.6: Many different phenomena are in fact electromagnetic fields oscillating at different frequencies. Light falls in the region between the more energetic x-rays and the micro-/ and radio waves at lower energies. The THz radiation used in this thesis can be found between infrared light and microwaves. Figure not to scale.

In case of a linear, isotropic response, which can be usually assumed for small enough fields, the polarization can be described by

$$\vec{P} = \epsilon_0 \chi_e \vec{E} \tag{2.23}$$

. Here χ_e is the dielectric susceptibility. For convenience, it is common to define the relative permittivity $\epsilon_r = 1 + \chi_e$ simplifying eq. 2.22 to $\vec{D} = \epsilon_r \epsilon_o \vec{E}$.

Likewise, a magnetic field can introduce a magnetization $\vec{M}$ resulting in the relation $\vec{B} = \mu_0 \left(\vec{H} + \vec{M} \right)$ between magnetic field $\vec{H}$ and flux density $\vec{B}$ [34].

To conclude, in this chapter we introduced the electromagnetic wave model of light that will be a crucial basis in the following chapters.

2.2.2 Polarization

A fundamental property of light is its polarization. In section 2.2.1 we already discussed how light can be described as a transverse electromagnetic plane wave, hence with the oscillation direction of the electric (and magnetic) field perpendicular to the direction of propagation. However, in a 3D space, this only restricts the oscillation direction to a plane and hence leaves another degree of freedom. It is filled by stating the direction of the E-field direction, which is then called polarization direction and the light is called linearly polarized. Albeit human eyes are not able to resolve this direction, it is not a mere necessity for accurate mathematical description, but bears plenty of physical relevance. One example is the polarization dependent reflectivity of dielectrics like glass (see e.g. Brewster angle), another one is the different behavior when light encounters systems with non-isotropic charge mobility.

An artificially engineered example of such a polarization dependent optical element is a wire grid polarizer. It consists of an array of many thin metallic wires arranged parallelly in a plane (fig. 2.7). When an electromagnetic wave propagates through such a device, the electric field will move the charge carriers if possible.
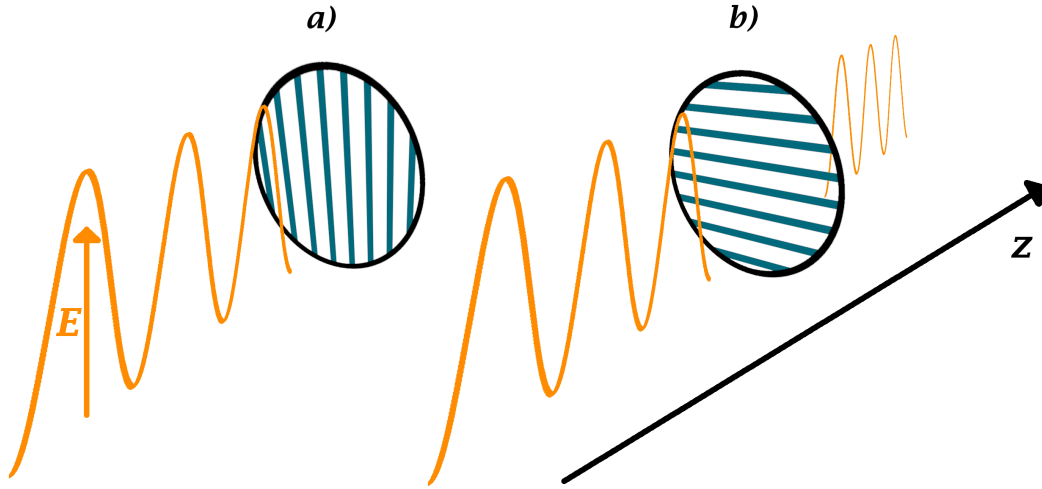

Figure 2.7: Wire grid polarizers are a simple type of polarization optics. Thin conducting wires allow an external driving field to move electrons only in one direction. The electric field generated by the moving electrons cancels the incoming wave behind the polarizer. This element hence only allows light with polarization perpendicular to the wires to pass. An electromagnetic wave is propagating in z-direction. Wire grid polarizers are shown in blocking (**a**) and passing (**b**) direction.

If the polarization direction is parallel to the the wires, the charges will be moved freely along the wire by the oscillating electric field and emit an electromagnetic wave themselves. This wave cancels the incoming wave behind the polarizer via destructive interference and counter-propagates on the other side. Effectively the incoming wave gets reflected.
On the contrary, in case of the wires being perpendicular to the polarization and thin compared to the wavelength, the charges can not be moved. Therefore the wave can propagate through the polarizer as it would be the case for any other dielectric material.
For any other combination of polarization direction and wire direction, the charge will only be moved by parts of the electric field. By projecting the E-field on the polarizer axis we find the passing component $\vec{E} \cdot \hat{e}_{wire} \hat{e}_{wire}$, while the remaining component perpendicular to $\hat{e}_{wire}$ gets rejected. This possibility to tune the amplitude of the passing wave by using a polarizer, makes them a very versatile building block for optical applications. This especially useful in combination with half-waveplates, an optical device made from birefringent

material, that can be used to turn the polarization direction of linear polarized electromagnetic waves with only miniscule losses in power.
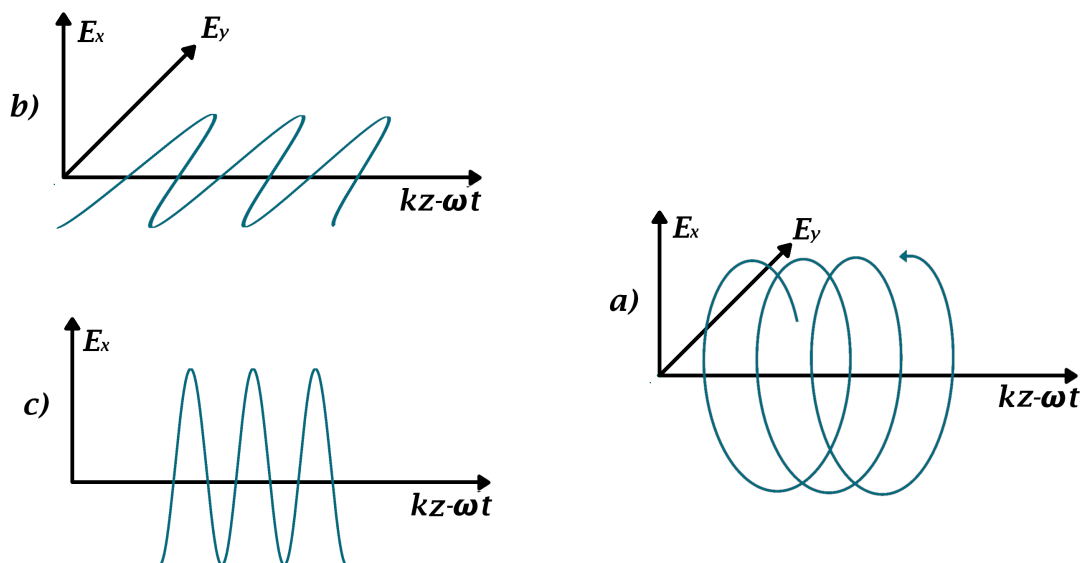
Figure 2.8: Light linearly polarized in x- (**c**) or y- (**b**) direction: The electric field vector only oscillates in the corresponding plane. A combination of two perpendicularly polarized waves with a phase difference of $\frac{\pi}{2}$ effectively leads to a spiral motion of the field vector: This phenomenon is called circular polarization (**a**).

The name "linear polarization" already hints at the existence of other forms of polarization. The most important (and only other one relevant in this thesis) is the circular polarization. Luckily, it is easily described by superimposing two linearly polarized plane waves with perpendicular polarization directions, but otherwise the same wavelength, propagation direction and amplitude, with a phase difference of $\pi/2$. For example a circular polarized wave propagating along z-direction could be written as

$$\vec{E} = \begin{pmatrix} E_{0,x}cos(\vec{k} \cdot \vec{r} - \omega t) \\ E_{0,y}cos(\vec{k} \cdot \vec{r} - \omega t + \frac{\pi}{2}) \\ 0 \end{pmatrix} \tag{2.24}$$

Such a wave essentially has the property of the E-field vector periodically moving in a circular motion around the propagation direction instead of oscillating in a plane (fig. 2.8). Quarter-wave plates can be used to convert linear to circular polarization and vice versa.

17

2.2.3 Ray Optics and Lenses

From a practical viewpoint, when building an optical experiment or device, it is important to know how a beam of light propagates in free space and behaves when encountering certain optical elements or interfaces. While it would be possible to use the approach of wave optics, this can quickly become laborious and generate a lot of practically less important side-results. It would be useful to have an approach that makes describing the path of light rays easy in standard situations, while accepting that certain special cases need to be treated separately. Such an approach is the so called ray optics model. It is rather accurate as long as all involved structures are large compared to the wavelength.

Ray optics is based on the notion that light consists of infinitely thin rays that propagate unhindered along the fastest path [35]. As long as they do not encounter an interface or travel through an inhomogeneous material, this means they are represented by straight lines.

When encountering a reflective surface, the rays get reflected such that the angle between the normal vector of the surface forms the same angle with the incident beam as with the reflective beam and all three lie in the same plane (fig. 2.10a).

When encountering an interface of two materials with different refractive indexes (meaning different speed of light in the materials), the ray changes its direction according to Snell's law (fig. 2.10b) [36]. This process is called refraction and described by:

$$\frac{sin(\alpha_A)}{sin(\alpha_B)} = \frac{n_B}{n_A}. \tag{2.25}$$

Here, $\alpha_{A/B}$ is the angle with the interface normal on side A/B of the interface, while $n_{A/B}$ is the refractive index of the material on either side.

A crucial optical building block based on refraction is the lens, a piece of transparent material curved to focus rays to a point or disperse them in a controlled fashion. When a ray of light passes through a lens, it encounters two interfaces that could be treated individually via eq. 2.25. For thin ideal convex lenses that are centered on a straight line, called optical axis, this is not necessary and they can be treated as just a plane that alters the direction of rays following certain rules (fig. 2.10c):

- All rays crossing the intersection of lens plane and optical axis propagate through the lens unaltered;

- All rays parallel to the optical axis will be refracted by the lens such that they cross the optical axis in the same point. This point is called focal point and the distance between lens plane and focal point along the optical axis is called focal length f. It is a characteristic property of a lens related to its shape and material;

- All rays crossing the focal point will be refracted by the lens such that they are parallel to the optical axis.

A similar concept is true for concave lenses, but here the extension across the lens plane of incoming or outgoing beams need to cross the focal point on the other side of the lens in order to be linked to a parallel beam (fig. 2.10d). Those lenses hence diverge light in a controlled manner, while the aforementioned convex lenses focus it.
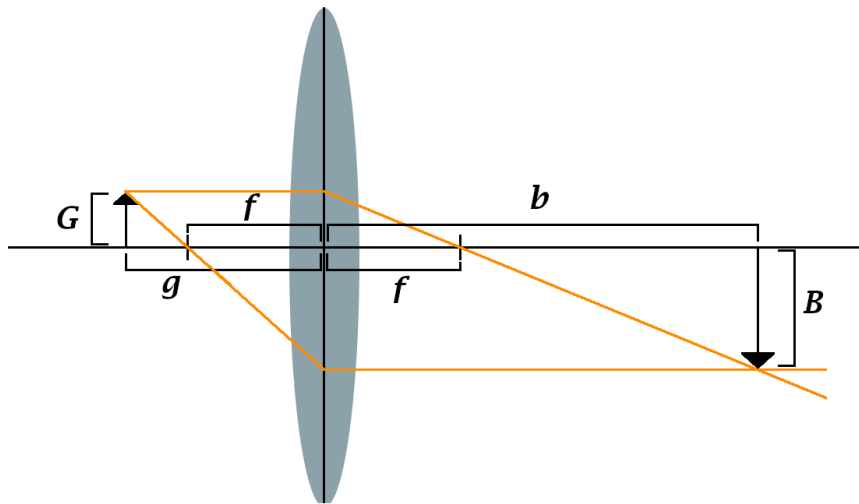
Figure 2.9: A lens generates an image of an object by refracting incoming light rays. The imaging equation (eq. 2.26) describes the position (b) and size (B) of the image as a function of focal length (f), object distance (g) and object size (G).

Being able to geometrically specify these three special beams is enough to analyze how to properly align lenses in many optical setups. The most basic, but nonetheless important one, is imaging an object with a lens: In such a setup an object is brought into proximity of the lens. Knowing the distance of the object to the lens on the optical axis (g), and the focal length of the lens f, the distance of the image to the lens b can be calculated by the imaging equation [37] (fig. 2.9):

$$\frac{1}{f} = \frac{1}{b} + \frac{1}{g}.$$
(2.26)

Knowing b and g, the apparent size B of the image on a screen can be calculated from the actual size G via

$$\frac{B}{G} = \frac{b}{g}.$$
(2.27)

By combining several lenses, more complex optical devices such as telescopes, microscopes etc. can be constructed.

19
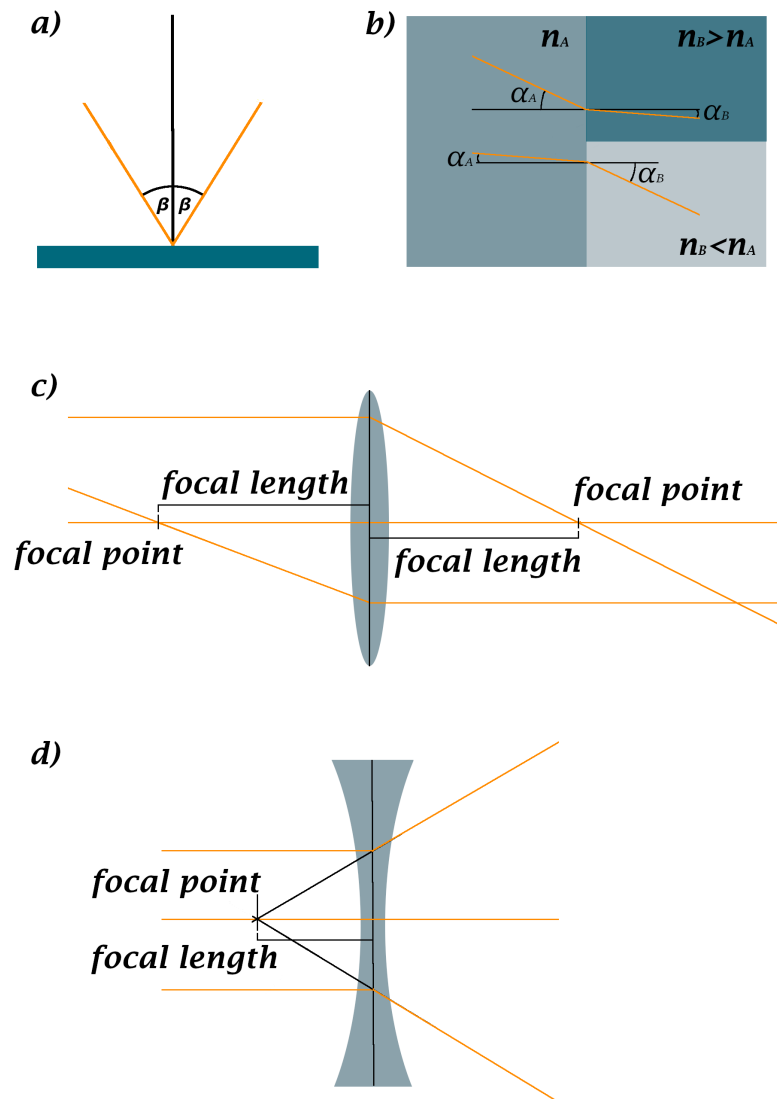
Figure 2.10: Ray optics allows for a simplified description of the behavior of light at interfaces. Reflection (**a**) on a surface is defined by the equality of the angle of incidence (β) being equal to the reflection angle. Refraction (**b**) of light when entering a medium is described by Snells law (eq. 2.25). The light refracts towards the surface normal when entering an optically denser medium and away from it otherwise. Lenses are a simple technical application of refraction. While convex lenses (**c**) focus parallel light beams on a focal point, concave lenses (**d**) diverge them.

2.2.4 Interference, Diffraction and Gratings

As already stated in section 2.2.3, while having the advantage of easily planning and writing down optical systems, ray optical descriptions come at the cost of disregarding certain effects based on the wave properties of light. Many of these effect are only relevant in special cases, are small or very local (e.g. absorption or non-linear optics) and, in this thesis, will therefore be discussed in-place if needed. There are two consequences of wave optics though that are universally relevant for understanding the spread of light. Usually those are taught as independent properties of light additional to the ray picture in order to keep the predictions consistent with experimental observations. These two are interference and diffraction.
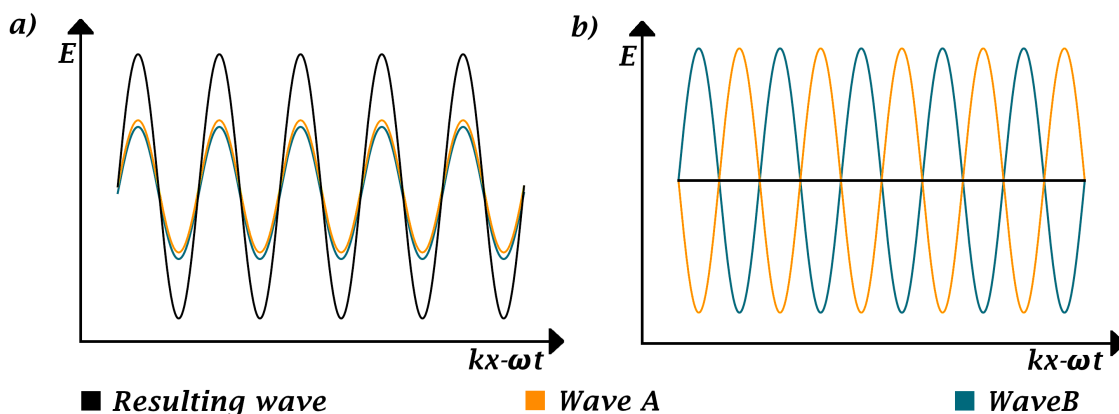
Figure 2.11: The linear addition of two oscillating electrical fields is called interference. When perfectly aligned in phase, constructive interference will lead to summation of the amplitudes of both waves leading to a stronger effective wave (**a**). When perfectly misaligned in phase, the amplitudes will get subtracted and two harmonic waves of equal amplitude will effectively cancel out entirely (**b**).

Interference is the direct consequence of the adding the time-dependent electrical fields of superposing light waves resulting e.g. in changes of amplitude or beatings. A very instructive example is again given by two plane waves with equal frequency and amplitude co-propagating. If these two waves have the same phase, their maxima and minima align and the resulting wave has twice the amplitude of the original waves. This is called *constructive interference*. If there is a phase difference of π though, the maxima of one wave align with the minima of the other: they *destructively interfere* leading to no effective electric field remaining (fig. 2.11).

Diffraction describes the bending of light close to an obstacle in contrast to the behav-

ior expected from ray optics. This effect is especially pronounced for structures being roughly the size of the wavelength or smaller. It is most easily understood by applying the Huygens' principle: The Huygens' principle is a very fundamental property of any kind of wave. It states that, in order to analyze the propagation of a given wave, every point of the wavefront can be viewed as the source of a so called elementary wave. These elementary waves are spherical waves of the same speed and wavelength as the original one, but do not penetrate into the room already occupied by the wave. The combination of all these waves then yields the new wavefront (fig. 2.12a).
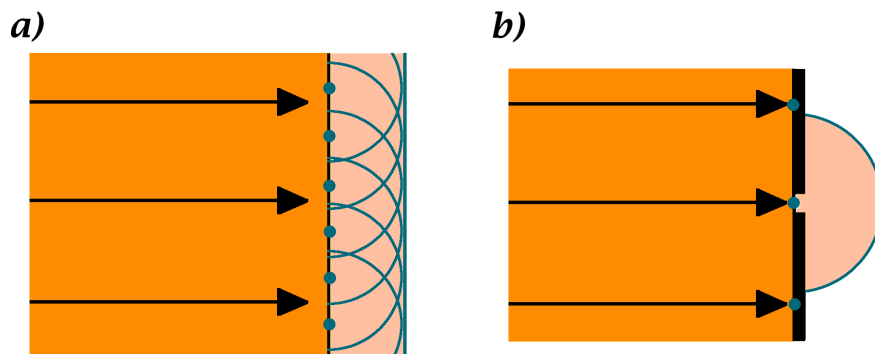
Figure 2.12: Huygens' principle states that any point of a wavefront can be viewed as the source of a new isotropic circular wave. While this has nearly no consequences for a freely traveling large light beam (**a**), its implications become clear when looking at a beam encountering a small slit: The beam divergence widens as a consequence of only few circular waves passing, explaining the phenomenon of diffraction (**b**).

Applying this principle to a plane wave passing a slit directly illustrates diffraction: If the slit is large compared to the wavelength, many elementary waves add up and it basically passes as expected from ray optics with only edge effects occurring. In case of a slit being small compared to the wavelength, only spatially very close elementary waves can pass and a new spherical wave will emerge from the slit (fig. 2.12b).

A famous experiment illustrating diffraction and interference of light at the same time has been performed in the early 19th century by Thomas Young: The double slit experiment [38]. Here, two parallel thin slits are illuminated from the back. The passing light is captured on a screen. Following ray optics or a particle picture of light one would consequently expect two narrow illuminated stripes to appear on the screen. But in fact a symmetric pattern of multiple stripes appears. This is due to the light being diffracted at both slits

leading to two elementary waves emerging. These waves interfere and hence yield the so called interference pattern on the screen.
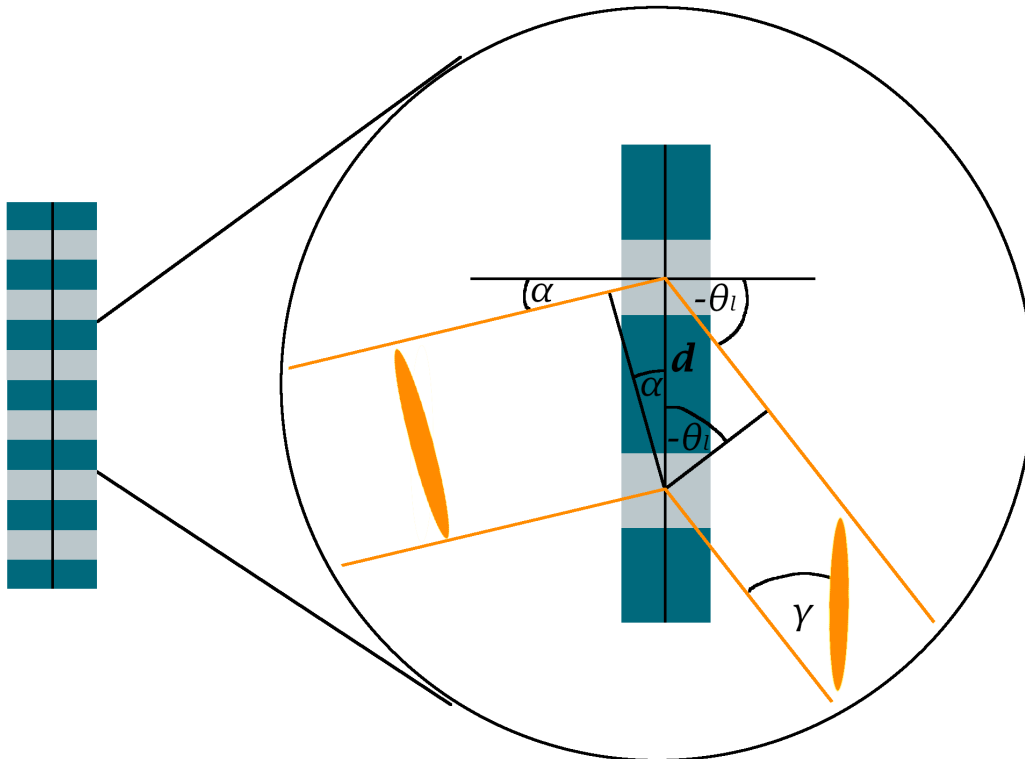
Figure 2.13: A grating diffracts incoming light into wavelength-dependent diffraction orders and tilts the wavefront by an angle γ. This is described by the grating equation 2.28.

A crucial optical component used in the experiments presented in this thesis works based on this principle. When expanding the idea of a double slit to a component consisting of many slits, arranged periodically, we arrive at a component called diffraction grating. A diffraction grating distributes light into several beams of different directions (fig. 2.13). This can easily be understood geometrically: A maximum appears in a direction where the additional path difference between all elementary waves is a multiple of the wavelength such that constructive interference takes place. This can mathematically be expressed by [39]:

$$d\left(sin(\theta_l) - sin(\alpha)\right) = l\lambda. \tag{2.28}$$

23

Here, d is the distance between the periodic elements of the grating, λ is the wavelength, l is and integer and the diffraction order, θ_l is the diffraction angle of order l and α is the angle of incidence. We can directly see that the diffraction angle depends on the wavelength and hence gratings are a dispersive elements. A grating can be designed in such a way (e.g. blazed gratings) that nearly all power is diffracted into a single desired order. The ration of the power in the desired order and the incident power is called grating efficiency.

In this thesis it will be important that a grating tilts the wavefront of an incoming beam. This again can easily be understood geometrically (fig. 2.13): Some parts of the wave need to travel longer than the others due to the aforementioned path difference, effectively tilting the wavefront. The tilt angle γ can then be calculated easily using the grating equation eq. 2.28:

$$tan(\gamma) = \frac{\Delta_{path}}{d} = \frac{l\lambda}{d}. \tag{2.29}$$

As we have seen in the previous sections, the wave character of light is responsible for many important phenomena and components and will hence be crucial in this thesis.

2.2.5 Particle and Quantum Picture

In the previous sections we have discussed many properties of light that can be explained by describing it as a wave (e.g. polarization, interference, diffraction). In the light of these observations, particle-based theories could not explain the experimental observations and knew approaches were necessary. That is, until in the beginning of the 20th century, Max Planck was able to theoretically describe the temperature-dependent spectra of blackbody radiation by quantizing the involved energies. Initially this was thought of as merely a mathematical trick [40]. But when Albert Einstein in 1905 explained the photoelectric effect using the quantized excitations of the electromagnetic field, later called photons, as description of light, it became clear quantum phenomena indeed bear a physical meaning and the highly fruitful field of quantum physics emerged [40].

Photons transport the energy of the electromagnetic field in finite local packages, which cannot split on their own, in a particle-like fashion. This is especially relevant when interacting with matter: In order to excite a state over some kind of gap, a single photon needs to carry enough energy, the state cannot (in first order) be excited by just absorbing multiple photons. Hence light seems to have particle-like properties. But as discussed before, light shows many properties of a wave-like behavior as well. In a modern quantum physical view this is not a contradiction anymore, quantum objects can behave like classical waves or particles in different scenarios. This phenomenon, not only true for light, but e.g. for particles as well, is called wave-particle duality. It can already be glimpsed at by looking at the formula giving the energy of a photon:

$$E_{ph} = hf. \tag{2.30}$$

With f being the frequency of the electromagnetic wave and h being the Planck constant, it interconnects particle and wave like pictures.

In this thesis both the photon- and electromagnetic wave-perspective will be relevant to explain the physics involved.

2.2.6 Laser Light

After having discussed some general theoretical properties of light and optical components in the previous sections, it is time to have a look at the type of light source that is necessary for the performed experiments as well as the characteristics of the emitted radiation. In order to be able to precisely control the experiments, light with very well-defined properties is required. It should be monochromatic (has, up to a small error, only one wavelength), of constant power, collimated (travel in a beam with minimal widening) and in general strongly coherent in time and space. Coherence describes, in some sense, the ability of a ray of light to interfere with itself. In our case it mainly means a high spatial and temporal stability of phase.

In practice it is very difficult to achieve light of such high quality. While metal-vapor lamps can deliver very monochromatic light due working based on atomic emission lines, the photon emission occurs randomly resulting in incoherent radiation. In fact easily generating coherent light was not possible until the invention of the laser in the mid of the 20th century [41]. Due to the unmatched quality of laser light, it is at the core of the experiments performed in this thesis - and most other modern optics experiments. It is therefore crucial to understand how lasers work and it will be discussed in this section.

Laser is actually an acronym for *Light amplification by stimulated emission of radiation*, which already explains the core of its working principle. The photons are not generated via spontaneous emission (as e.g. in metal-vapor or thermal lamps), but via stimulated emission. The simplest system to imagine in order to understand the involved processes is a two-level system that can interact with the electromagnetic field. (fig. 2.14a). If the system is in the excited state it can spontaneously relax under emission of a photon. This process is called spontaneous emission. If if is in the ground state and in presence of photons of suitable energy, it can switch to the excited state by annihilating such a photon. This process is called absorption. But there is a third kind of interaction: When in the excited state and in presence of absorbable photons, the system can be triggered to relax to the ground state under emission of a photon by interaction with one of the already present photons. The freshly emitted photons then inherits the properties (especially the direction, polarization and phase) of the stimulating photon. This process is called stimulated emission and leads to the high quality of laser light.

All three processes combined will drive the system in a thermal equilibrium. In order to build a laser, we need to gain more photons via stimulated emission than we loose via absorption or spontaneous emission. The rates for these three processes depend on each
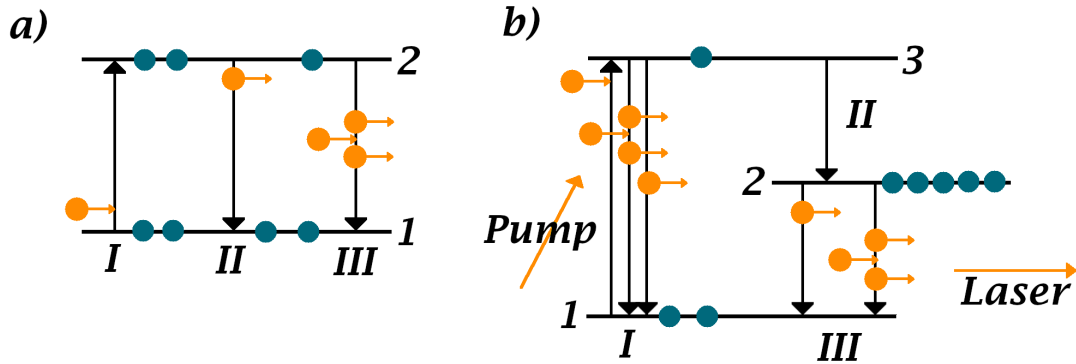
Figure 2.14: **a**) Two energy levels and their possible bright transition mechanisms: Absorption, spontaneous emission, stimulated emission. A population inversion is not possible. **b**) Schematics of a three-level laser. A transition state (3) is pumped (II) from the ground state (1) and quickly relaxes (II) to another long-living intermediate state (2). By doing so a population inversion can be achieved between state 1 and 2 and the transition via stimulated emission can be used for lasing.

other and are given by the Einstein coefficients. For non degenerate ground (1) - and excited (2) state their relation is given by [42]:

$$B_{1\to2} = B_{2\to1}, \tag{2.31}$$

$$\frac{B_{2\to1}}{A_{2\to1}} = \frac{\lambda^3}{8\pi h}. \tag{2.32}$$

Here, $B_{1\to2}$ is the coefficient of absorption, $B_{2\to1}$ for stimulated and $A_{2\to1}$ for spontaneous emission. The transition rate (in processes per time) is proportional to the respective Einstein coefficient as well as to the occupation number of the initial state.

As a first interpretation of eq.2.31 we see that the coefficients of absorption and stimulated emission are equal. This mean that, even neglecting the losses via spontaneous emission, if we want to gain more photons via stimulated emission than we loose via absorption, the exited state needs to be occupied higher than the ground state. This situation of the exited states being more populated than the ground state is called population inversion. Achieving it is at the heart of lasing.

The second realization from eq.2.31 is, that it is not possible to achieve population inversion by simple optical pumping. Latest when ground and exited state are equally populated, the transition rates become equal as well and an equilibrium is reached. This problem has been solved by using multi-level system. To understand the concept a three-level system

26

is sufficient, even though in practice more levels can be involved. There are three relevant transitions (fig 2.14) [43]. The first transition (I) moves electrons from the ground state (1) to a first excited state (3). This process is typically called pumping. It can happen by optical pumping via flash lamps or other lasers, but also e.g. electrical depending on the system. As before a maximum of equally populated states can be achieved here. Another transition (II) relaxes the electrons to a second, energetically lower excited state (2). This transition needs to be fast compared to the spontaneous-emission of the third transition (III) that relaxes the second exited state (2) back to the ground state (1). This last transition is the actual lasing transition that is supposed to mainly occur via stimulated emission. Since the second transition II is much faster than the spontaneous emission of the lasing transition III, electrons will pile up in the second excited state (2) and the desired population inversion is achieved!

While not critical to this thesis, it is noteworthy that from eq. 2.32 it follows that the ratio of spontaneous and stimulated emission gets much worse for shorter wavelength making it much harder to build lasers in the high energy regime and decreasing their beam quality respectively.

After having understood the physical principles of achieving population inversion it is instructive to have a closer look at the technical realization of a laser (fig. 2.15). At its core it consists of three components [43]: Firstly, the gain medium. This is the heart of laser, the material in which the population inversion needs to be achieved and that generates the laser light via stimulated emission. It is typically enclosed in the second component: a resonator that can e.g. be formed by two mirror. One of these mirrors is transparent to a small degree. Thirdly there is some kind of pump that generates the population inversion in the gain medium.

Practically, depending on the capabilities of pump and gain medium, the pumping can be performed in a pulsed fashion (e.g. with a flash lamp) leading to a pulsed laser operation or continuously (e.g. via a pump laser or electric discharge) leading to a continuous wave (cw) laser operation. Either way the basic operation principle is the same: The pumped gain medium generates few photons via spontaneous emission. These photons stimulate the emission of further photons. They travel back and forth through the resonator and with every roundtrip the lasing increases exponentially until an equilibrium is reached. Due to this exponential self-amplification the most suitable lasing modes are automatically selected, e.g. only the photons traveling perfectly aligned to the resonator will be selected leading to high collimation.

Today many lasers are constructed as fiber lasers (fig. 2.16). Here the gain medium is the doped core of an optical fiber. This makes it possible to couple a pump laser directly into the fiber and hence very efficiently pump the spatially long gain medium leading to very high conversion efficiencies [45]. Fiber lasers also allow to be highly selective for the spatial

27
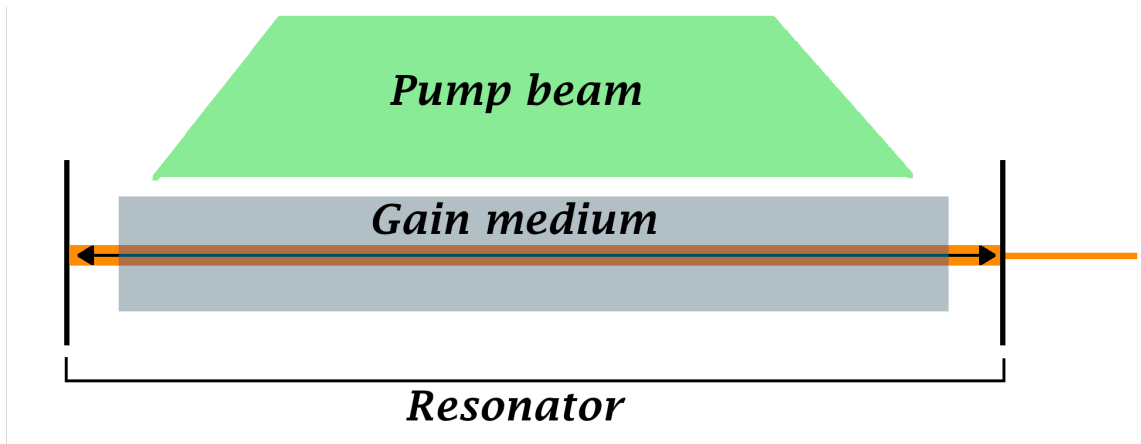
Figure 2.15: Setup of a laser: A pumped gain medium is enclosed in resonator mirror allowing light to travel long distances through the gain medium and hence experience strong amplification. A partially transmissive mirror releases the laser light from the resonator.

mode leading to very high beam quality: Usually one wants the lasing to occur mainly in the fundamental transverse electromagnetic mode (TEM_{00}), meaning that electric and magnetic field components are purely orthogonal to the propagation direction and the intensity profile of this mode is a Gaussian. A measure of how much a beam deviates from the TEM_{00} mode is the beam quality factor M^2 [46]. While ideal beams in ray optics can be perfectly collimated or cross in an infinitely small focal spot, realistic beams, better described by Gaussian optics, cannot. When trying to focus them, they converge to a finite width before diverging again. This point of smallest radius is called beam waist. If the profile of a beam is at least close to a Gaussian and rotational symmetric, the quality factor can easily be calculated by observing the divergence ϕ of a beam at its waist, ω_0 [46]:

$$M^2 = \frac{\pi \omega_0 \phi}{\lambda}. \tag{2.33}$$

From a practical viewpoint it is noteworthy that the minimal achievable focal spot size is proportional to the beam quality factor M^2 in this picture. Hence, having a beam as close as possible to a Gaussian beam is very desirable in many cases as it can be focused more tightly (and collimated better) the closer it is to the this fundamental mode. With a fiber laser values close to $M^2 = 1$ are routinely achieved, making them a great choice for many experiments.
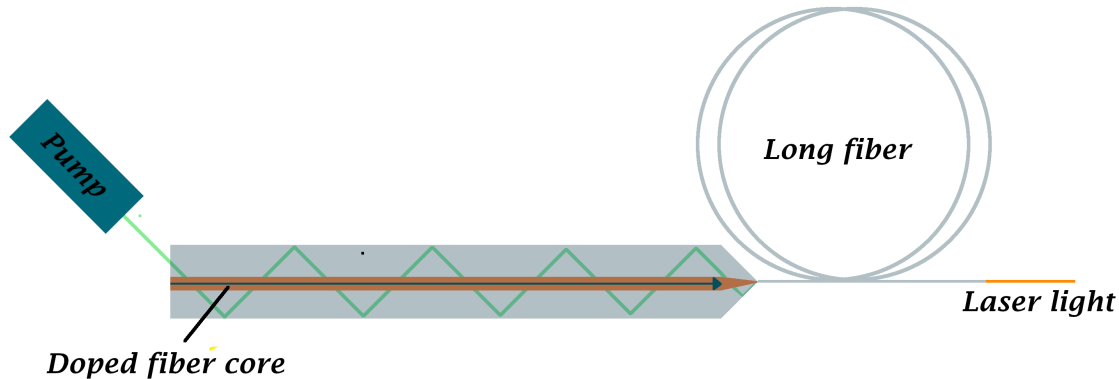
Figure 2.16: The gain medium of a fiber laser is the doped core of an optical fiber. The possibility to build very long fibers allows for efficient lasers with exceptional beam quality. Furthermore efficient pumping is possible by coupling pump light into the same fiber.Plot inspired by [44].

2.2.7 Ultrashort Pulses

In the beginning of this chapter we expressed the desire to use light as a tool to access ultrashort timescales beyond the reach of the typical electronic bandwidths. Up until here, even though a lot of fundamentals were explained, we did not come noticeably closer to this goal. While light is very fast in propagation and (potentially) in its field oscillations what we actually need is a short event in time. This already excludes using lasers operating in continuous wave(cw)-mode. Of the concepts already discussed, the pulsed operation of a laser, as mentioned in section 2.2.6, seems most suitable.

By now we have discussed that this possible by pumping in a pulsed fashion. When exciting the gain medium with a pulse (e.g. flash lamp), the lasing will only start after reaching some threshold in population inversion. After starting the lasing the exponentially growing photon count will quickly use up the available inversion, after which the lasing comes to an end if no further pumping occurred. By carefully choosing a suitable pumping pulse energy and duration, single pulses can be generated. While these pulses are short on everyday timescales, they will not generate the desired ultrafast sub-picosecond events. For example, ruby lasers operated via pulsed pumping barely reach the sub-millisecond regime ([47]).

A more sophisticated approach to control this pulsed relaxation of population inversion has already been demonstrated by Robert Hellwarth in 1962 citeqhell, rpQ: Q-switching. Q-switching [48, 49] is based on a variable quality factor (Q-factor) of the resonator. Initially the resonator's Q-factor is kept low such that no lasing will occur and the gain medium can be pumped until saturation, which would not be possible during lasing. At some point the resonator switches to the high Q-factor mode. Due to the highly excited gain medium, the

photon numbers will raise extremely fast and high, hence, leading to a pulse with higher intensity and shorter duration than it would have been possible otherwise. For example, quality switched ruby lasers can routinely achieve pulse durations in the nanosecond regime [50]. Technically a Q-switch can e.g. be realized via the Pockels effect or saturable absorbers [48, 49].

While quality switching is a potent way of generating short high energy pulses, it still does not open up the desired sub-picosecond timescale [48]. In order to advance into this regime we need to further look at the relevant processes on these timescales: A single field oscillation of visible light takes roughly 2fs. Therefore the desired sub-picosecond regime is governed by only relatively few field oscillations. It is hence crucial to further understand which modes are actually excited in a given laser and how they oscillate.

The first limiting factor for modes of which frequency will be exited is the bandwidth of the transition driving the stimulated emission. These might be very sharp resonances, e.g. in gas lasers, but the emission lines can very well be strongly broadened by their surroundings, e.g. in condensed matter lasers.
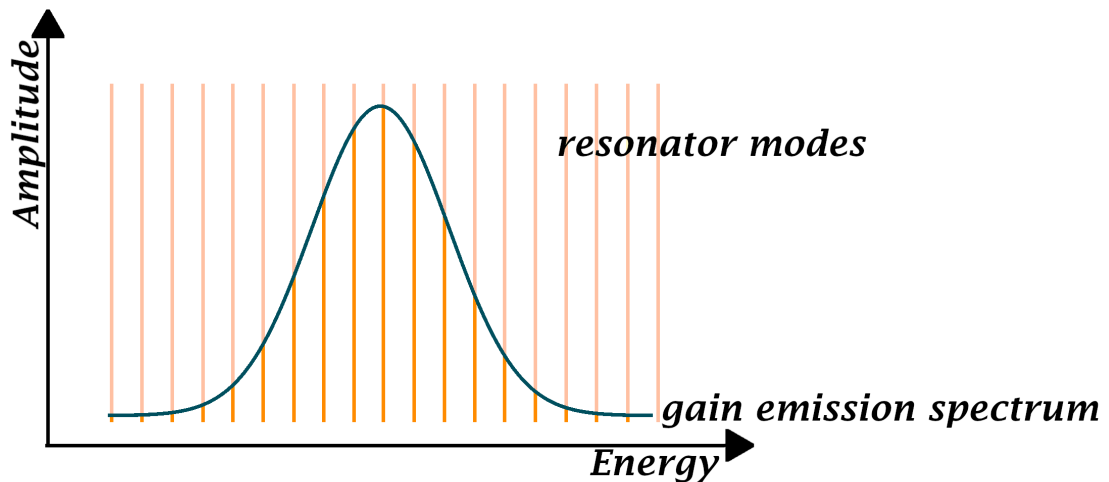
Figure 2.17: The possible lasing modes are given by two conditions: A multiple of the wavelength needs to fit into the resonator, leading to many densely spaced resonator modes. Secondly, the mode needs to lie within the emission spectrum of the gain medium. If no further selection occurs, a laser can lase in many different modes at the same time. Adopted from [51]

But not the whole continuum of supported wavelengths will actually be present in a laser. This is due to the optical resonator. It will only support modes that can form a standing

wave inside, while other oscillations cancel due to destructive interference. A standing wave in a linear cavity can be formed if the length of the resonator is a multiple of the half wavelength. The combined modes that correspond to a wavelength inside the aforementioned emission spectrum of the gain medium make up the laser radiation (fig. 2.17) [52]. With macroscopic resonators, this means that for typical condensed matter lasers many modes are simultaneously oscillating. Since they have no intrinsic reason to have a fixed phase relation, the resulting radiation will have a noisy average value in time. Fixing a phase relation between these modes is the core idea of mode-locking [51, 53–55]. This is closely related to the concept of Fourier transform, where an arbitrary function is projected onto the space of sine-functions.:

$$U(f) = \frac{1}{2\pi} \int_{-\infty}^{\infty} u(t)e^{i2\pi ft}dt. \tag{2.34}$$

Like this it is possible to decompose most functions into a set of harmonic oscillations making the Fourier transform a connection between time- and frequency space. Consequently by forming a suitable phase relation of enough excited laser modes in a laser of sufficient bandwidth, short effective laser pulses can be generated.

Practically there are different, active and passive, ways of mode-locking a laser [51]. For simplicity, we will restrict ourselves to shortly discussing a single one here: Mode-locking via Kerr-lensing [51, 56, 57]. This approach is based on the Kerr effect. This nonlinear optical effect describes the dependence of the refractive index on the local electric field strength: The laser radiation traveling in the gain medium will get focused depending on its own field strength. Since shorter pulses focus their energy more tightly in time, they are focused more strongly than longer pulses or cw-radiation. By introducing an aperture clipping the outer parts of the resonator, the shortest pulses get favored and hence the system will lase in this mode. Practically, there is obviously more to consider, first of all a proper dispersion compensation is necessary in order to keep the pulse compressed, but the basic principle applies and has been used in many femtosecond laser systems. For example, the naturally broadband Ti:Sapphire laser readily emits pulses with well below $100fs$ pulse duration, using kerr lensing mode-locking techniques [56].

With this section, we finally arrived at an object, ultrafast mode-locked laser pulses, that is exceptionally short in time and can hence potentially be used to access these fundamental timescales of matter.

2.2.8 Pump-Probe Schemes

Up until this section we have established how ultrafast pulses can be generated. In a final step we now need to discuss how we can use them to gain insight into the ultrafast processes in other systems. While experimentally challenging, the basic concept is surprisingly easy: Pump-Probe experiments.

The basic idea of these types of experiments is to send two optical pulses with a defined

time delay. The first pulse (pump) somehow alters the system. The second pulse (probe) acts as readout signal. By altering the pump-probe delay, the time evolution of the effects caused by interaction with the probe pulse can be mapped out with high temporal precision effectively only limited by the pulse duration and technical precision.

For example a material could be electronically excited via absorption of the pump pulse. As long as it is exited, it will absorb the following probe pulse to a lower degree, as less unoccupied excited states are available. After relaxation, the absorptivity returns to baseline. By measuring the power or spectrum of the probe pulse dependent on the delay, the lifetime of the excited state can be mapped out.
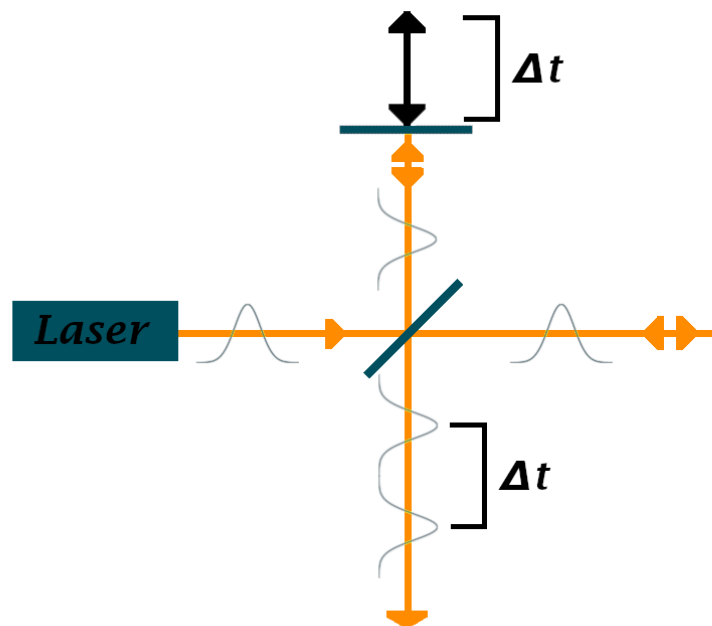
Figure 2.18: Pump probe schemes are a possibility to access ultrafast timescales. A first light pulse modifies the system, a second one acts as a readout. The necessary two laser pulses with an ultrashort temporal delay can be generated by splitting one pulses into two and letting them travel different distances prior to recombination. One way to do so is the interferometric approach, using a central beamsplitter, shown above.

Technically pump-probe experiments are often realized by splitting a single pulse into two pulses using a beamsplitter. One of these pulses can then be variably delayed by sending it over a spatially precisely controllable delay line. Afterwards the pulses can be recombined and fed to the system and detector subsequently (fig. 2.18). Due to the typically high

repetition rates of ultrafast pulsed laser, many pump-probe pulse pairs will arrive during the response time of the detector,automatically yielding a high averaging and stronger detector response and making slow quasi-DC measurement tools feasible.

We have now finally arrived at the desired goal of understanding how to use optics to gain insight into ultrafast processes. In combination with the STM/STS theory already discussed, the basic theoretical framework, necessary to understand the experiments performed in this thesis, has been set.

CHAPTER 3

EXPERIMENTAL DETAILS

Within the framework of this thesis, the goal is to combine high spatial and ultrafast temporal resolution by means of building a THz-STM and performing first proof-of-work experiments. In this chapter, as a first step we discuss the basic working principle of a THz-STM in order to understand the experiment we aim at. In a second step, we describe the used infrastructure, pre-existing or newly installed, for this project.

3.1 Making STM Ultrafast: Working Principle of a THz-STM

The high spatial resolution of STM makes it an obvious choice when investigating electronic processes on surfaces localised on atomic length scales. There is one major flaw in though: These processes are typically ultrafast. While the tunneling junction itself is capable of responding on timescales down to a few femtoseconds [10], the measurement electronics severely limit the possible time resolution. Especially the bandwith of the current amplifier, does not allow to resolve dynamics much faster than the microsecond time scale [10]. Standard STM can hence often only record the time average of the observed physics.

It has hence not been long after the establishment of the STM in the community, that first approaches bypassing this limitation by fusing STM and the pump-probe-schemes known from laser physics have been presented: Using photoconductive switches in combination with optical pulses, ultrafast transient bias voltages were generated [9–11]. Though, beside requiring a sophisticated sample design and allowing only partial control of the applied transient bias, only limited success in maintaining high spatial resolution has been presented [10, 58]. Furthermore the observed time dynamic is heavily convoluted with the

response of the photo-switch itself [10]

Based on this general idea, many more approaches to realize time-resolved STM have been presented in the following years. Most notably, direct illumination of the STM junction with optical pulses in the desire of achieving time-resolution via photoexcitation of charge carriers has been attempted [10, 12]. Even though the theoretical concept seemed promising, the time-dependent thermal load brought into the system by the laser and leading to periodic tip contractions severely limited the use of this approach [10, 13, 14, 59, 60]. Shaken-pulse-pair-excited STM (SPPX-STM) in combination with high-repetition-rate lasers has proven itself to at least reduce some of the temperature problems by keeping the time average of the thermal load constant [10, 13, 61] and allowed for true time-resolved STM measurements [62]. While being very impressive, this technique is in first order limited to dynamics directly excitable via photons [11] such as molecular systems or semiconductors. Hence many typical STM systems cannot be investigated without engineering specifically tailored measurement schemes. Furthermore, albeit the thermal effects on the STM stability are highly reduced in this technique, the average thermal load itself is still the same, posing a severe challenge for low-temperature measurements required for many physical systems.
Only very recently, techniques fundamentally evading the high thermal load and being versatile in the choice of measurement system have been presented: These approaches are based on parts of the electromagnetic spectrum with low-energy photons that only weakly interacts with the materials in the STM head directly, keeping the thermal load low. Using pulses in the comparatively easy to handle GHz spectrum, this approach has been successfully used to gain insights into single atomic spins [11, 63]. Since microwave-photons can be directly absorbed during the (photon-assisted) tunneling process [64, 65], they can be used to form effective bias voltage pulses and perform pump-probe schemes [63].
Unfortunately, the period duration of GHz radiation is too long, preventing it from being used to form ultrafast pulses in the few- to sub-picosecond regime. But there is a part of the electromagnetic spectrum, which only recently became routinely available, that unites the field-driven interaction of GHz radiation with relatively short achievable pulses: Terahertz (THz) radiation.
THz-radiation is the part of the electromagnetic spectrum (fig. 2.6) between the far-infrared light and the microwaves, the range typically named is 0.1 THz to 10 THz [66]. Accessing this regime has proven itself somewhat difficult both in generation of coherent radiation as well as in detection. Only in the last decades, THz sources generating short pulses with comparably high energy as well as means of detection and characterization became available [67, 68]. The exploitation of THz-radiation made a variety of physical condensed matter effects energetically accessible to pump-probe experiments. For example, superconducting gaps, excitations in semiconductors, many phononic modes or spin excitations fall in the THz energy range [66]. However, while increasingly accessible, the setup and operation of THz experiments is still considerably more delicate than for a typ-

ical boxed laser system as e.g. available for the visible regime of the spectrum.
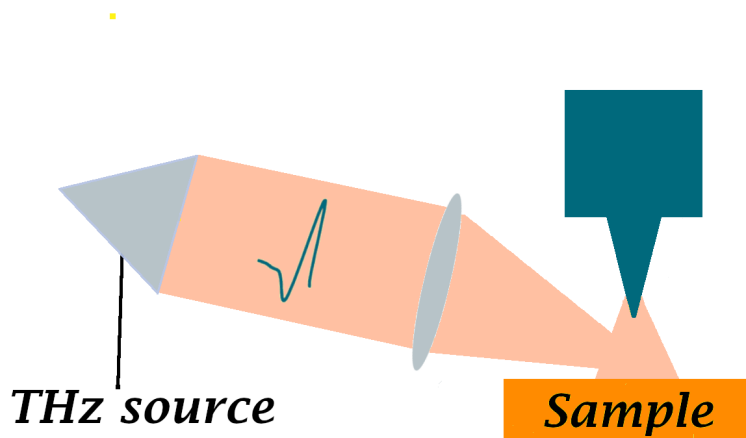
Figure 3.1: In a THZ STM, THz pulses are focused into the junction to act as an ultrafast bias.

The THz-STM is a novel scientific device combining the outstanding spatial resolution of STM (sec. 2.1.2) with the time resolution achievable via optical pump-probe experiments (sec. 2.2.8) by using such THz-radiation. It has been first presented by Tyler Cocker et al. [1] only recently in 2013. Since then, it has several times proven itself to push the boundary of experimentally accessible phenomena [66, 69–71], routinely combining high temporal and spatial resolution in a versatile approach.

A THz-STM is based on a usual STM system extended by an optical access. An external laser-source generates two THz-pulses with an adjustable delay. They subsequently get focused onto the STM junction (fig. 3.1). Here the tip effectively acts as an antenna and, when picking up a pulse, it gets focused into the junction via local field enhancement [66, 72], locally amplifying the pulses field strength by a factor of several thousands [1] inside the junction. Due to the comparatively low photon energy of THz radiation, it only weakly interacts with the sample on a single photon level, but in a field-driven regime [13]. Its electric field can be seen as a transient modification of the tunneling barrier in form of an ultrafast transient voltage pulse [1, 66]. Beside this being a versatile way of introducing time-resolution within the common way of thinking in STM and allowing access to all kinds of different system without special sample requirements, this field-driven interac-

tion solves a fundamental problem in time-resolved STM: The classically low-absorption of electromagnetic fields in metals keeps the thermal load on the STM extraordinarily low, in principle allowing high stability even under cryo conditions [1, 69]. On the other hand, THz radiation is still of high enough frequency to support pulses with sub-picosecond duration and hence facilitate the desired ultrafast time resolution.

Depending on the applied techniques, electric fields corresponding to maximal in-junction voltages from fractions of to many volts [72, 73] can be controllably generated, effectively introducing an ultrafast transient bias of the magnitude of typical STM DC biases. One now chooses a dc bias voltage, such that a certain state is initially energetically not available for tunneling, but is made accessible by the additional bias voltage introduced via the THz-pulse (fig. 3.2). Enabling this additional tunneling is called *opening a tunneling channel* and the additional current is the desired measurement signal. Consequently all electronic interaction with the state is limited to the ultrafast timescales during which the THz pulse is present in the junction. This direct interpretation with relies on the idea that the electric field of the THz pulse is weak enough to act as transient bias, but not heavily modifies the local electronic structure itself, which would make it harder to interpret the resulting current. This weak-field picture [13] is probably true for reasonable transient voltages, as it has been shown to be in excellent agreement with the usual Simmons model of tunneling [73–75]. For very strong applied THz fields deviations were shown to appear [74] . So for high voltages or local elements inside the junction (such as adsorbates), care has to be taken to verify that this straightforward interpretation is still valid. This is a non-unique problem to THz-STM though: tunneling, especially with small junctions or large voltages, can very well alter the system in standard STM [76]. Nevertheless, additional care needs to be taken: While large currents are obvious in normal STM and can be exactly adjusted using the feedback loop, they are only present on ultrashort timescales in THz-STM - but those can be extremely large [73]. Since the time-integrated current would still be very small, this might lead the user to underestimate existing strong-field interactions.

Now, if the electrons tunneling due to the first pulse excite the system in a way such that the tunneling probability into the state changes, the additional current due to the second pulse will change for all delays below the lifetime of the excitation. By recording this additional tunneling current, generated by transiently opening a tunneling channel via the probe pulse, as a function of pump-probe delay, information on the ultrafast dynamics of the examined system can be inferred. While this systems readout obviously relies on the THz-probe pulse, the pump pulse can in principle be of any other wavelength that can excite the examined system in a suitable way - as long as their power can be kept low and continuous enough to guarantee thermal stability. In this thesis, we will e.g. use optical pulses in the near-infrared region as pump. Since the tunneling, as it is always the case in STM, is extremely local, such a THz-STM successfully combines cutting edge spatial and temporal resolution and can potentially pave the way to a better understanding of
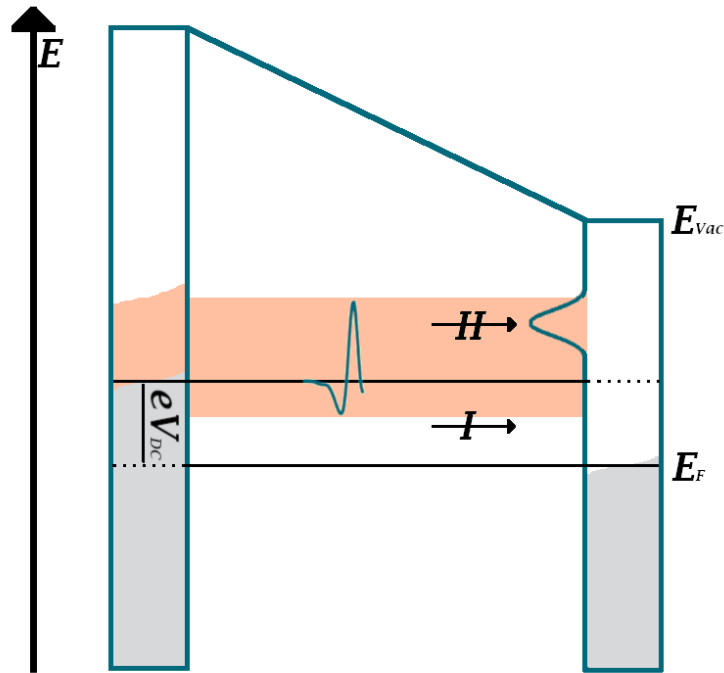
Figure 3.2: In a THz-STM, the THz-pulses act as an ultrafast transient bias voltage. To record time-resolved data of a feature, the DC bias is chosen such that it does not allow to tunnel through the state under observation (I). The additional voltage of the THz pulse then exclusively opens this tunneling channel on ultrafast timescales (II).

microscopic surface processes.

While the concept itself is rather straight-forward, there are many fundamental technical challenges in realizing such an experiment. In the following we want to name just a few: The first one is the generation of the ultrashort THz pulses themselves. As mentioned, the THz-regime of the spectrum is not as easily accessible as other spectral regions and hence a lot of work needs to be invested to generate and characterize suitable THz pulses. Secondly, water vapor features various absorption bands at THz energies [68, 77] and hence is a strong scatterer for this kind of radiation. Even though this, fortunately, is less pronounced for our low THz frequencies [78], the experiments still need to be as compact as possible and to be performed under conditions with the humidity of the air being as low as possible.

Lastly, the performance of STM experiments at the atomic scale typically requires ultra-high vacuum (UHV) conditions in order to keep the surfaces under examination atomically clean. Furthermore, cryogenic conditions are desirable to reduce thermal broadening and excitations as well as to enable the stability of single molecular or atomic systems. Both pose a considerably challenge as suitable window material needs to be selected at the different boundaries. This is especially problematic as the thermal load on the STM needs to be minimized in order to reach the desired cryo-temperatures. Unfortunately, according to Wien's displacement law, the thermal radiation of the involved temperatures happens to peak in the (higher) THz regime as well, rendering the desired properties of thermal filters more strict.

Throughout this thesis, we will present our approaches to overcome these, and further, hurdles and challenges in order to construct our version of a THz-STM.

3.2 Experimental Setup

The THz-STM experiments take place in a preexisting STM lab, at Freie Universität Berlin, that underwent heavy modifications in order to be suitable for its new use. As a first step, this included making the room ready for a laser experiment: It was heavily cleaned, potential dust sources were removed. To ensure laser safety, windows were blinded and a laser-safety-curtain was installed. It separates a safe entrance and measurement area, harboring a desk as well as the designated lab computer, from the potentially dangerous experimental area. Protective goggles for the involved wavelengths were placed in this gate area.

The tunneling microscope used is a preexisting commercial Createc beetle-type AFM/STM [79]. Since the AFM will not be used in this thesis, we will refrain from further discussing it here. In this type of STM, the tip, within this thesis we use etched tungsten tips, is connected to a central piezoelectric tube. It facilitates the fine movements in z-direction during measurements. It is connected to a central plate with a ramp that is sitting on three additional piezos. This ramp can be moved in x and y direction and rotated. Due to the slope of the ramp, the rotation leads to a coarse movement in z-direction, used to initially approach the tip.

The whole STM head (see fig. 3.3a) is suspended via springs connected to the bottom of a Helium cryostat, its movements are further damped by an eddy current brake. The cryostat is extended via radiation shields, covering the STM head. The whole Helium cryostat is surrounded by a liquid Helium cryostat, again featuring radiation shields (see fig. 3.3b). A shutter allows to transfer samples in and out. The system originally reached a base temperature of the microscope of about 4.8K.

Electronically, the STM is controlled using a Nanonis system [80] and a Femto current amplifier [81]. A Zurich Instruments [82] lock-in amplifier is used for detection of small

signals. All relevant cables are equipped with low-pass filters.
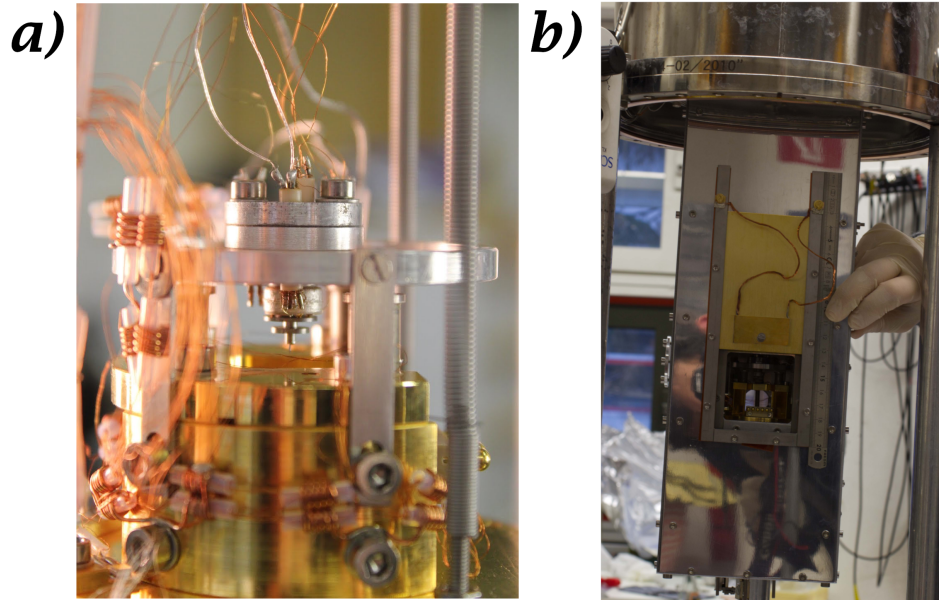
Figure 3.3: **a)** The STM head suspended on springs. Centrally the tiny STM tip can be seen that can be moved using the piezos it is connected to. The complex geometry with many potentially obstructing structures can be readily seen. **b)** The STM head is covered by two radiation shields to maintain cryo conditions. The large opening with a shutter is used for transferring samples in and out. Photography by C. Lotze.

In order to keep samples atomically clean, the STM is located inside a UHV-chamber (3.4a). This chamber is split into three main parts separated by valves:
Firstly, the STM chamber harboring the cryostat with the microscope.
Secondly, a preparation chamber used to prepare the different samples for measurement in the STM. It features an ion sputter gun, a mass spectrometer, several leak valves and a garage for samples. The transfer between preparation and STM chamber is done via a rotatable manipulator, which can be moved freely in xyz-direction. It can be cooled by pumping liquid nitrogen or helium through it. The sample plates used in this system feature a button heater as well as a thermocouple directly on the sample holder, which can be used in combination to precisely adjust the temperature of the sample during preparation or transfer.
Thirdly, a load-lock allows to introduce new samples or tips from the outside into the vacuum without contaminating the main chambers. Windows are placed over all chambers

allowing optical access in the visual range.

The UHV is maintained by a turbomolecular pump, two ion pumps, a titanium sublimation pump (TSP) and a cold trap. The whole chamber is supported by four pneumatic feet to further decouple the system from vibrations in the building.

Beside the STM and its UHV chamber, THz radiation is the second building block of a THz-STM. Of course, before being able to think about how to couple the ultrashort pulses into the STM, they need to be generated. As a basis, this requires a suitable lab infrastructure for optical experiments, which we set up:

We introduced a commercial $2,4m$ x $1,5m$ optical table into the lab [83], again suspended on pneumatic feet, to ensure mechanical stability for the delicate optical setup we wish to construct (see fig. 3.4b). The whole optical table got surrounded by a lamella curtain, decoupling the table from external airflow and dust. The interior is ventilated via laminar flow particle filters, ensuring clean and turbulence free air. This air is fed via a climate cabinet, stabilizing the temperature of the optical setup to $23 \pm 1K$. Furthermore dehumidifiers keep the air humidity on average below 30% to reduce THz scattering due to water vapor.

The basis for the optical setup is formed by a commercial $1030nm$, $50W$ fiber laser system, *Amplitude Satsuma* [84]. It features sub-$300fs$ pulses with high pulse-to-pulse and pointing stability, both being essential for the planned precision experiments. Additionally, a commercial optical parametric amplifier *APE AVUS* [85], was installed. It has not yet been used and will hence not be further mentioned throughout this thesis.

Optomechanical and optical components used on the laser table (see fig. 3.4c) are mostly commercial pieces produced by Thorlabs [86], Newport Spectra-Physics [87], EKSMA Optics [88] or Edmund-Optics [89]. Few special pieces have been bought at specialized retailers or manually produced in a mechanical workshop. Most optical parts feature special high power and anti-reflective coatings. In combination with being produced from low defect material, such as UV-fused silica, they reach the necessary high damage thresholds.

Data evaluation and was mainly performed using Python, LabView, SpectraFox [90] and WSxM [91].

After having configured the laboratory and instruments in the described manner, the fundamental infrastructure necessary to construct the THz-STM has been set.
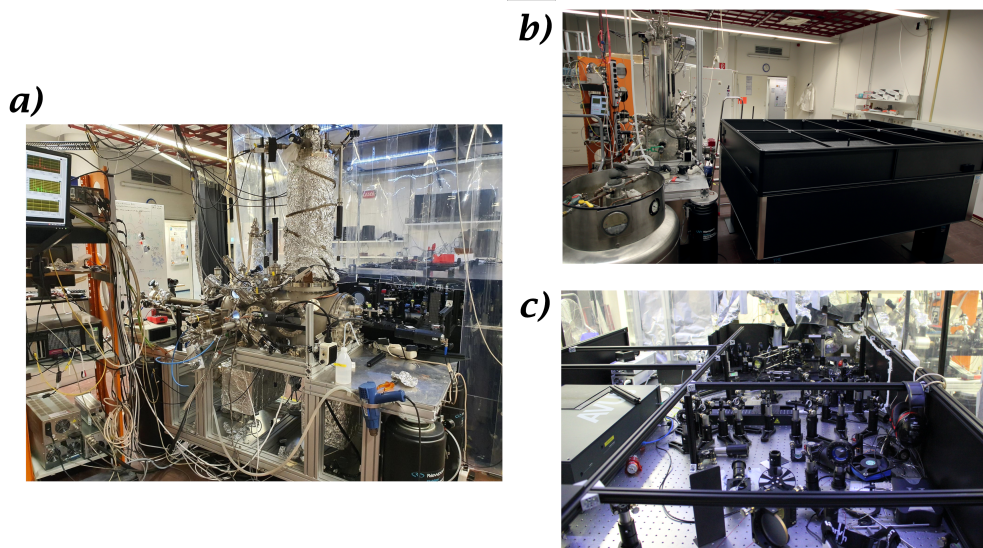
Figure 3.4: **a)** Our preexisting STM in its vacuum chamber. The large upright structure covered in aluminum foil is the cryostat. **b)** The laser table (right) is located directly next to the STM to allow coupling THz radiation from the former to the latter. **c)** Exemplary view of the optical experiment under construction showing various optical and optomechanical components. The vacuum window used for feeding THz radiation into the STM can be seen in the background. Photography by C. Lotze.

SAMPLE MATERIALS

The construction of the THz-STM itself is at the core of this thesis and sample system are, in contrast to the usual case of interest in its physics, mainly a tool for different testing scenarios. Yet, they still have substantial impact on the measurements performed. Before starting to discuss the actual construction of the THz-STM, we hence quickly want to mention the sample materials used. In general our samples need to be conducting, cleanable to an atomic degree and atomically flat. In this thesis two main sample system were used: Noble metals and transition metal dichalcogenides (TMDCs).

4.1 Noble Metal Crystals: Au(111) and Ag(111)

Due to being chemically rather inert and easy to clean, noble metals are a popular set of sample systems in STM. They are used in form of single crystals grown with high purity and fine polished along a given crystal direction in order to expose a flat and defined crystal surface with high accuracy. In this thesis we use a Au(111) and a Ag(111) surface. We clean these samples in UHV via alternating cycles of neon gas ion sputtering ($1.5keV$, ca. $15min$) and annealing the sample to $900K$. Typically, two to three cycles yield an atomically clean surface with large flat terraces.

Both noble metals are chemically rather inert and crystallize in a face centered cubic (fcc) lattice. However, on the Au(111) surface, a surface reconstruction takes place. While it is still fully fcc in the bulk, on the surface there will be regions of fcc and regions of hcp (hexagonal close packed) as well as the boundaries in between [92]. In STM images, this gives rise to the typical *herringbone* reconstruction (see fig. 4.1) [92].
Due to being easy to work with and well-characterized in the community, these two are very useful basic metallic substrates that will be used heavily within this thesis.
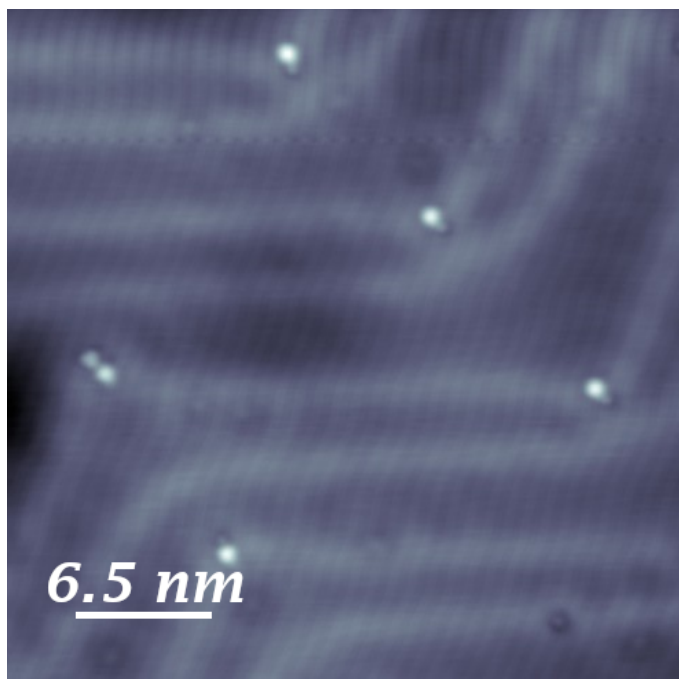
Figure 4.1: Topography of a clean Au(111) surface. The heringbone reconstruction of the surface can clearly be seen. Recorded at 100 mV, 100 pA.

4.2 Transition Metal Dichalcogenides

The semiconducting 2D TMDCs are a material class formed by sandwiching a layer of transition metal atoms between two layers of chalcogen atoms leading to layers of just a few Angstrom thickness. They can form a bulk material as a stack of monolayers bound by Van der Waals forces. [93]

While some of these TMDCs have been of technical use for a long time [94], the material class has only recently become of greater scientific interest. Beside high mechanical sturdiness, especially the electronic properties are of great interest: Unlike the natively ungapped graphene, they mostly exhibit an indirect band gap in bulk and transition to a direct bandgap when prepared in monolayers [95].

In the main part of this thesis, we made use of the properties of one TMDC: A Molybdenum disulfide (MoS_2) monolayer grown on a noble metal substrate. Furthermore, preliminary data was recorded on Molybdenum ditelluride ($MoTe_2$). Since the latter is shown in the framework of an outlook, we will discuss this material only in place.

4.2.1 Monolayer Molybdenum Disulfide and Kondo Defects

a)

b)
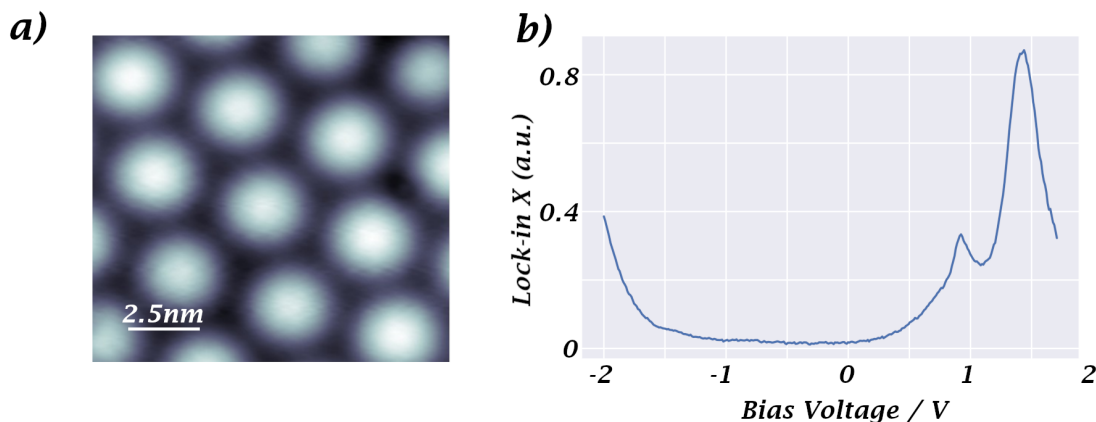
Figure 4.2: **a)** Topography of a small port of an MoS_2 monolayer island on Au(111). The Moire pattern, originating from the lattice mismatch of monolayer TMDC and the noble metal substrate, can be seen clearly. Recorded at 800 mV, 200 pA. **b)** A typical constant-height spectrum of MoS_2 on Au(111). The gap caused by the semiconducting TMDC can be utilized to electrically isolate adsorbats. Feedback opened at 1.75 V, 1 nA.

Growing thin layers of different materials on metallic crystals is a well established technique in STM [96]. Beside investigating the local properties of the layers themselves, they can act as a modification of the electric properties directly on the surface and hence optimize a substrate for the investigation of structures grown on these layers. For example, thin insulating layers, such as MgO or NaCl, are routinely used to electrically decouple adsorbates from the metallic substrate [96–99]. This has e.g. been used to make atomic spin systems accessible to ESR-STM [100]. A single layer of a TMDC can be used to obtain a similar effect: States within the semiconducting gap are electrically decoupled from the substrate. In our group, growing a single layer of molybdenum disulfide on gold or silver crystals is a well established technique and has e.g. been used for the isolation of molecules to study their vibronic modes [101].

We prepare these samples directly inside our UHV preparation chamber based on a known recipe [102]. Using a leak valve, H_2S gas is directed on an atomically cleaned noble metal crystal (see sec. 4.1) resulting in an in-flow pressure of $2 * 10^{-5}$ mbar in the chamber. Using a commercial metal evaporator, molybdenum is then evaporated for about 20 minutes onto the substrate, which is heated to 550 °C. Afterwards we stop the H_2S inflow and keep annealing for 5 more minutes before cooling the sample for transfer. Usually, the sample is annealed to 500°C again on the next day to help remove H_2S residues.

Using this recipe, large single layer MoS_2 islands, with up to hundredth of nanometer di-

ameter, are grown on the sample. Due to the lattice mismatch of the TMDC with the noble metal crystal, the topography of the MoS_2 shows a prominent Moire pattern (see fig. 4.2a) [103]. Spectroscopically a clear gap due to the semiconducting properties of MoS_2 can be seen (see fig. 4.2b) [103].

In this thesis, we will, albeit being a promising approach for future physical systems, not be using the decoupling properties of the MoS_2, but be more interested in the electrical properties of defects in this layer.

The MoS_2 monolayers prepared in our group have a very low density of defects. Nevertheless, different types exist and can be occasionally observed. Typical defects include vacancy point defects for sulfur (either top or bottom layer) or molybdenum [104]. In this thesis we will make use of the electric properties of sulfur top vacancy defects since they can be easily created in a controllable amount by short low-energy (100eV, 15sec) ion gas sputtering (see fig. 4.3a).
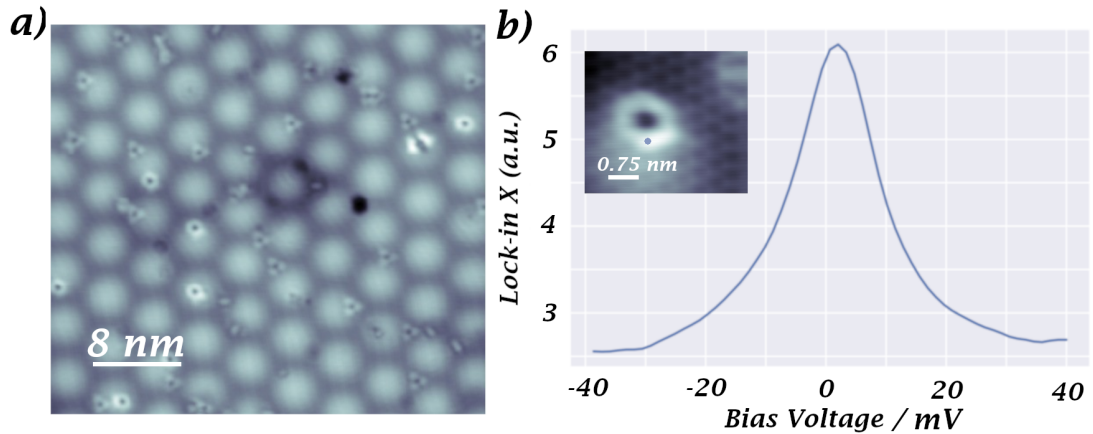
Figure 4.3: **a)** Topography showing a large MoS_2 on Au(111) island. Many defects, successfully created by ion sputtering, are clearly visible. Recorded at 100 mV, 100 pA. **b)** Constant-height spectrum showing a zero bias peak as fingerprint of the Kondo resonance caused by a sulfur vacancy point defect in MoS_2 on Au(111). Inset: Corresponding defect. Feedback opened at 100 mV, 1 nA.

This kind of defect has been shown [105] to carry a spin in similar systems. Spins on MoS_2 on Au(111) can introduce a localized Kondo resonance in the underlying metal surface [106] and the defects are known to do so here as well. A Kondo resonance is a many-body state originating from the screening of a magnetic impurity by the bulk electrons of a metal

[107, 108]. It can be described by the Anderson impurity model and, since it is of great physical interest, has been and is investigated in a myriad of different systems. In this thesis though, Kondo physics will not be relevant and we hence refrain from going into detail here. We will however make use of the fingerprint of this resonance in STS: A peak at zero bias (see fig. 4.3b). This prominent feature, isolated in the semiconducting gap and spatially stable due to being part of a lattice, will be used as a testing system for opening tunneling channels via THz radiation. Spatially, this feature is not isotropic, but dI/dV maps reveal a double-kidney shape (see fig. 5.18c), probably originating from symmetry breaking due to the TMDCs electronic lattice and Moire structure. This distinct shape will be used to validate the real space resolution of the THz-STM.

Having quickly mentioned all samples used in this thesis, as well as the preparation methods, we can now finally begin discussing the construction process of our THz-STM in the following chapter.

CONSTRUCTION OF A THZ-STM

In the previous chapters we introduced a theoretical foundation, the concept of THz-STM and the lab infrastructure as well as the sample systems used. We have hence successfully discussed all surrounding factors and requirements and can finally begin to describe the construction of our THz-STM. In this chapter we will cover the setup of the THz source as well as the characterization of the generated pulses. We will then proceed to discuss our path along coupling the THz pulses to the STM, presenting three milestones, each showcasing a crucial step towards a complete THz-STM. In the end of this chapter, we will have presented the entire construction process and presented first results.

5.1 Generation and Characterization of THz Radiation

As a first step of the construction of our THz-STM we needed to generate the necessary pulsed THz-radiation used as a transient bias. As already discussed before (see sec. 3.1), the generation of radiation in the THz window proved to be more sophisticated than for other wavelengths. Nevertheless, in present times several reliable methods are available. Typical approaches include photoconductive antennas [109], spintronic emitters [110], optical rectification [111] or free electron lasers [112]. A free electron laser, being a large scale research facility, already prohibits itself for use in our experiments. While e.g. a spinctronic emitter can yield an especially broadband THz pulse [113], optical rectification is known to produce THz pulses with especially high pulse energies [114]. Since we expected considerable losses due to long travel distances of the THz beam under atmospheric conditions as well as several optical interfaces throughout the way into the vacuum chamber, this is a considerable advantage. Additionally, handling the higher THz frequencies generated by spintronic emitters, as well as the shorter pump pulses necessary, are experimentally more demanding. Since we do not necessarily need these higher frequencies to reach the desired

sub-picosecond pulse durations, this is a clear downside. We hence decided to settle for the optical rectification approach in our setup.

In this section we will report on the construction of our THz source based on optical rectification, using a tilted-pulse-front pumping scheme, in lithium niobate (LN).

5.1.1 Optical Rectification

Optical rectification is a nonlinear optical effect occurring when high-intensity light travels through a nonlinear material. Since the THz source used in this thesis operates based on this principle, we will quickly outline the principle in the following.

We have already (sec. 2.2.1) discussed electromagnetic fields leading to a polarization of dielectric materials. At this point we assumed the response to be linear with the applied electric field and introduced the linear susceptibility χ_e as proportionality factor. This is essentially justified since the electrons are moved by the applied field in a nearly harmonic atomic potential. For, material dependent, higher displacements caused by large driving fields, the potential can look increasingly anharmonic (fig. 5.1). When hence spectrally decomposing the oscillation performed by an electron in such a potential driven by an incoming electromagnetic wave of a given frequency, components of different frequencies will arise in the response of the polarization. This gives rise to phenomena such as higher harmonic generation, optical parametric amplification, Kerr-effect and the phenomenon of optical rectification used in this thesis [115, 116].

Optical rectification describes a DC response of the polarization of a material when driven by an oscillating electric field. This can be heuristically understood by again looking at the electron in an anharmonic potential: The ground state given by the lowest energy is not necessarily the average position of an electron oscillating in such a potential. The difference between those positions gives rise to the net DC polarization of optical rectification.

More formally this can be express by introducing higher order electric susceptibilities when expanding the polarization response of a material [115]:

$$\vec{P} = \chi_{e,1}\vec{E} + \chi_{e,2}\vec{E^2} + \chi_{e,3}\vec{E^3} + ... \tag{5.1}$$

Due to the higher order susceptibilities being very small, strong fields are required for such a nonlinear response to become relevant. For the effect of optical rectification, it is sufficient to look at the second-order term. As an example how this term leads to a DC response, it is illustrative to look at a very simple harmonic wave $E = sin(\omega t)$ as driving field [115]. When plugging this into the second order term, we find $\chi_{e,2}E^2 = \chi_{e,2}sin^2(\omega t) = \chi_{e,2}\left(1 - cos^2(\omega t)\right)$. We can now apply the trigonometric identity $cos^2(x) = \frac{1}{2}\left(1 + cos(2x)\right)$ and find $\chi_{e,2}E^2 = \frac{\chi_{e,2}}{2} - \frac{\chi_{e,2}}{2}cos(2x)$ The first term is the desired DC response and hence describes the effect of optical rectification. The second term will be of relevance later in this thesis as well: It generates a response with twice the driving frequency. It is hence called frequency doubling or second-harmonic generation [115].

52
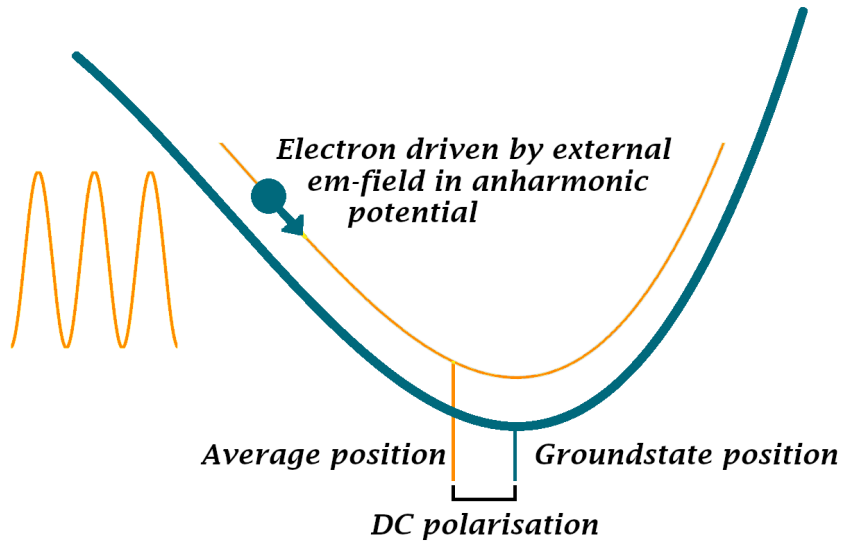
Figure 5.1: Nonlinear optical effects can occur when light interacts with a medium with anharmonic electronic potentials. In such a potential, the average position of the electron changes compared to the ground state when being driven by an external field. This effectively leads to a DC polarization as response to an oscillating field and is hence called optical rectification. Adopted from [117].

We have now discussed how nonlinear optics can result in a DC polarization caused by a strong driving field, such as an intense laser beam. However, the initial goal was generating THz radiation, leaving us with the question how optical rectification can contribute to this. This becomes clear when again thinking about ultrafast laser pulses: When driving a system with such a pulse the DC polarization rises and falls of on extremely short timescales as well. By a suitable choice of pumping technique and nonlinear material, the time-dependent DC polarization can perform ultrashort pulses with THz frequencies [118]. In this thesis we will use this effect as the THz source for our experiments.

5.1.2   Tilted-Pulse-Front in Lithium Niobate

In the last section we fundamentally discussed optical rectification, the nonlinear effect used for our THz source. While this clarified the physics involved, this still leaves several technical difficulties on the path of practically generating suitable THz generation untouched.

In this section we discuss these as well as the principle of tilted-pulse-front pumping and describe how we laid out our THz source.

The first, and most obvious, open question when designing a THz source is the choice of nonlinear material: Fortunately, there are many well-know crystals to select from:

Lithium niobate is a thoroughly studied material and recognized for its strong nonlinear properties [119]. Crystals of high purity, considerable size and with optical polishing as well as coatings are commercially available, making it well suited for our THz source.

There are two different classes of crystals available: Congruent lithium niobate (cLN) pulled via a Czochralski process and stoichiometrically grown crystals (sLN) [119, 120]. While sLN crystals are superior regarding their nonlinear optical properties, they are still reported to be very prone to damage induced by high-power laser radiation [120]. Fortunately, this problem can be overcome by suitable manganese (Mg) doping. In sLN, a Mg doping as low as 0.67-1 mol% is sufficient to greatly improve the optical damage threshold [120, 121]. We hence settled for such a Mg doped sLN crystal for our experiments.

After having chosen a material, the second hurdle for a THz source is how to actually extract THz radiation: While we already discussed how THz frequencies can be generated via optical rectification, it is unclear how to efficiently collect this radiation from an extended crystal. One of the main challenges here is the significant difference between the group refractive index ($n_{gr,1030nm} = 2.3$) for radiation in the visible range and the phase refractive index ($n_{THz} = 4.96$) of THz frequencies in lithium niobate [121–124]. An optical pump pulse will therefore travel through the LN much faster than the generated THz radiation. It will hence not be able to generate co-propagating THz radiation that could continuously build up as the pump pulse travels through the crystal. Instead, analogously to Cherenkov radiation [125], the generated THz radiation will add up to a cone following the pump pulse (fig. 5.2)[123, 126]. Such a radiation cone cannot be easily collected to form a single collimated THz pulse and is therefore of little use for our desired application. Luckily there is a technique allowing the generation of more controllable THz radiation: The tilted-pulse-front pumping scheme [123].

In order to generate THz pulses compact in time and space, the pumping pulse needs to co-propagate with the generated THz pulse. By doing so, the THz radiation, generated via optical rectification by the pump pulse traveling through the nonlinear material, continuously builds up a single spatially compact THz pulse with growing power. In order to achieve this we need to have the pump pulse traveling at the same speed ($v_{gr,vis}$) through the crystal than the THz radiation (v_{THz}). It has been shown that this can be achieved by tilting the pump pulse front by an angle γ [127]:

$$v_{THz} = cos(\gamma) * v_{gr,vis} \tag{5.2}$$

The THz radiation traveling under an angle γ with respect to the pump pulse will hence continuously constructively interfere while other directions will be suppressed. A single THz pulse front, compact and directed in space [123, 128, 129], with high field strength,
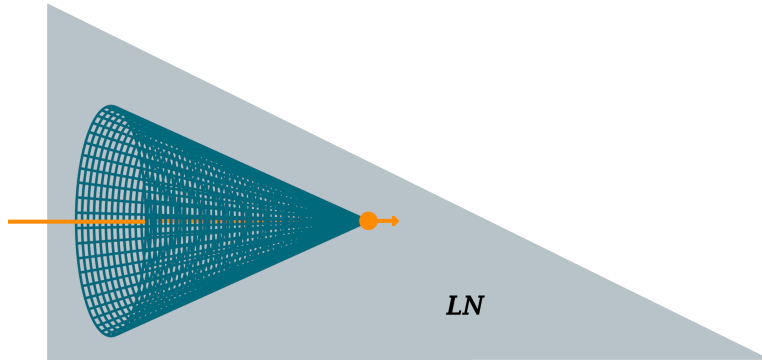
Figure 5.2: A point like pump beam (orange) propagating through a lithium niobate crystal will generate, analog to Cherenkov radiation, THz radiation in a cone shape. The low directionality and the curved wavefront of this cone makes it hard to collect and collimate the THz pulses generated in such a source [123]. Figure inspired by [123].

emerges, making this so called tilted-pulse-front pumping scheme favorable over the simpler Cherenkov scheme [123].

In our THz-STM we hence use tilted-pulse-front pumping. In case of lithium niobate pumped by 1030 nm pulses and using the aforementioned refractive indices, we find $\gamma \approx$ 62.9°. For our THz source we settled for a commercially available [130] 1.3 mol% Mg doped sLN triangular prism with a 62° angle and AR coatings on two surfaces. Such a well-established geometry has the advantage of the THz wavefront being approximately parallel to the surface when leaving the crystal, while the pump beam internally reflects and leaves the crystal in a controlled way (fig. 5.3). This makes it possible to use safely use such crystals with high power pumping beams as necessary for THz-STM.

After having chosen the nonlinear crystal and the pumping scheme, the next step for our construction was planning the wavefront tilt. One of the most straight-forward ways to achieve this, and the one used in this thesis, has already been discussed in section 2.2.4: Pulse-front-tilting using a grating. But this comes at a cost: Since gratings are dispersive optical elements, the frequency components of the pump pulse will spread out spatially. To circumvent this, a telescope made from two lenses can be used to collect the dispersed light and spatially recombine the different wavelength in the lithium niobate (fig. 5.4) [129]. In order to achieve efficient pumping it has been shown that it is optimal to generate an image
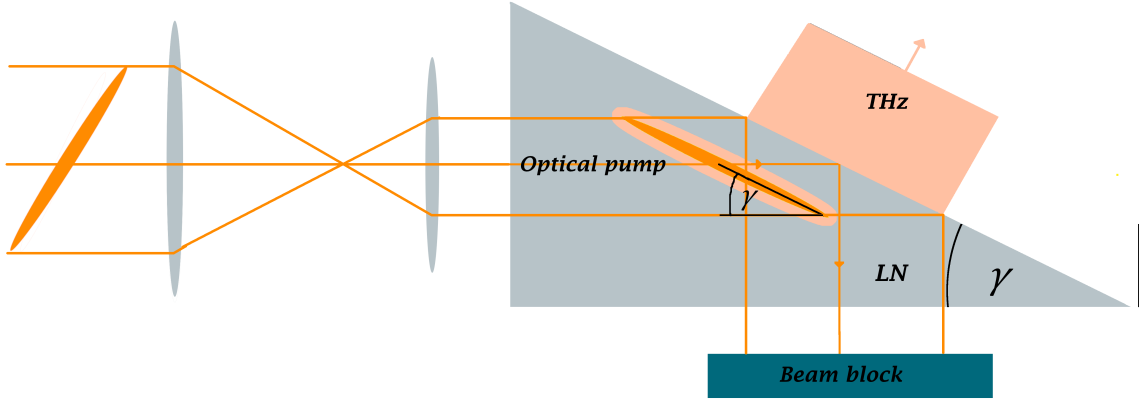
Figure 5.3: In the tilted-pulse-front pumping scheme, the wavefront of the pumping radiation is tilted by an angle γ such that the phase velocity of the THz radiation aligns with the effective group velocity of the pump pulses. This allows for efficient THz generation over an extended crystal while keeping the generated pulses spatially compact and directed [123, 128, 129]. The initial tilt of the wavefront is created using a grating (not shown, see fig. 2.13). It is then altered using a telescope such that the wave front tilt angle in the crystal corresponds to the aforementioned phase matching angle γ. The lithium niobate is cut under the same angle to allow the THz beam to efficiently leave the crystal. Adopted from [129].

of the grating at the edge of the lithium niobate that is tilted with the wavefront angle using the telescope [131]. This leads to minimal pulse duration across it. Furthermore it has been realized that lenses with longer focal lengths are favorable due to the reduction of field curvature [131].

Since the pulse front tilt, image tilt and beam diameter are all changed in combination by the telescope, it is not trivial to find optimal parameters for grating and lenses. Starting from grating and imaging equation, two formulas have been shown to govern the optimization [129, 131]. To attain the desired wavefront tilt γ,

$$tan(\gamma) = \frac{l\lambda}{n_{gr}\beta cos(\theta)d} \tag{5.3}$$

needs to be fulfilled. Here, θ is the diffraction angle at the grating, d is the grating period, l the diffraction order and $\beta = \frac{f_1}{f_2}$ the magnification factor of the telescope composed of lenses with focal length $f_{1/2}$. As before n_{gr} is the group refractive index in the crystal and λ is the wavelength.

56
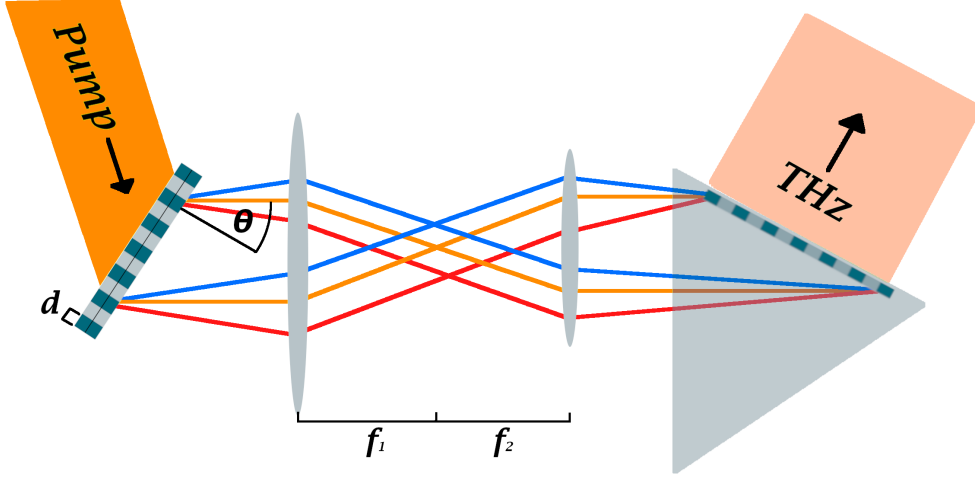
Figure 5.4: The wavefront tilt in our setup is generated by a grating. By additionally imaging this grating into the LN under the same angle as the wavefront (using a telescope), the grating dispersion is compensated at the point of THz generation, leading to the shortest pulses and optimal THz generation efficiency. Graphic inspired by [129]

In order to achieve the correct image tilt, a second equation needs to be satisfied [129, 131]:

$$tan(\gamma) = n\beta tan(\theta), \tag{5.4}$$

with n being the refractive index. To find a matching combination of grating and telescope, the two equations are plotted for different commercially available grating periods [129] in fig. 5.5. Intersections of the two curves are possible configurations. Furthermore, the grating is ideally operated close to its Littrow configuration. In this configuration, the angle of incidence and the refraction angle coincide. Typically, blazed gratings are optimised to yield the highest grating efficiency in this configuration, which is desirable in our case. Finally lenses with matching focal lengths to achieve the desired magnification need to be commercially available.

From this figure we determined a 1600 l/mm grating to be an ideal choice in combination with a $\beta = 0.625$ telescope. Due to extraordinary damage thresholds at affordable pricing, our THz source operates using a UV-fused silica transmission grating. The telescope is based on commercial lenses of 200 and 125 mm focal length, finding a compromise between field curvature and space requirement.

After having theoretically discussed our choice of THz source, we can proceed to describe the construction and alignment process of our THz STM in the following sections.
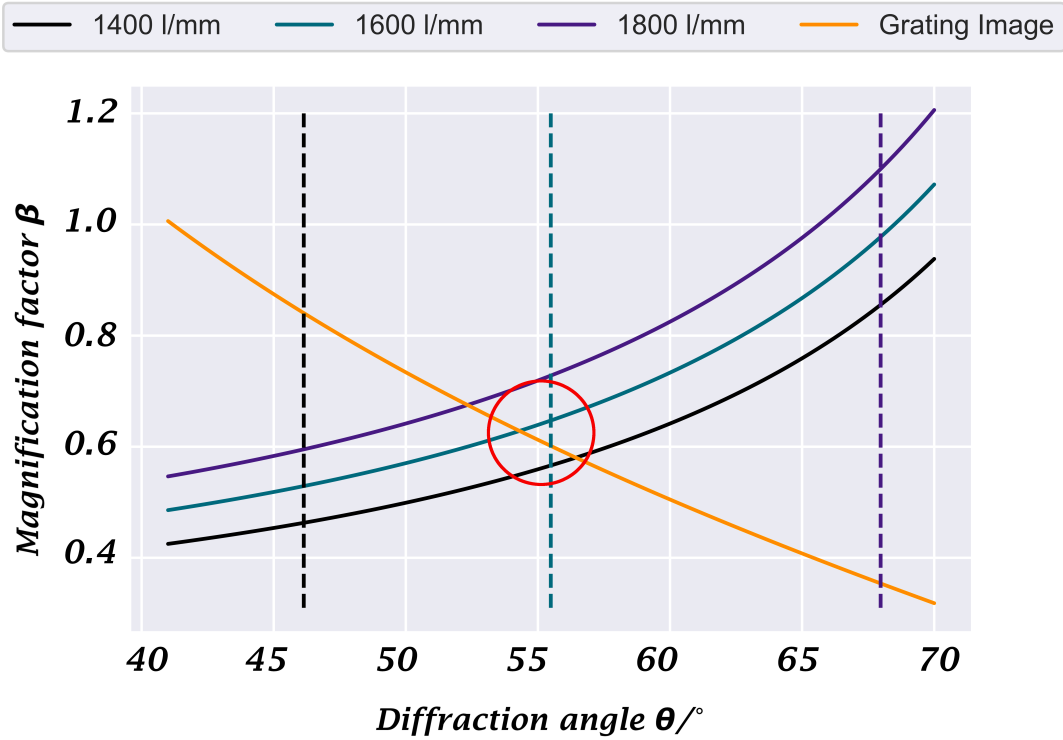
Figure 5.5: To choose the correct grating and lenses, several conditions need to be fulfilled independently. In this plot the necessary conditions for optimal operation of our LN source are plotted following an approach by [129, 131]. The necessary magnification for achieving the desired wavefront tilt is shown for three different commercially available gratings as a function of diffraction angle (eq. 5.3). Furthermore the necessary magnification to fulfill the grating image condition is shown (eq. 5.4). The dashed lines show the Littrow angle for every grating, under which it is supposed to be operated. It is clear that all three curves ideally fall together for a $1600 \frac{l}{mm}$ grating with a magnification factor of slightly above 0.6 (red circle). Plot inspired by [129, 131].

5.1.3 Initial Setup of the THz Source

In the last section we discussed the core element of our optical setup: The THz source generating radiation via optical rectification in lithium niobate using a tilted-pulse-front pumping scheme. In the process we determined and described the optimal components involved in our source. In this section we will now describe the entire optical setup designed around the THz source and describe its building process. Since at the moment we do not need to adjust to certain physical energy scales, we aim for maximum THz pulse energy to ease the detection. Due to the nonlinear process, a linear increase in pump energy results in an exponentially increase in THz energy. Until further notice, we hence performed all following experiments with the 1.25 MHz repetition rate setting of our laser, corresponding to maximum pump pulse energy.

The initial focus of our optical experiment was simply generating THz radiation. Therefore our first setup (fig.5.6) focused on this goal, while keeping flexibility for future applications in mind:

The beam path originates at our commercial 1030 nm fiber laser emitting a collimated beam of 3 mm diameter. Right after the laser, we placed a half-wave plate followed by a thin-film polarizer. The transmission direction allows us to couple out high-power laser beams for future applications, e.g. directing them to the input of our OPA, by adjusting the waveplate. Since no such x-power side-beam was needed in the initial experiments, the waveplate was adjusted such that the entire laser beam gets reflected on the thin-film polarizer. The following element is a periscope increasing the beam height above the table. This is necessary to have sufficient space for the large THz optics later on. In the following a group of mirrors is leveling the beam and walking it towards the STM chamber. One of these mirrors is specifically coated such that a 1% transmission generates a low-power side-beam, which will be needed later. The main beam then encounters another waveplate and thin-film polarizer. This time, the waveplate was adjusted to lead to a 50/50 split: The two resulting beams are used as pump for the desired two THz pulses involved in pump probe experiments. Both of them are sent through two separate telescopes. These telescopes are on the one hand used to reduce the beam diameters to about 2 mm in order to increase the local field strength. This is necessary to reach the high fields needed for nonlinear processes. On the other hand, the telescopes introduce local focii. Those are needed to efficiently place optical choppers upon need.

After the telescope, one beam is walked over a delay stage to allow for a flexible and precisely adjustable delay between two pulses. The second beam is just walked an additional distance in order to set the zero-delay to a fitting position on the delay stage. Afterwards both beams pass another half-wave plate used for independently adjusting the polarization direction of the beams. The beams are subsequently recombined by reflecting them on two mirrors to give them a crossing point in the far distance. They are then walked together through another telescope to further reduce the beam size and finally hit the grating of

the tilted-pulse-front THz source. From here the beams get diffracted and the wavefront tilts. The final telescope, calculated in section 5.1.2, picks up the beams and images the grating into the lithium niobate. The crossing of the two pump beams, at this point having a diameter of about 0.5 mm, was adjusted such that it occurs exactly inside the crystal. There, optical rectification gives rise to THz radiation that leaves the lithium niobate. Meanwhile the optical pump beams get internally reflected and finally leave the crystal. They are then collected safely by a beam dump.

The THz radiation now needs to be collected: While this pumping scheme in principle gives rise to already rather collimated THz beams, our pump spot is far smaller than the THz wavelength leading to diffraction. The resulting beam is directed but strongly diverging and needs to be collimated. In our case, we use a 3-inch diameter, 2-inch focal length parabolic mirror to collect the generated THz pulses by placing the lithium niobate in the focal spot. The large mirror diameter allows for a larger focal length while keeping the covered solid angle constant. A large focal length effectively makes the alignment of the mirror more forgiving since relative misplacements are smaller.

The basic setup described in this section is sufficient for THz generation - if properly aligned. Details on the challenging experimental optimization procedure of the THz source alignment are given in the following section.

Laser

OPA

Delay stage
Periscope
Beamblock
Chopper
Mirror
Half-wave plate
Polarising beamsplitter
Lenses
Grating
Parabolic mirror
Lithium niobate

Focal point
**1030nm pump beam**
Low-power sidebeam
THz beam
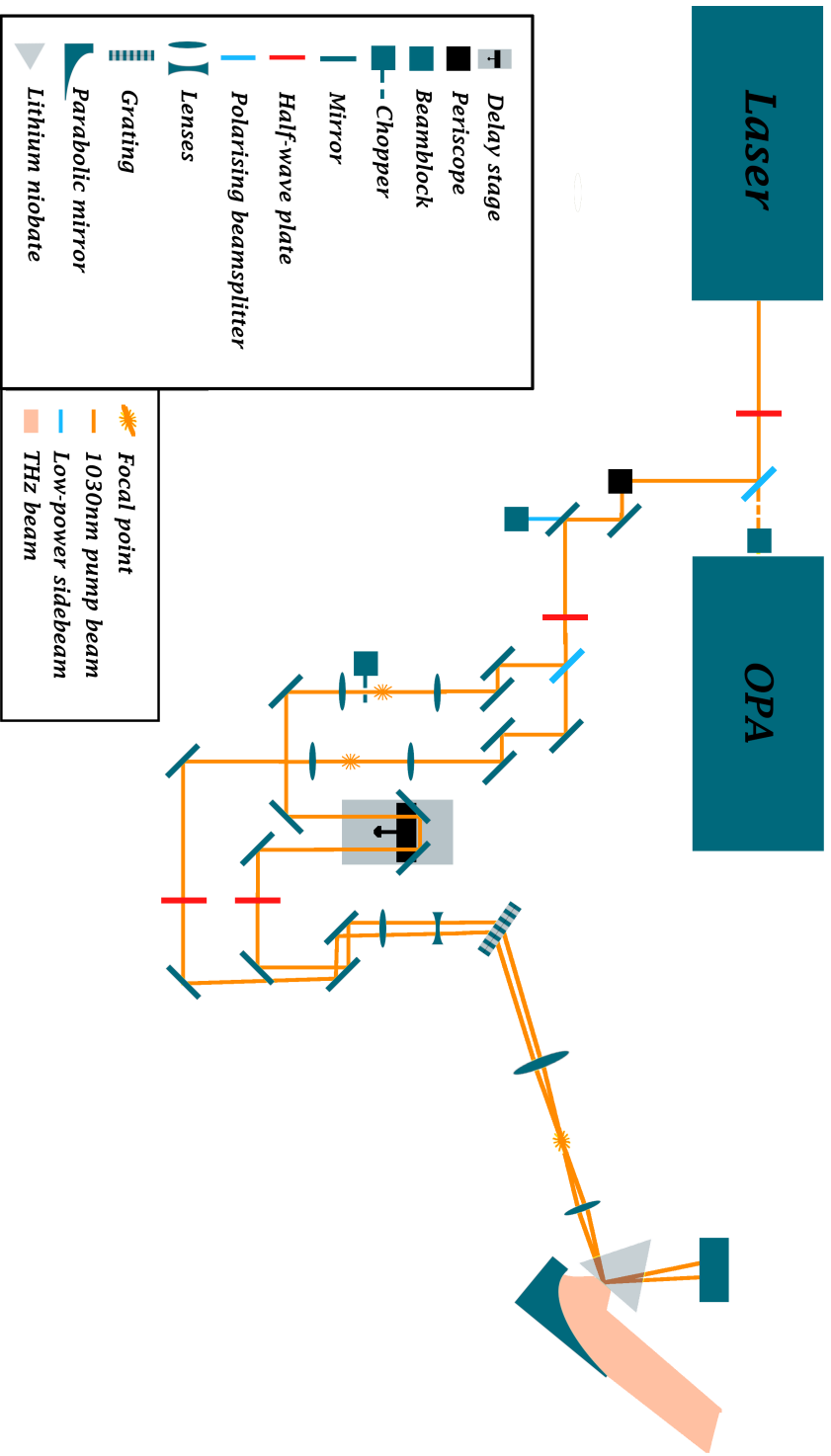
Figure 5.6: First and basic optical configuration of our experiment sufficient for generating and collecting ultrashort THz pulses.

5.1.4 Optimization

In the last section we described the basic optical setup constructed for THz generation. As for any modern optical experiment, high-precision alignment is crucial to achieve the desired functionality. This usually requires a precise measurement of the properties of the laser beam. It is well known in the community how to do so while aligning standard elements such as e.g. mirrors, lenses, delay stages or gratings in the visual and near-infrared range, as used in this thesis. Working with the available viewercards, power meter, beam-profiler camera, autocorrelator and Shack-Hartmann wavefront sensor a precise control of the beam was possible with well-established procedures. We will hence not touch the alignment of these elements here.

In contrast, the alignment directly at and after the THz-source is far more challenging. This is mainly due to the lack of possibilities of beam characterization in this frequency range: THz beams are invisible to the eye and there are only very few and heavily limited technical imaging options available, none of which was available in our lab. The only available way to directly measure the presence of THz radiation in our lab was hence a thermal powermeter with a THz bandpass filter: The filter allows only THz radiation to proceed to the sensor area which absorbs the radiation and by this means thermally determines the average THz power. This leaves questions about beam diameter, divergence and quality unanswered.

Using only this basic measurement possibility, we needed to develop an approach how to still optimize both the THz generation efficiency as well as the properties of the THz beam. We did so by building a splittable breadboard consisting of two separate, specifically cut, pieces tightly screwed together (fig. 5.7). On one of the pieces we placed the large THz-collection parabolic mirror. It is supposed to collect and collimate the incoming THz radiation. In some distance, we then placed another parabolic mirror on the second breadboard piece, focusing the collimated beam down. Finally we placed the THz powermeter at the focus. Using a a visual alignment laser and a lens we simulated the THz source in the visual range and were hence able to precisely align the optical elements.

The alignment process was then performed by, starting from a roughly correct position, translating and rotating the entire breadboard until a maximum in THz power was found. The reasoning behind this is that only a properly collimated and directed beam will be picked up entirely by the second parabolic mirror.

After having found the optimal position of the breadboard, a parameter of the pumping beam was altered: Position of the lithium niobate, rotation of the crystal, rotation of the grating or polarization of the pump beam. Afterwards the breadboard was again moved around to find its new optimal position. The new maximal power either increased or decreased. By iterating this process with all parameters, an optimal THz generation efficiency as well as good beam quality could be achieved. To prevent getting trapped at

local maxima, it is in principle important to roughly sample the entire plausible parameter space, which we did. However, this situation turned out to be overall less problematic than expected: Close to the optimal configuration, which can be achieved by careful pre-alignment, most parameters behave relatively independent.

Having found a sufficiently optimised configuration, the first part of the splittable breadboard was fixed on the optical table. Afterwards the second part got disconnected and removed leaving only the initial THz collection mirror on the optical table.

Using this technique with our two pump beam at 1.25 MHz each and 20 µJ pulse energy, we were able to generate a collimated THz beam with over 16 mW power. This corresponds to about 6.5 nJ THz pulse energy and hence a per pulse conversion efficiency of over 0.3 ‰. When positioning the parabolic mirror, we intentionally slightly misplaced it resulting in a small natural convergence of the THz beam. This will be of importance later when describing the coupling to the STM.

In this section we described our method of fine-aligning our THz source based on a splittable breadboard achieving a well collimated THz beam of sufficiently high power. Nevertheless, beside beam quality and pulse energy, other properties of the THz radiation are of importance for construction and operation of a THz-STM. We will present further characterization of our THz radiation in the following section.
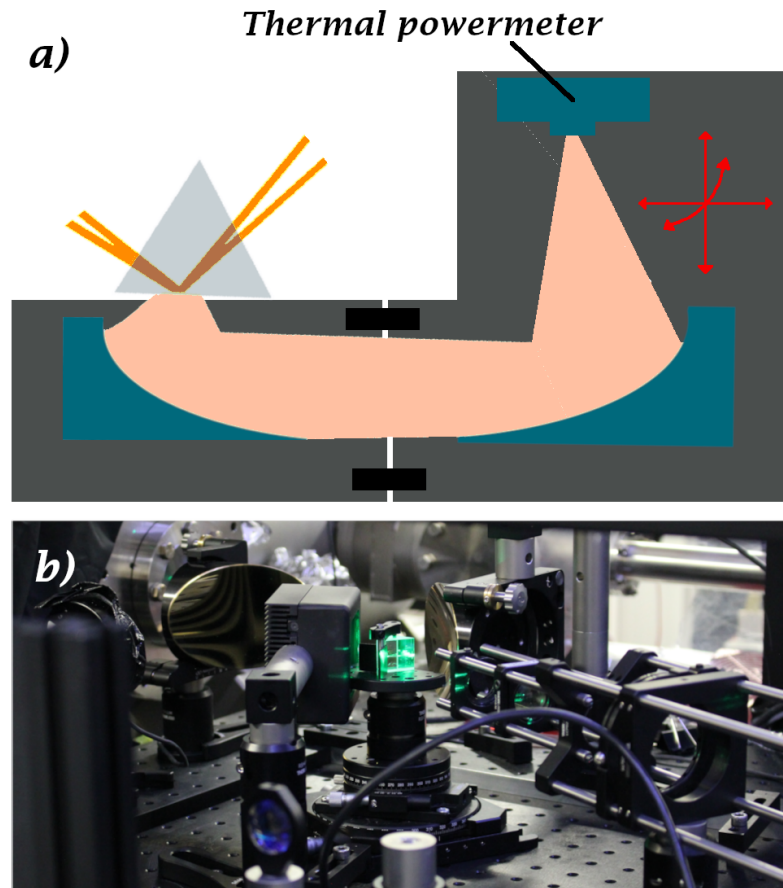
Figure 5.7: **a)** To align the parabolic mirror collecting the THz radiation from the lithium niobate, we mounted it on a breadboard. On this board, a second parabolic mirror focuses incoming collimated THz radiation into a powermeter. We then translated and rotated the entire construction for optimization (red arrows). The maximum power reading indicates optimal alignment. The splittable construction allowed to remove everything beside the desired mirror after completing the alignment. In our setup, we used parabolic mirrors of 3-inch diameter. The first parabolic mirror has a focal length of 2-inch, the second one of 3-inch. **b)** A photography of the same scenario displays the telescope (bottom right) as well as the lithium niobate crystal (central, glowing green). The two 3-inch diameter parabolic mirrors and the THz-powermeter are visible in the background.

5.1.5   Characterization via Electro-Optic Sampling

In the last sections we described the construction and fine-alignment of our THz source resulting in a high THz power in a collimated beam. Even though this already covers two vastly important aspects, another fundamental quantity of the THz radiation is crucial for its application in THz-STM: Since the fundamental idea of THz-STM is opening transient tunneling channels on ultrafast timescales, it is important to know the pulse duration and the actual time-dependent form of the THz field oscillations. Measuring this pulse shape on ultrashort timescales requires a special technique well-known in the THz-community: Electro-optic sampling (EOS). [132]

Electro-optic sampling is a technique allowing to directly measure the time-dependent electrical field and is hence one approach usable to perform THz time-domain spectroscopy. It is based on the electro-optic Pockels effect[132]. This linear electro-optic effect introduces a voltage-dependent change in refractive index to a crystal [133]. Since the electric field of the THz radiation can be seen as such a voltage, an optical readout allows sampling ultrafast THz pulses in the time-domain using a dedicated optical setup. The principle of operation and the necessary components will be described in the following, following a well-established approach [134]:

When a THz pulse and a significantly shorter, linearly polarized optical probe pulse co-propagate together through a suitable electro-optic material, the THz electric field aligning in time with the optical pulse will lead to an electric field dependent birefringence. The resulting different phase delay for s- and p-polarized components of the optical probe pulse introduces a field dependent slight ellipticity in the previously linear polarization [134]. Directly after the electro-optic crystal, the probe pulse is passed through a quarter-wave plate. This effectively biases the polarization such that s- and p- polarization are of equal amplitude - beside a tiny, THz voltage-dependent, difference caused by the just introduced ellipticity [134]. The THz pulse typically cannot pass through standard optical components, such as the quarter-wave plate anymore. Luckily, the instantaneous THz electric field already got imprinted on the optical pulse in the electro-optic crystal and the THz pulse can be disregarded at this point.

The optical probe beam is now sent into a Wollaston prim. This prism spatially separates the probe beam into their s- and p-polarized components. These two beams are then finally focused, using lenses, onto a balanced photodetector. This type of detector, consisting of a matched pair of photodiodes and a transimpedance amplifier, allows to detect tiny differences in the power of two laser beams. It is hence ideally suited to detect the desired phase difference between s- and p-polarization in the two beams of nearly equal power. This phase difference is then proportional to the electric field component of the THz pulse: $\Delta\Phi \propto E_{THz}$ [134]. Since the phase shift angles are very small, the differential current measured by the balanced photodetector is proportional to the phase difference and hence $\frac{\Delta I}{I} \propto E_{THz}$ [134].

By varying the delay between optical and THz pulse and recording the signal, it is possible

to scan the entire THz pulse with high temporal resolution, limited mainly by the probe pulses temporal width.

In order to incorporate electro-optic sampling into our THz setup, we first needed to decide on a suitable electro-optic crystal. While there is a material dependent difference in strength of the electro-optic response, it is more critical to choose a material that allows for thicker crystals resulting in a larger interaction area. The thickness of a crystal used for electro-optic sampling in limited by the different propagation speed of optical and THz radiation in the material. To keep an approximately constant temporal relation between THz and optical pulse throughout the crystal, a material dependent coherence length must not be exceeded [135]. For our 1030nm probe and THz frequencies around 1THz, Galliumphosphide (GaP) is a great choice of material allowing for crystals of over 3mm thickness with a reasonably strong electro-optic response.

In our setup we used the available low power side-beam as a probe (fig. 5.9). To facilitate the necessary variable delay, we directed it over a delay stage. A combination of a half-wave plate and an absorptive linear polarizer allowed us to fine-tune the power and polarization of the probe beam.

The principle of electro-optic sampling requires the two beams to co-propagate and the pulses to temporarily overlap. In order to spatially combine the probe beam with the THz radiation we used a glass plate coated with a conducting indium tin oxide (ITO) layer. This component is optically transparent but highly reflective in the THz regime. We hence placed such an ITO after the parabolic mirror into the slightly convergent THz beam. We then coupled in the optical probe by transmitting it through the ITO from the back. We carefully designed the path length of the probe beam such that it equaled the one of the THz, ensuring temporal overlap. A gold mirror then directed the combined beams towards our GaP crystal that was positioned at a position of a reasonably converged THz diameter. The readout elements were then positioned as described above.

In order to detect small THz signals, a precise adjustment is crucial. This mainly means finding the correct angle of the quarter-wave plate. Without THz signals present, both beams hitting the photodetector need to have the same power and there should consequently be no signal from the detector. Using an oscilloscope to display the signal one can already roughly balance out the beams by rotating the quarter-wave plate. But, albeit the detectors features a matched pair, the temporal shape of the two photodiodes responses is not entirely equal. It will hence not be possible to adjust to an permanently zero signal. Fortunately, this is not a problem: As this technique usually averages over many pulses anyway, it is sufficient for the integral of the detector signal to vanish.

In our setup we reached this by chopping the probe beam before it split and connecting the detector signal to a lock-in amplifier. By choosing a suitable time constant much longer than the pulse repetition rate, a good average was reached. With ideally balanced beams there should be no difference between both beams being present and both being blocked by the chopper blade. We hence further fine-adjusted the quarter-wave plate until the lock-in

66

signal vanished in the background noise.

In order to now actually sample the THz pulses, we moved the optical chopper into the THz pump beam. Using a National Instruments ADC, we recorded the Lock-In signal, now being proportional to the polarization change caused by the instantaneous THz field, as a function of delay stage position. First only opening one pumping beam, we were able to record the temporal shape of our THz pulses. A first long range scan of one THz pulse reveals the general time-dependent electric field form (fig. 5.8a): A large and short single cycle field elongation followed is followed by a far weaker ringing signal lasting several 10th of picoseconds. Two harmonic repetitions of the main oscillation can be seen: Those are most likely internal reflections in the detector crystal. Another long range scan was used to image both THz pulses next to each other (fig. 5.8b). Using a higher resolution scan of the main oscillation cycle (fig. 5.8c), we can see that our THz pulses are well suited for the application in a THz-STM: They are largely single cycle with a main half-cycle pulse duration of about FWHM 640fs. It is hence in principle allowing us to access the desired picosecond timescales using them as ultrafast transient bias in our THz-STM. Fourier transforming such a pulse reveals the spectral components (fig. 5.8d). In good agreement with other tilted-pulse-front lithium niobate sources in the literature [131], our THz region is spectrally located in a broad band mainly below 1 THz. These relatively low THz frequencies will allow us to use more forgiving optical components than would be necessary for higher THz frequencies.

Unblocking the second beam, we were able beautifully track how two THz pulses were generated and the delay between them could be freely adjusted using the delay stage. This measurement was used to get a first idea of the delay stage position corresponding to temporal overlap between the two THz pulses.

In this section we presented how we recorded the temporal shape of our THz pulses using a electro-optic sampling technique. We were able to show that we generated two independent trains of ultrashort, single-cycle THz pulses well suited for use in a THz-STM and identified the delay stage position corresponding to their temporal overlap. With this piece of information, the characterization of our THz radiation is complete. In the following sections we will therefore begin to couple the generated radiation to the STM.
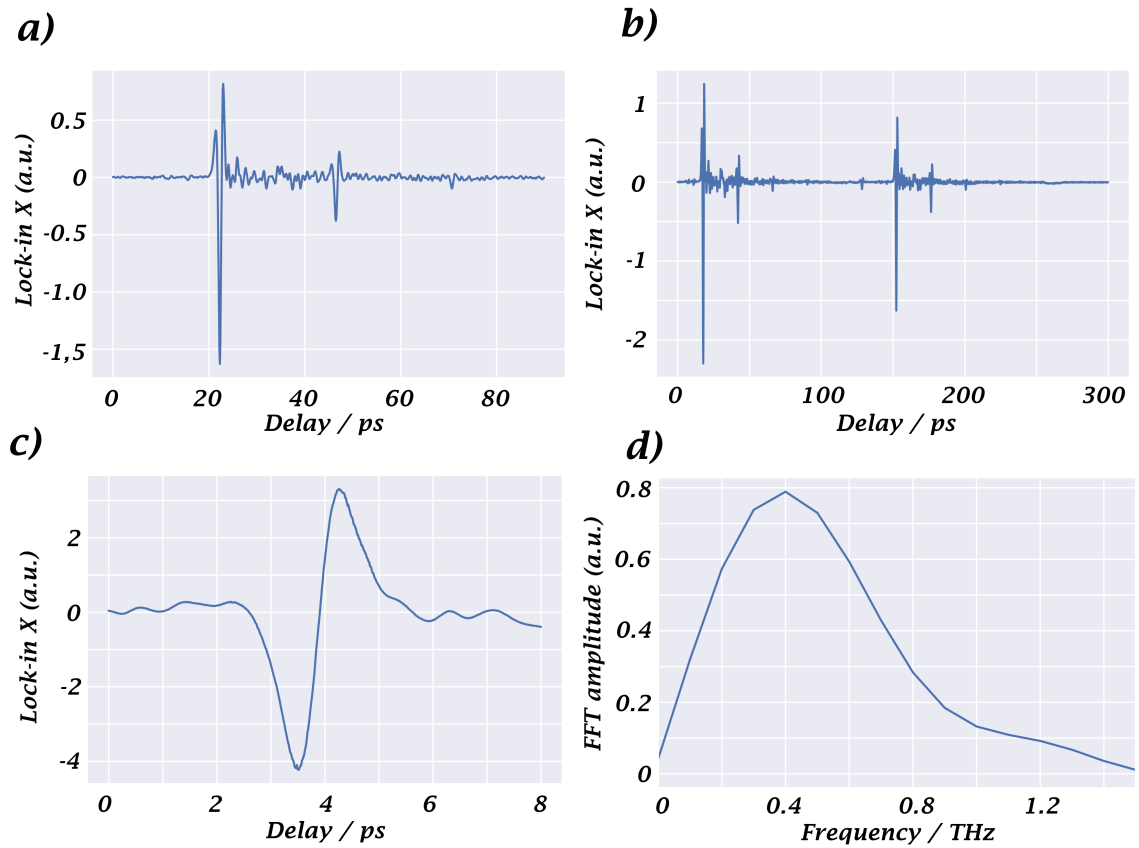
Figure 5.8: **a**) Long-range electro-optic sampling data of our THz pulse. We see that the pulse is large single cycle and strongly raises above the noise level. The harmonic repetitions of the signal are caused by internal reflections in the detector crystal. **b**) Similar data showing both THz pulses with a delay. **c**) Close-up of the main cycle of a THz pulse illustrating the ultrashort duration of FWHM below 1ps per half-cycle. **d**) Fourier transform of zero-padded pulse from c) showing the spectral distribution of our THz radiation. All measurements performed at 1.25MHz rep. rate and by chopping the THz pump beam with about 900Hz.
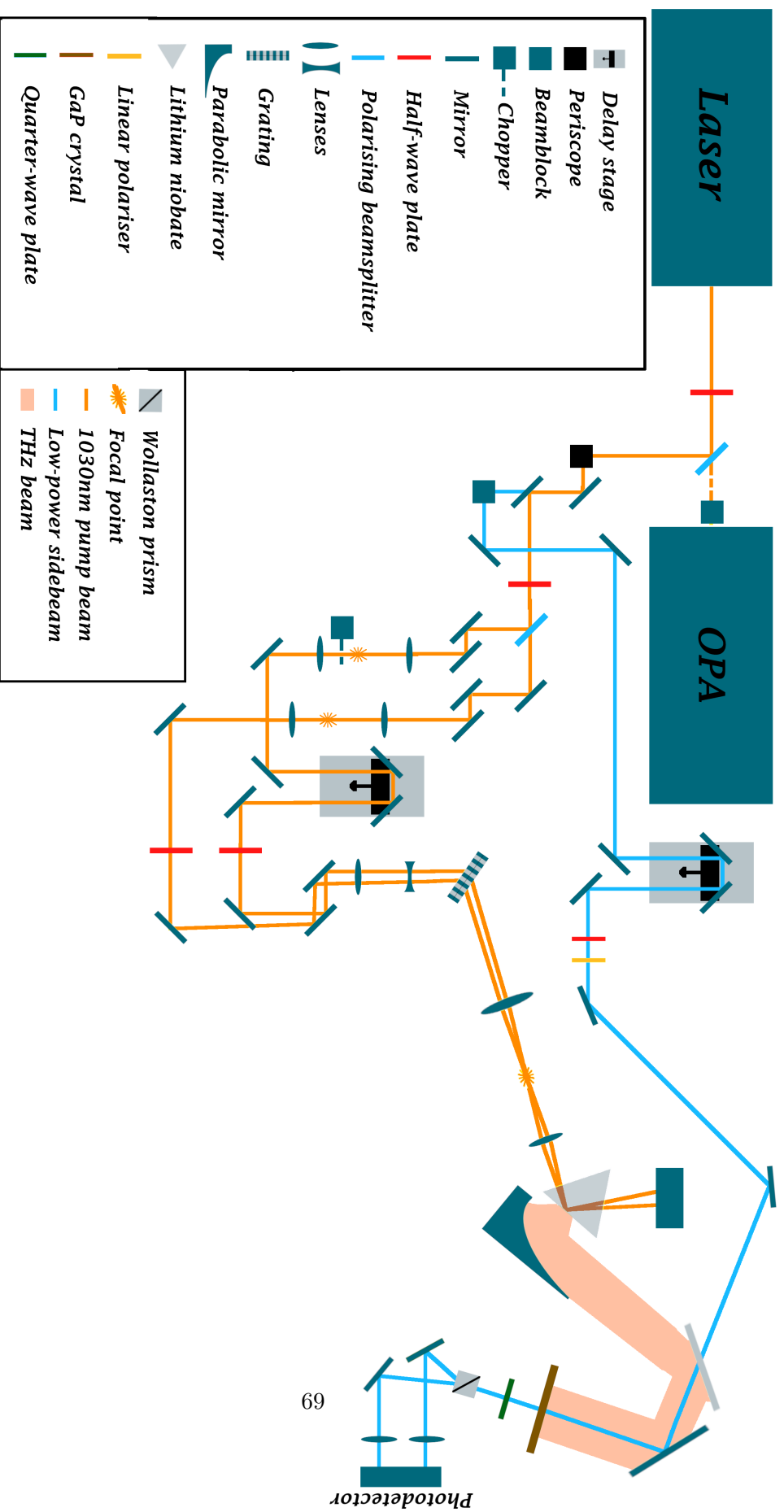
Figure 5.9: Extension of our setup allowing electro-optic sampling to measure the THz waveform.

Legend:

- Delay stage
- Periscope
- Beamblock
- Chopper
- Mirror
- Half-wave plate
- Polarising beamsplitter
- Lenses
- Grating
- Parabolic mirror
- Lithium niobate
- Linear polariser
- GaP crystal
- Quarter-wave plate
- Wollaston prism
- Focal point
- 1030nm pump beam
- Low-power sidebeam
- THz beam

Laser

OPA

Photodetector

5.2 Coupling THz Radiation to the STM: Photoelectron Regime

In the last sections we described the generation and alignment of our THz radiation generated from a lithium niobate source via tilted-pulse-front pumping. Using electro-optic sampling we were able to show that the THz pulses are indeed ultrashort and well-suited for use in a THz-STM. In this section we will now discuss how we introduced the THz radiation into the STM and present the corresponding first milestone: Using photoelectrons we proved the presence of ultrashort THz pulses in the STM junction.

5.2.1 Modification of the STM
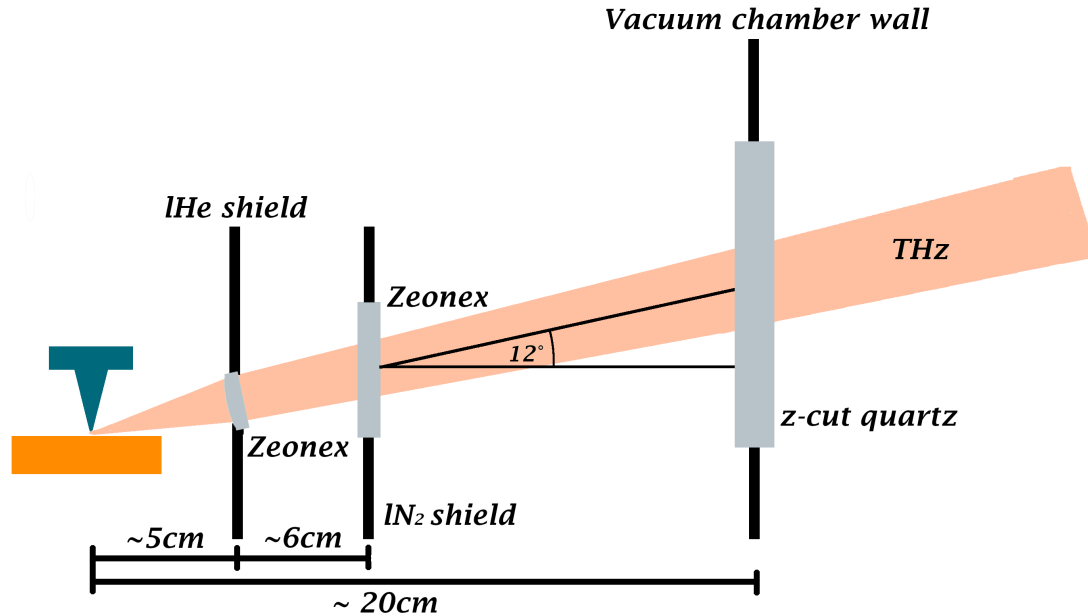
Figure 5.10: Newly constructed optical access to our STM. The radiation needs to pass the vacuum barrier as well as both cryo shields. The vacuum flange houses a 63 mm diameter z-cut quartz window. A Zeonex window is located in the liquid nitrogen shield. The optical access through the liquid helium shield is realized by a 1-inch Zeonex lens with a 2-inch focal length. It focuses the THZ pulses directly into the junction. Overall, the THz radiation needs to travel over 20 cm inside the difficult to access vacuum chamber. Not to scale.

Bringing THz pulses into the STM junction is not trivial. As described in section 3.1, the necessity to cross the barrier to the vacuum as well as to maintain cryo temperatures introduces several interfaces, complicating the project. Furthermore the geometry of the STM head and its radiation shields is complex. Many obstructing structures leave only tight and hard to access free paths to the tip. Threading the THz beam through these structures from outside the vacuum without visual feedback is challenging. Hence, a suitable choice of geometry and window materials is essential for the THz-STMs performance in order to not further hinder the process. Since our standard STM does not feature a THz-compatible optical access (see section 3.2), it was necessary to modify the system and create a new optical access.

We decided to design such an access with an angle of incidence of 12.5 ° with respect to the sample surface (fig. 5.10). Doing so, shadowing of the THz-beam by STM and sample structures is reduced (fig. 5.11) and the bottom plate of the STM head is avoided. Though, to realize this approach, we still needed to remove some blocking structures from the STM head itself. Especially the stop ring of the piezo ring needed to be reworked. Furthermore the radiation shields needed to be modified. Specifically, we mill-cut a hole at suitable height and of fitting size into the helium-radiation shield and introduced a commercial 1-inch diameter, 2-inch focal length lens made from optically polished Zeonex [136]. It is used to focus the incoming THz-beam as tightly as possible onto the tip and made out of optically polished Zeonex. Zeonex is an ideal material for this application: It is highly transparent in the visible as well as in the THz region of the spectrum with a comparable refractive index, keeping dispersion-related offsets of the focal points small. It is effectively blocking the undesired mid-infrared region between 2 µm and 20 µm reducing the thermal load on the microscope. Furthermore it is UHV- and cryo-compatible.
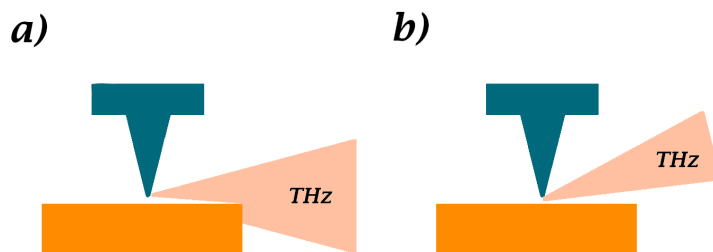

Figure 5.11: A direct horizontal coupling of the THz beam into the STM junction will lead to the sample introducing an obstruction into the beam path (**a**). Approaching the junction under an angle (**b**) allows for a clear path.

On the nitrogen shield, we constructed a shutter, that can be opened and closed. In closed position, it is just solid metal, keeping the thermal load low and hence reducing liquid Helium consumption. In the open position, a flat Zeonex window is enabling access for THz- as well as visible radiation. Finally we placed a new window at a suitable position in the vacuum chamber. This window features a 63mm diameter crystalline z-cut quartz viewport, ideal for the transmission of both THz and visual radiation [137].

With these modifications, the STM is in principle well prepared to be coupled to ultrashort pulses. In the following section, we will discuss our approach of guiding the THz radiation through this newly created access.

5.2.2   Alignment using Photoelectron Emission

Even with the specifically designed optical access available, it is still challenging to guide the invisible THz radiation through the complex geometry into the STM, where there is not enough space for additional measurement devices. To simplify the procedure a guide to the eye as well as a sensitive detection method in the junction are desirable. Furthermore, it has been shown that the antenna properties of the STM tip act as a frequency-dependent filter for THz radiation [72]. It is hence necessary to confirm our pulses are still acting on ultrashort timescales in the STM junction. In this section we will outline our approaches to guide the generated THz radiation into the STM and detect it in place.

It has been shown [72, 138, 139] that photoelectrons can efficiently be driven through a STM junction using THz pulses resulting in considerable, easy to detect currents. In principle the idea is to generate lots of free electrons using the photoelectric effect. In the UHV, those can then be accelerated by the effective voltage of the THz pulse resulting in a net current proportional to the number of generated electrons. Generating photoelectrons requires overcoming the work function of tip and/or sample material. Choosing our Ag(111) substrate (see sec. 4.1), 4.5 eV need to be supplied by the photons [140]. The work function of the polycrystalline tungsten tip, covered by silver at the apex by crashing it into the sample, is harder to quantify. Though, related data from literature suggests that it might be expected to be around 4 eV [141].

The energy of our 1030nm photons is about 1.2eV. Hence, a 4-photon process would be necessary to generate photoelectrons. While those are definitely possible, they require very high laser fluences. This is very disadvantageous for the stability of the STM and the integrity of the vacuum. Furthermore the 1030 nm radiation is still invisible to most standard cameras. Therefore we decided to set up a second harmonic generation to obtain 515 nm photons. These 2.4 eV photons allow for a far more efficient 2-photon photoeffect and are readily visible as green light. Since we still expected significant heat input and no tunneling contact is needed for this approach, these experiments were performed under room temperature conditions.

As already mentioned in section 5.1.1, second-harmonic generation is a non-linear opti-

cal effect generating photons of twice the frequency of the pump beam. This standard procedure is well-established using different non-linear crystals. In our case we chose a commercial beta barium borate (BBO) crystal, as it is a well-studied and strongly performing standard material for this application [142].

To establish a second-harmonic generation in our setup, we dismantled the side beam constructed in section 5.1.5. We then walked the available high-power side-beam, originating directly after the laser at the initial beamsplitter, through a telescope. By shrinking the beam diameter to 1 mm, the energy density increased which lead to a stronger non-linear response. The beam was then sent through a half-wave plate followed by the BBO crystal. A dichoric mirror then reflected the 1030 nm pump into a beam block letting the frequency-doubled radiation pass freely. A following narrow bandpass filter further rejected the 1030 nm radiation. We then walked the new 515 nm beam over a delay stage to allow adjustment of the pulse delay. Finally a set of half-wave plate and absorptive linear polarizer was used to make the power adjustable. The beam was then carefully combined with the THz radiation such that both beams co-propagate by passing it through the ITO under the correct angle (fig. 5.14). After optimizing the waveplate angle in front of the BBO we generated around 500 mW of green light using a 10 W pump beam, corresponding to a conversion efficiency of about 5%.

This combination of green and THz light allowed to use the latter as a guide for aligning the former. We hence reduced the power of the green laser to about 1 mW to use it safely for this purpose. A silver mirror after the ITO was then roughly adjusted to direct the visible green, and invisible THz, beam through the windows into the STM. While this already gives a good first orientation, there is no direct sight along the beam necessary for the fine adjustment into the tiny STM junction. To help with this, we placed a 50/50 beamsplitter right before the window in the vacuum chamber. While the THz was blocked by this beamsplitter, the green laser passed and still traveled into the STM. This beamsplitter now allowed to place a camera to directly observe the STM junction, looking along the lasers path (fig. 5.12).

Using this configuration we precisely positioned the focal point of the green laser on the STM tip using the final silver mirror (automatically moving the THz beam along as well). We then moved it down along the tip until it reached the junction. At this point, we expected being close enough to the junction to be able to generate at least some photoelectrons inside.
In order to measure a current resulting from these photoelectrons, a bias voltage needs to be applied. By choosing its sign, we select photoelectrons flowing from tip to sample (positive voltages) or vice versa (negative voltages). It turned out our focal spot inside the STM was too big to selectively excite photoelectrons on the tip. Since generating photoelectrons on tip and sample at the same time can lead to distortion of the measurements e.g. due to
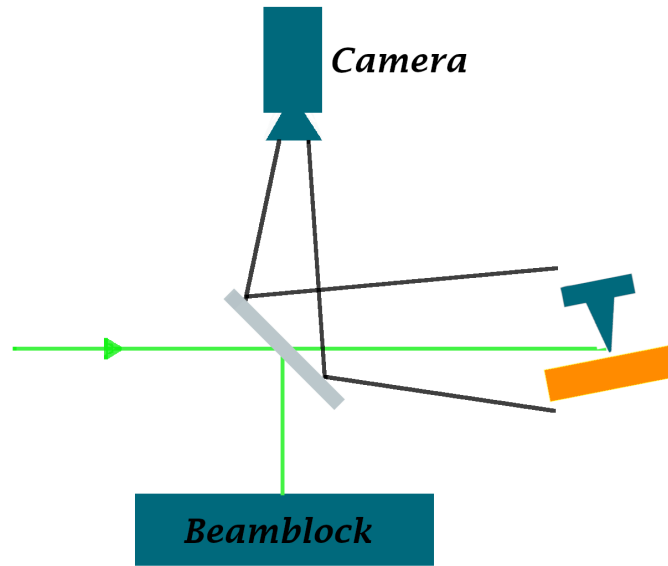
Figure 5.12: Using a beamsplitter and a camera we observe the STM junction from the front while simultaneously shining in 515 nm radiation. This allows to efficiently align the laser focus on the tip apex.

THz streaking [72, 138], we choose to optimize on photoelectrons generated at the sample side of the junction. Therefore, we set the bias to a negative value of -6V, accelerating possible photoelectrons from the junction to the tip. We then brought the STM into tunneling and directly retracted it by around 500 steps (several 100 nm) to establish a controlled junction. Finally we removed the beamsplitter, blocked the THz pump and increased the power of the green laser to 400 mW. We directly noticed a current in the order of a few picoamp. By doing very tiny adjustments to the position of the focal spot, we were able to optimize this to several nanoamp. We then proceeded to record bias dependent spectra (fig. 5.13a) of the photocurrent. Nearly no photocurrent was detected at positive voltages, indeed verifying that photoelectrons nearly exclusively originated at the sample side. For increasing negative voltages, the photocurrent quickly increased to large currents before forming a plateau, verifying that we indeed have plenty of photoelectrons available.

It was then finally possible to try to detect THz radiation in the junction. We unblocked one THz pump and included the chopper into it at the focal spot of the first telescope. Using a lock-in amplifier connected to chopper and tunneling current, we identified changes in current caused by the presence of THz pulses in the junction. Since this can only happen when THz pulses and optical pulses temporally coincide in the junction, the path lengths of both beams need to be equal to a high precision. We therefore recorded the lock-in signal
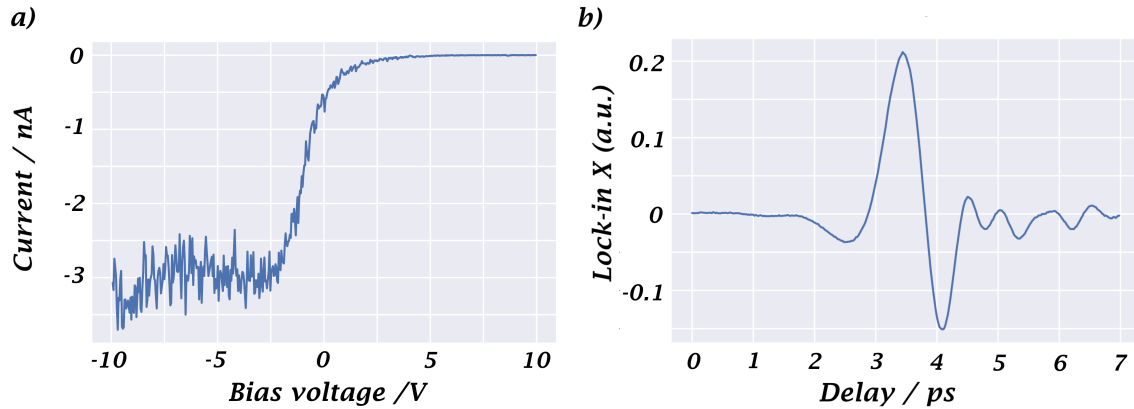
Figure 5.13: **a**) Voltage dependent photoemission spectra under 400mW (measured outside the vacuum window) 515 nm illumination with the side-beam of the STM junction, tip 500 piezo steps (several 100 nm) above tunneling regime. High currents at negative bias compared to nearly none at positive ones confirm the photoelectrons exclusively originating at the sample site. **b**) Delay dependent measurements using a THz and the 515 nm pulse at -6V bias. The photocurrent due to the THZ bias leads to a lock-in signal if both pulses coincide in the junction. This allows to sample the THz pulse in the STM with the much shorter optical pulse. The general shape and timescale of the EOS measurements is preserved with a main half-cycle FWHM of 550 fs. Recorded at 1.25 MHz rep. rate, THz pump beam chopped close to 900Hz, lock-in time constant: 500 ms

as a function of the position of the delay stage in the path of the green laser. And indeed we found a small lock-in signal possibly corresponding to THz radiation in the junction. To optimize, we left the delay stage at the assumed overlap position and maximized the lock-in signal by moving the THz pulse via adjustments at the ITO (which has the advantage of leaving the green beam unaffected). Doing so we were able to greatly increase the signal. At this point the signal to noise ratio was good enough to sample the pulse with finer temporal resolution (fig. 5.13b). Showing features of shape and with timescales comparable to the results obtained via electro-optic sampling (see sec. 5.1.5), these measurements clearly verify the presence of our THz pulses! We can directly verify as well that their ultrashort character is preserved in the junction with a FWHM of the main half-cycle of 550 fs. While it is possible to analyze these curves to great detail and actually infer on the THz near-field present in the desired tunneling regime, there are many technical challenges and a high degree of precision is necessary [72]. Difficulties were e.g. readily visible in the unexpected strong voltage dependence of the shape of the sampling curves. Optimizing such an experiment is hence far beyond the scope of this thesis, that is aiming on the tunneling regime. We instead repeated the above measurement for the fine alignment of our second THz beam and decided to quickly move on to the tunneling regime.

In this section we were initially aiming at using a photoelectron-based THz signal as an alignment help to precisely focus the THz pulses into the junction in a controlled fashion. This was clearly successful. Using this technique we were able to show that our THz beam indeed passed all three window structures and reached the STM junction. We verified as well, that these pulses are, as expected, still living on ultrashort timescales. We hence reached our first milestone during building a THZ-STM: Bringing THz pulses into a STM.

Laser

OPA

STM

Legend:

- Delay stage
- Periscope
- Beamblock
- Chopper
- Mirror
- Half-wave plate
- Polarising beamsplitter
- Lenses
- Grating
- Parabolic mirror
- Lithium niobate
- Dichoric Mirror
- 515nm filter
- ITO

- BBO
- Linear polariser
- 515nm beam
- Focal point
- 1030nm pump beam
- Low-power sidebeam
- THz beam
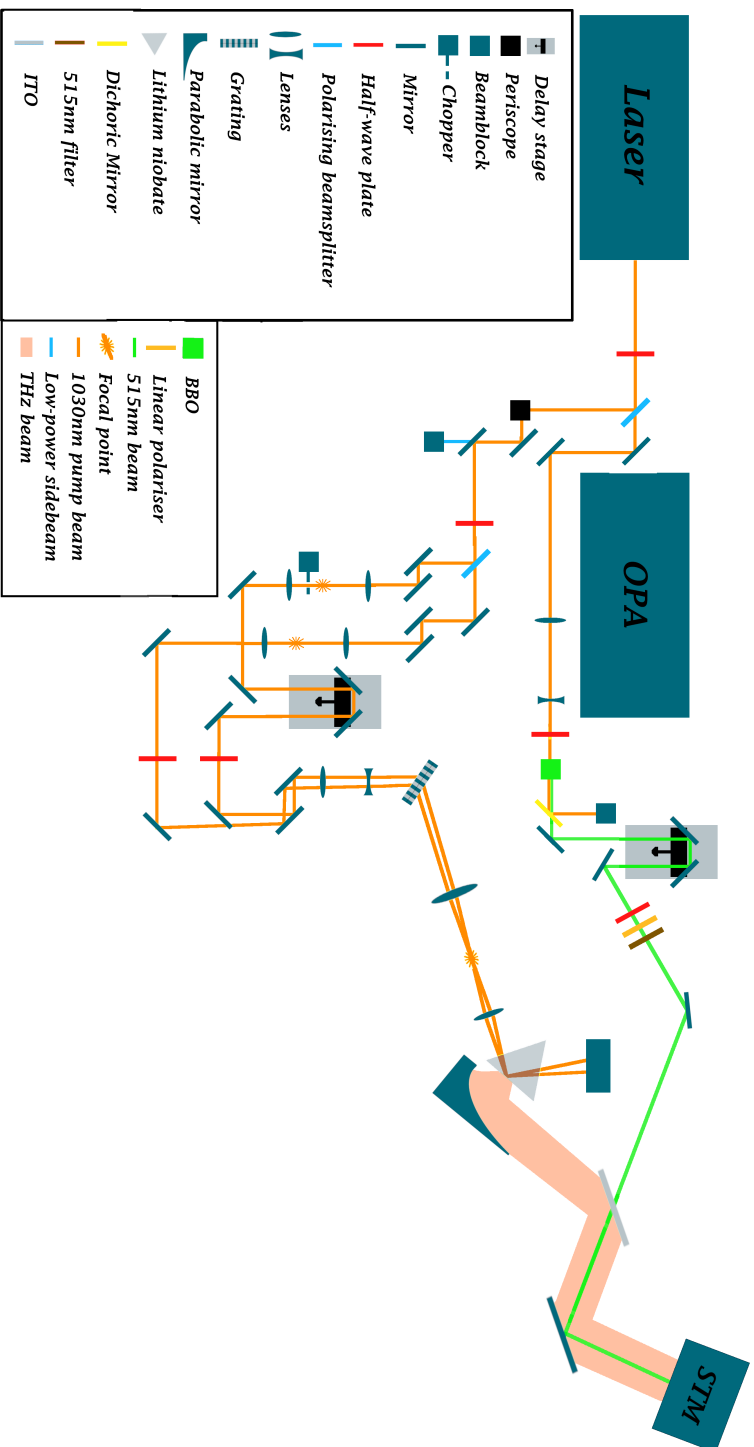
Figure 5.14: Extension of our optical setup by a second-harmonic generation in BBO to allow efficient generation of photoelectrons in the STM

5.3 Coupling THz Radiation to the STM: Field-Emission Regime

In the last section we successfully reached a crucial milestone of the construction of the THz-STM: We were able to show that we spatially inserted ultrashort THz pulses into the STM junction. Though up until here we only worked at large junction distances up to the µm regime outside of tunneling. While we included THz radiation into a STM and performed measurements with its electronics, we can hardly claim having actually performed STM measurements.

So in a next step we need to actually bring the tip close enough for electron tunneling to take place. The necessary stability required us to perform these experiments under cryo conditions. The following experiments were hence performed with liquid helium cooling. The optical setup is identical to the one previously used, but we directed no laser power into the 515nm path.

5.3.1 Field-Emission Resonances

In this section we try to go another step towards the realization of our THz-STM: Measuring a THz induced current in tunneling distances. In the previous experiment we used a second pulse to sample the THz pulse in time. In an actual THz-STM measurement, only the integrated current caused by a single THz pulse can be used as probe - the other pulse is already in use as pump. Since the signals in THz-STM are typically very small, the transient THz voltage should cause as many additional electrons to flow as possible in order to beat the noise level. This is the case for marked I-V nonlinearities, corresponding to high-values in dI/dV - spectra: A small change in voltage leads to a big change in current. Especially since our THz pulses are made up of both positive and negative voltage components, a significant non-linearity ensures that those two contributions do not cancel out (fig. 5.15).

At this point during the construction of our THz-STM we were interested in signals as large as possible to ease the construction process. One of the strongest nonlinearities available in small tunneling junctions is caused by field emission resonances [143, 144]. Field emission occurs when strong electric fields allow electrons to escape into free space e.g. via tunneling. In an STM, when the STM junction is biased with voltages corresponding to energies above the work function, the tunneling electrons become energetically allowed in parts of the vacuum barrier. In this area, the electronic wavefunction can form a standing wave with its reflection for suitable combinations of energy and size (fig. 5.16a)(18). In these configurations the field emission current is especially efficient leading to an oscillating behavior in the I-V curves (fig. 5.16b). This phenomenon is then called field emission resonances (FER).
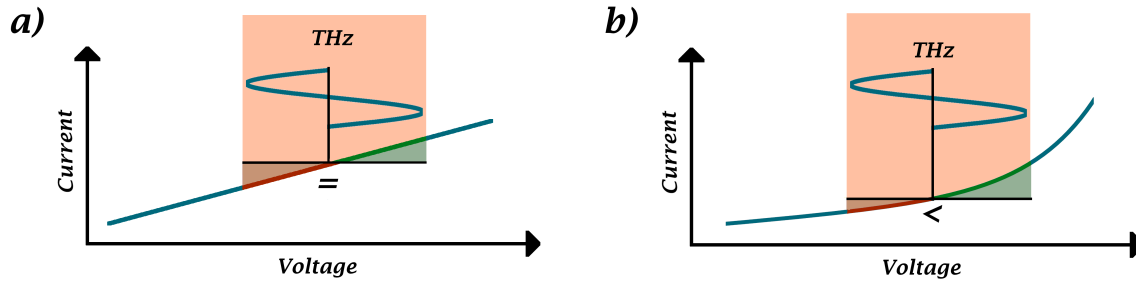
Figure 5.15: In order to imprint a signal to the measured tunneling current, the temporal integral of the I(V) curve over the transient THz bias needs to be non-zero. For a nearly symmetric THz pulse a nonlinearity is beneficial to increase the THz-induced current.**a**) A symmetric THz pulse will not lead to any additional current when acting on a linear I(V) since the ultrafast increase and decrease in current cancel out. **b**) When acting on a non-linear I(V) curve, a symmetric THz pulse will still generate additional current.

Due to their exceptionally strong non-linearity, their stability and to being easy to access experimentally, field emission resonances are an ideal choice as a model system to showcase THz-induced currents in tunneling junctions. There is just one downside: In a strict sense, FER are not based on direct tunneling but on field emission and hence ultimately are not a proof of a working THz-STM. We anyways decided on this system as a first test. We again prepared an Ag(111) sample via sputtering and annealing leading to an atomically clean preparation (see sec. 4.1). We brought the sample into the STM with closed THz shutter, corresponding to a base temperature of about 5K. Via repeated controlled crashing of the tip into the sample as well as voltage pulsing and sweeping we formed a spectroscopically stable tip. Recording I-V spectra revealed the presence and energy of field emission resonances for a given setpoint. After having prepared the sample system like this, we opened the THz shutter with the laser still being off. The base temperature increased until it saturated at about 9K after roughly one hour. At this point everything was ready to introduce THz radiation again.

We then proceeded to open the chopped THz beam aligned in the last section in order to introduce pulses into the junction. The temperature rapidly started rising to above 20 K. This was not only very problematic since it is basically forbidding to perform stable low-temperature measurements in the future, but also unexpected: The absorption of THz radiation should be low and the power introduced was small to begin with. Upon further analysis we noticed that tiny amounts of stray pump radiation escape the lithium niobate in such a way that it gets collimated together with the THz beam and gets focused in the junction. To prevent this we needed to introduce a THz-pass/IR-block filter. Since such filters were not commercially available in the desired 4-inch-diameter size in a reasonable
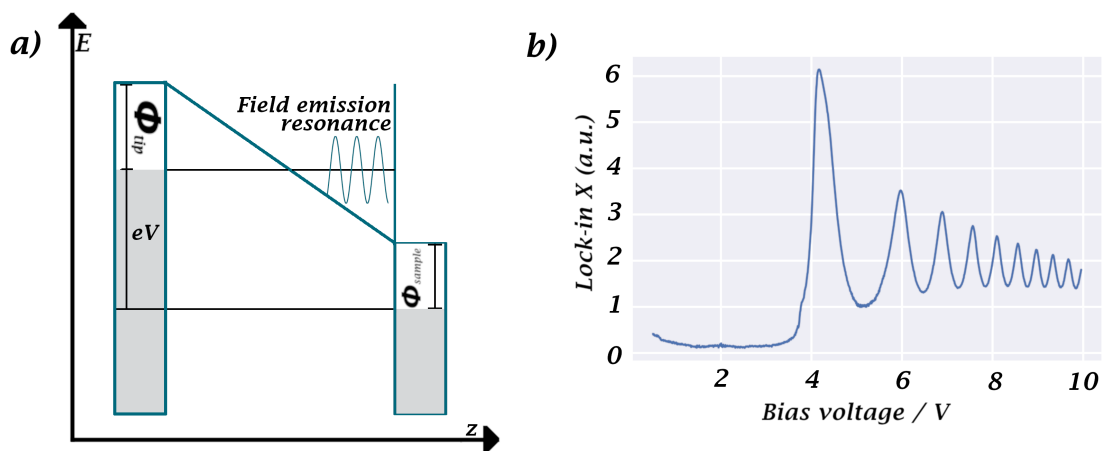
Figure 5.16: **a**) When a high bias voltage approaches the work function of sample and tip material, electronic states of this energy can become classically allowed in parts of the tunneling junction. At given combinations of junction size and bias voltage, the electronic wavefunction can form a standing wave in this area and allow electrons to resonantly tunnel through the junction. Adopted from [145]**b**) dI/dV (V) spectra showing the typical oscillatory features corresponding to field emission resonances. Recorded as constant-current spectrum using a lock-in amplifier. Current setpoint = 5nA.

timeframe, we decided to identify a suitable filter material on our own. For this we bought high density polyethylene (HDPE) sheets from the local hardware store. This material is known to be visually opaque, but highly transmissive for THz frequencies [146] and can hence work as a potent THz bandpass filter. Since visual inspection already revealed very different material quality, we bought severals sheets from different manufacturers. THz transmission was then determined by Oliver Gückstock from the group of our cooperation partner, Prof. Dr. Tobias Kampfrath. There were indeed marked differences in THz-transmission (albeit less relevant at the low THz-frequencies used in our setup). This allowed us to identify the ideal batch of HDPE, which we then cut in shape and positioned as a filter material directly after the parabolic mirror. Additionally we placed a THz wire grid polarizer directly after the filter in order to make the THz power tunable.

Having performed these modifications, we attempted again to introduce one of our two THz beams to the cold STM: This time the temperature barely rose and stayed well below 10 K. We noticed barely any decrease in stability during scanning or spectroscopy. With these ensuring observations we started chopping the THz pump beam at frequencies slightly below 1 kHz and tried to detect correlated changes in the tunneling current. And indeed when sweeping the bias and recording the lock-in signal a clearly bias-dependent signal far beyond noise level could be observed (see 1.25 MHz curve in fig. 5.17b) . Though

it seemed to correlate only loosely with the shape of the field emission resonances. The reason became evident when increasing the repetition rate of the laser: By doing so, the THz pulse energy exponentially decreases leading to smaller THz-induced voltages. The lock-in signal proportional to THz-induced change in current now started to clearly resemble the field emission resonances as seen in normal dI/dV spectra with an offset: The signal rose well before the field emission resonances in the dI/dV and dropped back to nearly zero around their maximum. This is in good agreement with the expected behavior: Due to the THz voltage, the FER become energetically accessible more early. Furthermore, since the THz pulse features voltage regions of both signs, the additional THz current averages out to zero around the maximum of the FER. Having seen these signals, it became clear why we did not resolve the FER with the initial high THz pulse energy: The THz voltage was just to large to resolve the oscillations.

Deducing the time-dependent voltage caused by the THz pulse is not possible from this data without knowing the exact pulse shape before. Fortunately, we do not need to know this voltage curve to proceed. Since we already know the pulses are largely single cycle, it is sufficient to know the size of the main elongation to open tunneling channels in a controlled way. In our recorded data, the offset between the onset of the FER signal between dI/dV- and THz-lock-in signal is a way to estimate the THz voltage amplitude even without knowing the exact waveform: The signal in the THz-lock-in starts to rise exactly when the maximal THz field elongation plus the applied DC bias equals the DC bias for the onset known from the dI/dV spectra (see fig. 5.17a).

In the following we recorded spectra for a broad set of repetition rates (fig. 5.17a-b) and were able to verify the expected trend: With increasing pulse energy the THz voltage amplitude, read off of the distance between FER in THz-lock-in signal and dI/dV, decreased. From this data we were able to estimate that, depending on the repetition rate, we are able to generate effective THz bias voltages of up to an estimated several volts at 1.25 MHz repetition rate and down to few mV at 40 MHz. Especially seeing a signal at 40 MHz was very ensuring: During actual physical THz-STM measurements the voltage modulation needs to be restricted such that it energetically only opens a tunneling channel to the time-dependent feature to be probed making very large THz amplitudes unnecessary. Those would of course yield additional THz-induced current. But this current would not correspond to the previously pumped feature under investigation and hence not contribute to measuring its timescales. In order to still generate high enough currents to beat the noise level, the THz-STM measurements need to be performed at the highest possible repetition rate still delivering enough voltage amplitude to cover the feature. Having shown that even in the 40 MHz mode THz current signals are clearly visible, we have a strong position to access most features at the highest possible repetition rate of our laser. Of course these values must not be taken as absolute but more as orientation for routinely achievable voltages. The actual voltage amplitude in a given measurement setting depends heavily on tip geometry, tip position, energies used in the pump beams and their fine alignment.

81

While we initially feared not to achieve high enough THz voltage amplitudes to be able to use the highest repetition rates, we now face the opposite problem: For many applications the THz voltage amplitudes achieved at the highest repetition rate will still be too large to exactly probe energetically sharp features. Luckily there is an easy solution already installed in the beam path: Using the wire grid polarizer we can freely tune the THz power. Since the tip itself acts as an s-polarization filter, this effect is even stronger pronounced. To verify this we recorded spectra while stepwise detuning the polarizer: Indeed we were able to reduce the THz signal continuously until it vanishes in the noise level (fig. 5.17c). At this point we have shown that we can generate quite significant THz induced voltages by coupling our pulses into a cryogenic tunneling junction while maintaining the stability and temperature to perform STS. Using the wire grid polarizer we can freely tune these voltages. In combination with the information on the THz pulse duration inside the STM gained via photoelectric effect-based measurements (see sec. 5.2.2), one could come to the conclusion that our THz-STM was proven to be fully operational at this point. And while we were indeed very close, further aspects needed to be tested. Most importantly: Pulse duration under cryogenic and tunneling gap conditions.
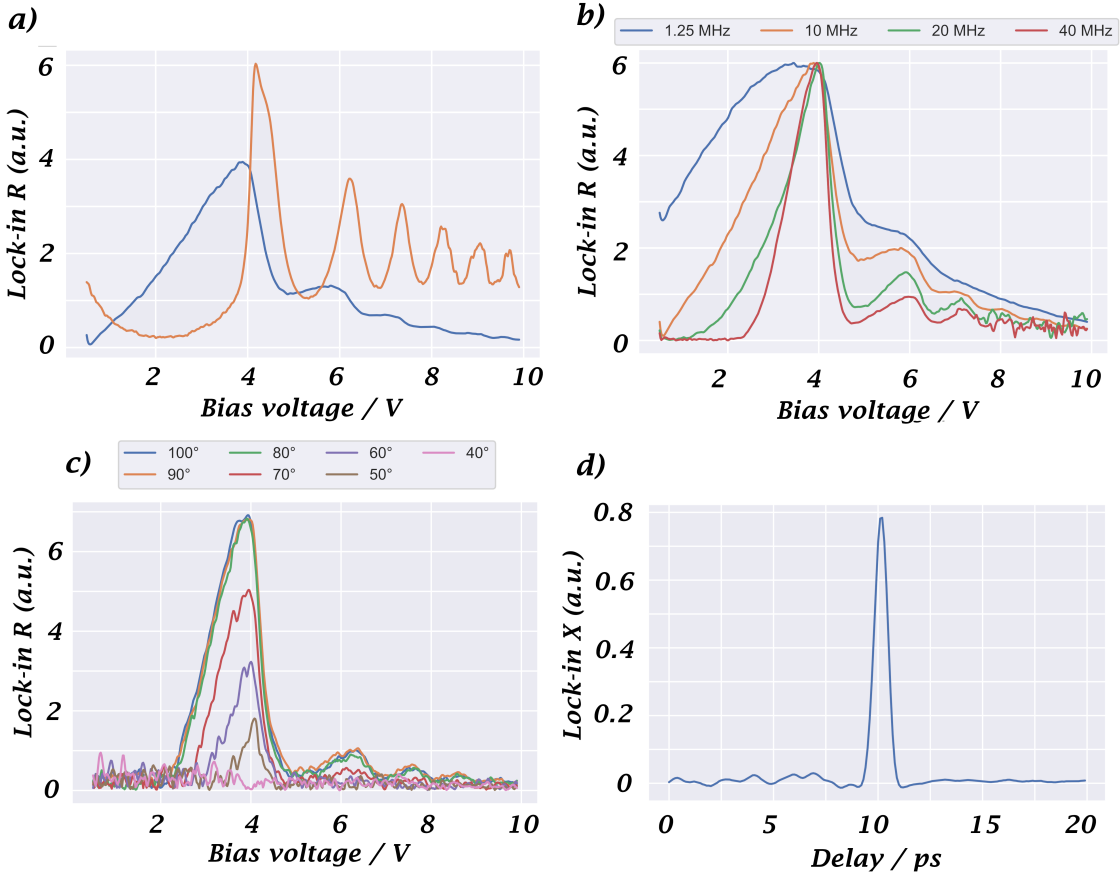
Figure 5.17: **a**) Usual dI/dV (orange) and THz lock-in (blue) signal. One clearly sees the THz induced signal following the field emission resonances. The difference in onset of the first peak is a measure of the THz amplitude (red). Recorded at 10 MHz rep. rate. Current set point 2 nA. **b**) THz lock-in spectra at different repetition rates, normalized to peak signal. As expected, the THz amplitude clearly reduces with the decreasing pump pulse energy associated with higher repetition rates. Due to the extraordinary non-linearity, the signal-noise ratio is higher for higher repetition rates. Current set point 2nA. **c**) THz lock-in spectra at different wire-grid polarizer positions. The THz peak power is continuously tunable using this device. Current set point 2 nA. **d**) THz-THz lock-in spectra as a function of delay. The correlation of the two THz pulses illustrate that the THz pulses act on ultrafast timescales in the tunneling junction. Recorded at 2.7 V, 1nA setpoint, laser at 10 MHz rep. rate. All spectra were recorded with one THz pump beam chopped below 1kHz, lock-in time constant 500 ms. All measurements were performed in constant-current mode.

5.3.2   Sampling via THz Autocorrelation

While our THz-STM is supposed to be operated at cryogenic temperatures, up until here only the FER experiments were performed under these conditions. Hence no data about the crucial pulse duration in the cold STM and the junction at tunneling distances was available. While unlikely, a change in pulse duration and hence achievable time resolution might have occurred. Involved mechanisms could be near-field antenna effects or changes in the optical properties of the windows due to the dramatic change in temperature. In order to be fully convinced our sub-picosecond time resolution is in fact available under our desired measurement conditions, another experiment needed to be performed: THz-THz autocorrelation using the already examined FER.

To do so, we again recorded a FER spectrum. We then set the STM to a bias voltage energetically slightly below the point where the THz lock-in signal starts to rise. We opened the second THz beam of which we made sure it roughly induces the same voltage as the first one. We then proceeded to record the THz lock-in signal as a function of the THz delay-stage position roughly around the temporal overlap position determined in section 5.2.2 via photoelectron-emission.

And indeed close to the known delay stage position a significant signal arose (fig. 5.17d). When both pulses overlap in time, their voltages add up and the FER channel becomes available for tunneling leading to a marked rise in tunneling current, recorded in our lock-in signal. Without knowing the exact near field pulse form of our THz radiation were not able to exactly quantify the voltage or duration of our pulses. Nevertheless, this data provides an easy way for a good estimate of the duration of the positive half-cycle of our THz pulses, which is the relevant part for the achievable time resolution: Since we chose the DC bias such that the voltage of a single THz pulse is just not enough to generate a THz lock-in signal, every additional voltage overlapping with the maximum of said single pulse leads to a signal. So while the intensity of the signal of our two THz pulses delay measurement is difficult to interpret, its width is a good approximation for the duration of the main positive half-cycle of our single THz pulse and hence for the achievable time resolution.

In our measurement we read of a signal width of about FWHM 750 fs, loosely corresponding to the duration for our THz pulse. While we cannot assume to have the same temporal pulse shape as in the electro-optic sampling (sec. 5.1.5) or the photoemission (5.2.2 experiments, at least the duration of the main half-cycle deduced via autocorrelation is well compatible with the sub-ps duration estimated using these two techniques. Hence, while it is of course just a very vague approximation, this two THz-pulse FER experiment gives confidence that our THz-STM still operates on ultrafast timescales when used under the desired cryo conditions and with a junction at tunneling distances.

At this point we reached the second milestone: Using the strong non-linearity of the FER, we were able to show that we can include THz pulses yielding a significant transient voltage into a STM junction at tunneling distances and cryo temperatures. The stability of the

system was at most slightly influenced and still high enough to perform STS measurements. By adding a second THz pulse we were able to verify that the THz induced voltages are indeed on ultrashort timescales under measurement conditions. With this we have basically proven that our THz-STM is operational. For practical purposes and before it can be confidently used on different physical system, one crucial milestone remains: Beating the noise level in true tunneling settings. We will tackle this challenge in the following section.

5.4 Coupling THz Radiation to the STM: Tunneling Regime

In the last section we have proven our THz-STM to be functional using field emission resonances as nonlinearity. We were able to show that under cryo condition and with the tip at tunneling distances we can indeed measure a current caused by the voltage induced by our ultrafast THz pulses. While one might be tempted to claim success in construction of a THz-STM at this point there is actually one more crucial prove to be made.

While we have successfully demonstrated a THz induced current at tunneling distances, field emission resonances are strictly speaking not a tunneling phenomenon. They are more closely related to a field emission. Furthermore we have not yet spatially scanned the sample and hence made only little use of the available high spatial resolution. Since scanning and tunneling are, as the name suggests, at the heart of STM, generating a THz induced current with an actual tunneling event is the necessary last milestone of our construction process. This is more than merely a syntactic problem though: The nonlinearity of the FER is exceptionally strong making comparatively large currents easily achievable. True tunneling nonlinearities are typically far weaker or more limited in their width. Even though the signals detected up until here were already small, they were still rather easily detected. This might be untrue for realistic THz-STM signals based on tunneling processes.

Furthermore, the stability requirement for spatial constant-height maps are a lot stricter than for merely recording a spectrum. A working THz-STM needs to be capable to still do so, which we did not demonstrate up until here. In this chapter we hence try to prove we are still able to beat the noise level in a more realistic tunneling setting and have the stability to make use of the high spatial resolution of STM.

5.4.1 THz-Induced Tunneling through Kondo Resonances

A nice testing system for this is the Kondo resonance located at sulfur vacancy point defects in monolayer molybdenum disulfide on Au(111) (see sec. 4.2.1). This system has been thoroughly studied in our group and is hence rather accessible. Furthermore, on the one hand the Kondo effect causes a rather small signal making it a suitable testing scenario for real-world applications. Additionally, it is highly localized on the the defects and hence showcases the spatial capabilities of our experiment. On the other hand it is a zero bias resonance located inside the bandgap of the MoS_2. This is keeping the background current

(and its noise) low making the selection of the target feature relatively easy.

We hence prepared a defectuous MoS_2 system using the procedure described in section 4.2.1. Via scanning we identified isolated defects located inside large MoS_2 areas and performed STS on them. By this means we identified defects with marked Kondo resonances. After being convinced plenty suitable defects exists, we turned on one THz beam. Since the width of the Kondo resonance is small, we aimed for a small voltage modulation as well and were hence able to comfortably choose the 40 MHz repetition rate setting on the laser. After thermal equilibration we positioned the tip over a suitable defect and recorded THz lock-in spectra: And indeed the Kondo resonance was clearly visible as feature centered around zero bias in the THz-induced current(fig. 5.18a): The signal in the THz lock-in signal started to appear at the onset of the Kondo peak in normal dI/dV and ends shortly after the resonance, corresponding to the small THz amplitudes in use. It crossed zero close to the peak maximum, when the signal of both THz half-cycles averages out to zero net additional current. We were hence clearly able to show that we are able to detect the additional tunneling current caused by the ultrafast transient THz bias in the tunneling regime on small and extremely local nonlinearities such as the Kondo resonance. Having reached this final milestone we can comfortably claim having successfully build a THz-STM!

Since we showed that we can clearly detect the THz response of the probe beam, we can pump a system of interest and expect to be able to record a time-dependent response on the picosecond timescale - if there is one. Sadly this is not expected to be the case for our Kondo resonances. We therefore, after a quick THz-THz pump-probe measurement showed, as predicted, no time-dependent signal, moved on to showcase a final capability of our THz-STM: As described in the beginning of this chapter the stability requirements of a spatial constant-height map far outreach those of a simple constant height spectrum. In the following we want to show that our system is able to fulfill those requirements and hence can not only be used for highly local spectra, but for time dependent spatial map measurements as well in the future.

As already stated in section 4.2.1, the Kondo resonance is spatially localized in a characteristic double kindey shape. We hence proceeded to record a constant height map at a characteristic point in the THz lock-in spectrum (7.5 mV), while shining THz into the junction, recording not only the usual dI/dV signal, but the THz lock-in signal as well. The resulting THz lock-in map (fig. 5.18d) clearly shows the expected shape of the Kondo resonance (fig. 5.18d) and resembles the normal dI/dV map recorded in parallel (fig. 5.18c). The topographic symmetry of the defect measured at a higher bias (fig. 5.18b) is clearly different, giving confidence that the THz-lock-in signal actually arises due to the Kondo resonance and not a broad electronic response. No obvious tip changes, crashes or other signal disturbances occurred during the measurement. This clearly shows that our THz-STM indeed has sufficient stability to record spatial maps of the THz-induced current for at small signals, further broadening the potential applications!

86
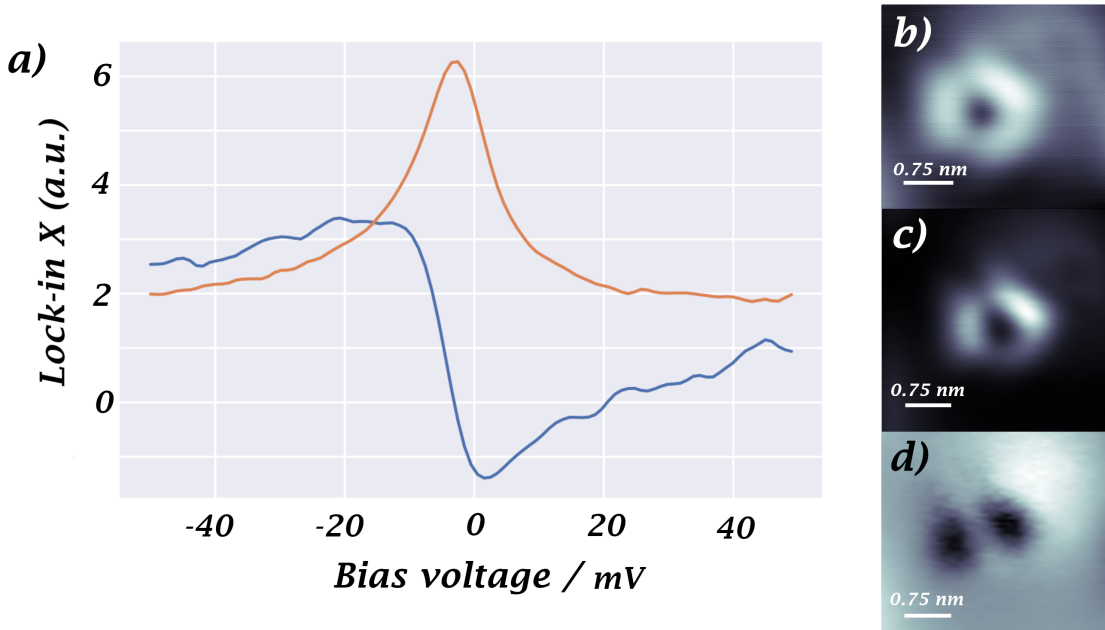
Figure 5.18: **a**) Usual dI/dV (orange) and THz lock-in (blue) signal. One can clearly see the THz-induced signal corresponding to the Kondo resonance as expected. Feedback opened at 6mV, 2nA. Lock-in modulation below 1kHz, time constant 100 ms. **b**) Topography of the defect under investigation. Recorded at 100mV, 100pA. **c**) A dI/dV map of Kondo resonance shows the known double kidney shape. Constant height, 7.5mV, feedback opened at 2nA over the defect. **d**) THz lock-in map showing the same distinct shape as in (c), proving the spatial capabilities of our THz-STM. Measured in parallel to (**c**)

In this chapter we finally performed the last confirmatory experiments proving we indeed succeeded in building a THz-STM and showcasing its capabilities. We have hence reached the goal of this thesis and can now look for systems with interesting locally time-dependent physics knowing that we have a measurement device ready to reliably access it.

PRELIMINARY RESULTS & OUTLOOK

At the core of this thesis is the construction of a THz-STM. In the previous chapters we explained the theoretical framework and the building of such a system before thoroughly testing it to prove its functionality and capabilities. We of course directly wanted to apply our new device to a physical system. The results from these measurements are not yet understood, nevertheless we want to present some preliminary data in this thesis. Furthermore want to give a short outlook on potential future research ideas we consider investigating using our new THz-STM. In the following we will hence quickly discuss some of these systems and why they might be of interest and show some preliminary data.

6.1 Planned Experiments and Preliminary Data: Dynamics on MoTe$_2$

Semiconducting systems are of high interest for THz-STM applications. Their electronic bandgap allows for marked optical excitations changing the band occupation or leading to spatially confined bound states between electrons and holes - the so-called excitons. Depending on the system their lifetime can be very short or rather long e.g. reaching well into the μs regime for pristine silicone [147]. Exciton lifetime is not only of fundamental interest though, but also directly relevant for technological applications: E.g. the efficiency of organic cells is directly linked to the lifetime and mobility of these excitons [148].

Due to the potentially strong interaction of excitons with the lattice, their mobility and lifetime can be strongly influenced by lattice defects. For example, it has been shown that lattice defects can play an important role in exciton dynamics in MoS$_2$ [149] on a macroscopic scale. But the direct role of these defects in the behavior of electronic excitations can, naturally, only be studied on local and ultrafast timescales, a regime accessible by

THz-STM!
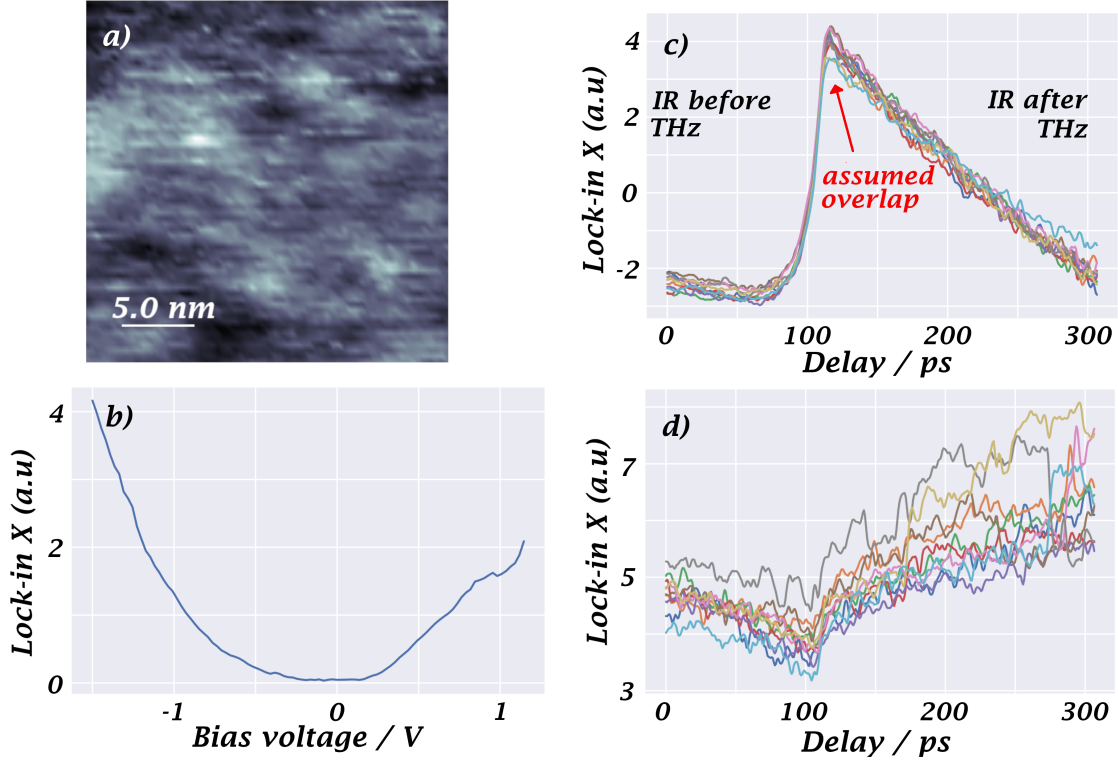
Figure 6.1: Preliminary experimental observations on MoTe$_2$ suggest it being a promising system for our THz-STM. **a**) STM topography of a MoTe$_2$ bulk crystal cleaned in vacuum via adhesive tape cleaving. While reproducible structures are clearly visible, further improvements in quality are necessary for classification of the features. Scanned with 1V, 1nA. **b**) dI/dV spectrum on MoTe$_2$ illustrating the semiconducting gap. Feedback opened at 1.2V, 300pA. **c**) 10 sweeps of a THz lock-in spectra with an IR pump, delay with arbitrary zero. For large delay values the THz pulse arrives before the IR pulse, while it is the other way round for small values. A time dependent feature is clearly and reproducibly visible around the assumed temporal crossing point (red arrow). Recorded with constant current mode at 1V, 1nA. Thz pump beam chopped below 1kHz. **d**) The otherwise same spectra recorded at a DC bias of -1.1V show a less pronounced feature at the same delay value. The difference could either be related to physical reasons in the sample material or to the asymmetry of our THz pulses.

As mentioned before, there is a strong history of TMDC research in our group. It would

therefore be of high interest to us to investigate such a system. Unfortunately, our usual configuration of a TMDC monolayer on a noble metal substrate will probably not be suitable here: The direct interaction with the metal as well as the direct bandgap of mono-layer MoS_2 will likely prevent long-lived excitons. An alternative would hence to use a bulk TMDC.

For another TMDC, molybdenum ditelluride, Yoshida et al. already made first observations on the lifetime of photoexcitations [139] in one of the few other THz-STM groups - without further looking at defects. Due to its indirect band gap, they found fairly long exciton lifetimes with signals still observable after hundredth of picoseconds. Though, their THz-STM is not able to be cooled below room temperature, strongly limiting their capabilities especially regarding accessing the defects. We would hence be very interested in further investigating such a system with the capabilities of our cryo THz-STM. In fact, we already had a first look: We acquired a commercial $MoTe_2$ sample [150] and brought it into our preparation chamber. Via adhesive tape cleaving, we prepared a clean sample and transferred it into the STM. On this first try, we had problems identifying clear topographic features such as defects in the topography, although the sample was easily scanable and clearly showed some kind of reproducible structure(fig. 6.1a). This might well be due to the absence of defects that could easily be introduced later, but could hint at other problems, e.g. insufficient cleaning, as well. Further research is necessary here. We still proceeded to record dI/dV (fig. 6.1b) clearly showing the gap, but otherwise exhibiting strong spatial variance.

Ultimately we would of course be interested in observing a time-dependent process. Since, as discussed above, it has already been shown that IR photoexcitation leads to a process on the desired timescale at room temperature, we decided to perform a quick test and repeated the experiment performed by Yoshida et al., but at cryo temperatures [139]: We shone an IR pump and a THz probe into the junction and recorded the THz lock-in signal as a function of the delay between pump and probe. And indeed a strong time-dependent signature was recorded (fig. 6.1c-d). While it was entirely expected that, due to the possible temperature dependence of exciton dynamics, the measured lifetime would be very different in our case as compared to Yoshida et al., we were not able to fully understand the recorded data. This is further complicated as we can only assume the position of temporal overlap from comparison with electro-optics sampling data (assumed position marked in fig. 6.1c), but might well be off by a bit. There is clearly a reproducible exponential process visible, which is starting at the assumed temporal overlap with positive delay between IR-pump and THz probe and lasting for slightly more than 100ps. This might in principle be associated with the desired charge carrier excitations. Its shape is by now less clear to us though. The process does not quite fit the expected behavior: We would have expected a nearly instantaneous photoexcitation and an exponential decay back to baseline. But we actually seem to have recorded a rather slow and exponential excitation

process with no clear tendency to return to baseline on the recorded timescales. To be able to interpret the exact nature of this data, further measurements are necessary: Calibrating temporal overlap using the known photoemission experiments (see sec. 5.2.2 will help ensuring where the desired signal starts. Spatial variance calls for more data points to map the feature to the STM topography, bias- and distance-dependent measurements as well as using different pump-fluences and observing the changes in the duration of the process, will hopefully unravel its origin. Beside exciton dynamics, we could imagine a direct influence of the strong electric fields on the local band structure.

There is more unclear behavior in the recorded data though, albeit not in the range where we are actually looking for a signal: A strong slope is visible before temporal zero. In contrast to the rather reproducible main-feature described above, the exact slope is less reproducible and it is likely to be some kind of undesired background response of the system. While in principle a non-exact alignment of the delay-stages might be at fault, we tried to exclude this by using different stages for pump and probe, both giving very similar slopes, and several realignments. We are hence rather confident, that this is not the origin of the behavior. A possible explanation would be the thermal response of the tip, which is known to happen on timescales of hundredth of nanoseconds in response to infrared pulses [13, 151]. The fluence-dependent measurements proposed above might be of use in this case as well.

So, while further research is needed to understand the recorded data, it clearly shows that there are time-dependent processes accessible by our THz-STM in this system. Beside being the first time-dependent data recorded using our THz-STM and hence again proving its functionality, this further strengthens our interest in our system and more experiments will be performed in the near future, especially focusing on possible spatial dependence of the signal close to defects.

6.2   Hydrogen on Monolayer Molybdenum Disulfide

It is known that hydrogen (H_2) can be driven to an oscillating motion in an STM junction by a voltage [152] It is hence plausible that using a THz-THz pump probe experiment, such a motion could be tracked. To make sure the small signal is accessible by the THz probe, we made a quick test preparation: We dosed H_2 molecules on a Au(111) sample and recorded dI/dV spectra and THz lock-in spectra (fig. 6.2). A signal consisting of two symmetric dips around zero bias was detected in the dI/dV spectra. This signal is the well-known fingerprint of a bistable hydrogen motion [152–154]. In the THz lock-in data, a strong matching signal was detected: At zero bias, the signal is zero, since the ultrafast THz bias averages over both dips. The extrema are aligned with the them.

Since this signal is accessible to us, we are confined that detection of dynamics might be possible in the future, e.g. in dependence of local changes in the substrate or in combination with an AFM signal.

Recently, it has come to our attention, that first findings of H_2 dynamics in a THz-STM have been published [155]. These findings reinforce our interest in this kind of systems and we are looking forward to further analyze systems based on hydrogen-oscillations.
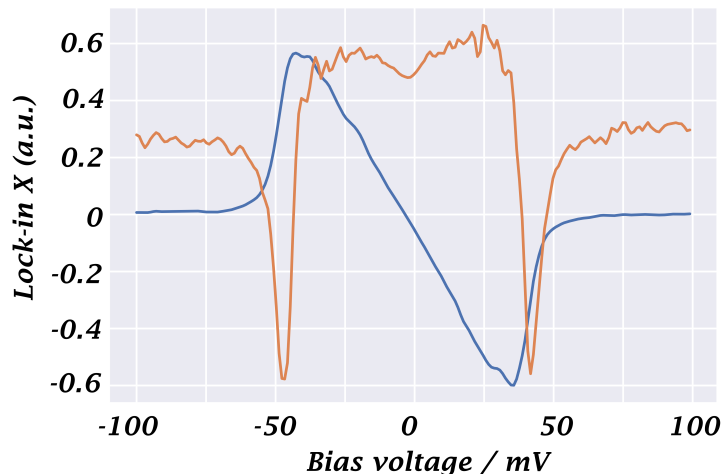

Figure 6.2: Spectra of a H_2 on monolayer MoS_2 on an Au(111) sample. The typical H_2 resonances are readily visible in the dI/dV (orange). They were accessible with an excellent SNR in the THz lock-in measurements (blue). Feedback opened at 7.5mV, 200pA. THz beam chopped below 1 kHz

6.3 Molecular and Atomic Adsorbates

Molecular or atomic adsorbates have been systems of great interest in the STM community for a long time in a broad range of projects. While direct adsorbation on a metal is likely to push the relevant timescales below our detection level, thin isolation layers, such as MgO, NaCl or a TMDC, can lead to a sufficient decoupling. It has e.g. been shown that spin excitations can be directly observed as inelastic tunneling events in magnetic adsorbates on such decoupling layers [108]. For example, some rare earth adatoms are known to lead to a large spin excitation signatures on graphene on iridium [156]. In the future we would like to investigate the dynamics of similar systems, e.g. using the well-established MoS_2 as isolation layer hosting dysprosium adatoms. A spin polarized tip will most likely be necessary to generate a contrast between the different spin states, as is the case in ESR-STM, which is needed to achieve a time resolved signal.

Beside the inelastic steps in the tunneling current associated with spin excitations, localised spins can lead to Kondo resonances, which only form below a certain characteristic tem-

perature. A planned research project would include destroying the Kondo resonance via laser pulse heating and measuring its local reformation characteristics.

Investigating such atomic and molecular magnetism on the ultrafast timescales accessible via THz-STM would be a major goal in our future work.

Beside spin excitations, there are far more processes in adsorbates occurring at ultrafast timescales. One of the most relevant ones to THz-STM is molecular vibration. Already very early THz-STM publications were able to observe the ultrafast motion of a vibrating molecule [69]. In our group we were able to show the strong decoupling properties of MoS_2 regarding vibrational modes [101]. We would hence like to record the motion of molecular adsorbates on ultrafast timescales in such a system. Since an operational OPA is already included in our setup, photoexcitation of molecular states would be another interesting approach.

6.4 Overcoming Limits - a Second Setup

Having learned what is crucial in building a THz STM, we also realized several limiting factors throughout this thesis. One of the most important one is the complex geometry of our preexisting STM. It prevented us to install optics directly on the head and forced us to use relatively large windows made from less optimal materials.

Recently another commercial STM was installed in a new laboratory. This time, the new system is already optimized for THz access featuring parabolic mirrors directly on the STM head. An identical laser has recently been delivered and we plan to copy the existing setup in the near future. First tests using the new STM, without any optics, suggest the possibility to operate a THz-STM below the critical temperature of lead.

If further tests during the installation of the new systems confirm this, a broad range of extremely interesting physics would be accessible. To name just a few, Josephson junctions operate at intrinsic frequencies in the GHz to THz regime and could hence potentially be driven coherently by THz radiation. Using such junctions in an STM has been shown by several groups in the past and our group as well has first experiences [65]. We hence have a good fundamental knowledge how to work with such a system.

Furthermore the superconducting gap can be used to strongly isolate electronic states and increase their lifetime. Combined with the high energy resolution possible thanks to superconducting tip and sample, many sharp resonances with picosecond lifetimes become available for investigation. A first testing system could be the dynamics of the single particle states caused by magnetic impurities: Shiba states. There is broad experience with those states in the group, which would make them an ideal and well controlled system to start into ultrafast local superconductor physics.

CHAPTER 7

SUMMARY AND CONCLUSION

In this thesis we presented the process of designing and building and characterizing our version of a THz-STM. This complex technique has only been recently introduced [1] and uses a combination of ultrashort THz pulses and the high spatial resolution of STM to facilitate ultrafast and local electronic measurements using a pump-probe scheme. After a fundamental theoretical introduction and presenting the lab preparation, we hence firstly discussed the steps involved towards setting up our THz source based on tilted-pulse-front pumping in LN. We presented our calculations of an appropriate combination of specifications for the non-linear crystal, telescope and transmission grating in order to efficiently operate this scheme. We then proceeded to describe the setup process of said source. Notably, we split the beam of our 1030nm, 50W fiber laser system into two and used a delay line to generate two temporally independent pump pulses in preparation for the planned pump-probe experiments. Using this setup and the well-known tilted pulse front pumping scheme [123] we were able to generate THz radiation in the frequency range slightly below 1THz with an average power of over 15mW at 1.25MHz rep. rate.

Since ultrashort pulses are crucial for the operation of a THz-STM, we recorded their temporal shape as a first characterization step. Using electro-optic sampling, we confirmed our pulses to be largely single-cycle and of ultrashort nature with a half-cycle duration of about 640 fs. They were hence found to be ideal for the use in a THz-STM.

After having build a suitable THz source enabling measurements on ultrafast timescales, we needed to prepare for coupling the pulses to an STM in order to facilitate the desired spatial resolution. We hence proceeded to discuss the performed modifications of our pre-existing standard Createc Beetle type 4K STM. This mainly involved creating an optical access. Due to many different small structures in the STM head, that could potentially obstruct the beam path, the construction turned out to be quite delicate. We finally settled to couple in the radiation under an 12.5° angle. To do so we introduced a z-cut quartz window on the

vacuum chamber and constructed a Zeonex window into the nitrogen radiation shield of the cryostat. Both materials allow THz and optical radiation to be transmitted. Furthermore a Zeonex lens was brought into the Helium radiation shield. Its focal length was chosen such that it directly focuses incoming radiation on the tip. Finally we modified the STM head to remove obstructing elements. These modifications raised the base temperature of the STM, but it stayed below 10K allowing it to still perform experiments at very low temperatures. With the STM being prepared we were then finally able to shine THz radiation into the STM junction.

Before claiming to have successfully build a THz-STM, we needed to convince ourselves of the capabilities of our system. In the following sections we hence presented the performed characterization and optimization process along three milestones: Firstly we introduced short-lived free photoelectrons into the STM junction by irradiation with 515nm laser pulses (generated via frequency-doubling) following the approach of [72]. Due to the high thermal load of these experiments, they were performed at room temperature and μm scale junctions. The generated photoelectrons were accelerated by the electric field of the THz pulses present in the junction at the time of their creation. The resulting current was recorded using a lock-in technique. By varying the delay between THz and 515nm pulse we recorded the temporal shape of the THz radiation in the STM. Using this data we were able to not only prove that THz pulses successfully enter the STM junction. We showed as well that, even after passing several transmissive elements and experiencing local field enhancement at the tip apex, our THz pulses still exhibit the necessary single-cycle line shape with an ultrafast pulse duration of below 1 ps.

After having shown that we successfully introduced an ultrafast transient bias voltage to our STM, we needed to proceed to cryo temperature and junctions at tunneling distances. In the following section we hence presented our results regarding the second milestone: Operating the THz-STM at cryo temperature and using junctions at tunneling distances. Using the non-linearity of field emission resonances on a noble metal sample, we were able to demonstrate the capability of our system to stably operate under those conditions. In correlation experiments using two THz pulses, we again demonstrated the ultrashort timescales of the involved processes.

Finally we were able to showcase our THz-STM to be fully operational by discussing the experiments performed regarding the third milestone: Using the highly localized Kondo resonances of point defects in MoS_2 monolayers on Au(111), we demonstrated that we are able to detect the desired tiny additional currents caused by the transient THz voltage under realistic tunneling conditions. We furthermore presented spatially resolved data using this signal, showcasing the stability of our system and highlighting its capabilities for future applications.

Having an operational THz-STM available, we began taking first steps towards using our system to investigate novel time-resolved spatially confined physics. As final experimental data, we presented preliminary results of lifetime measurements of photoexcitation in a $MoTe_2$ bulk crystal at cryo temperatures, trying to reproduce room-temperature data

presented by [139]. While the results are not yet understood, they clearly demonstrate the capabilities of our system to access ultrafast processes in a STM! We finally closed this thesis with an outlook on some of the many planned research projects using this potent new measurement technique we can now use in our lab.

To summarize, within the framework of this thesis we were able to successfully introduce the complex and only recently invented technique of THz-STM to our lab and characterize the constructed system. Using its extraordinary combination of high temporal and spatial resolution, we are looking forward to successfully investigating a broad range of previously inaccessible physics in the near future.

[1] T. Cocker et al. "An ultrafast terahertz scanning tunnelling microscope." In: *Nature Photonics* 7 (2013), pp. 620–625. DOI: `10.1038/nphoton.2013.151`.

[2] E. G. Richards. *Mapping Time : The Calendar and Its History.* 1999. Chap. 9–10. ISBN: 9780198504139.

[3] R. Wendorff. *Tag und Woche, Monat und Jahr: Eine Kulturgeschichte des Kalenders.* VS Verlag fur Sozialwissenschaften, 1993. Chap. Einleitung.

[4] Dava Sobel. "Brief history of early navigation." In: *Johns Hopkins Apl Technical Digest* 19 (1998), pp. 11–13.

[5] S. Berryman. "Democritus." In: *The Stanford Encyclopedia of Philosophy (Winter 2016 Edition).* `plato.stanford.edu/archives/win2016/entries/democritus/`. 2016.

[6] "Atomic Theory." In: *Encyclopedia Britannica.* `britannica.com/science/atomic-theory`; Accessed 08/22. 2022.

[7] John Thomas. "Centenary: The birth of X-ray crystallography." In: *Nature* 491 (2012), pp. 186–7. DOI: `10.1038/491186a`.

[8] G. Binnig and H. Rohrer. "Scanning tunneling microscopy." In: *Surface Science* 126.1 (1983), pp. 236–244. DOI: `https://doi.org/10.1016/0039-6028(83)90716-1`.

[9] G. Nunes and M. Freeman. "Picosecond Resolution in Scanning Tunneling Microscopy." In: *Science (New York, N.Y.)* 262 (1993), pp. 1029–32. DOI: `10.1126/science.262.5136.1029`.

[10] Y. Terada et al. "Laser-combined scanning tunnelling microscopy for probing ultrafast transient dynamics." In: *Journal of physics; Condensed matter* 22 (2010), p. 264008. DOI: `10.1088/0953-8984/22/26/264008`.

[11] M. Rashidi et al. "All-electronic Nanosecond-resolved Scanning Tunneling Microscopy: Facilitating the Investigation of Single Dopant Charge Dynamics." In: *J. Vis. Exp.* 131 (2018), e56861. DOI: 10.3791/56861.

[12] R. Hamers and D. Cahill. "Ultrafast time resolution in scanned probe microscopies." In: *Applied Physics Letters* 57.19 (1990), pp. 2031–2033. DOI: 10.1063/1.103997.

[13] M. Garg et al. "Ultrafast Photon-Induced Tunneling Microscopy." In: *ACS Nano* 15.11 (2021), pp. 18071–18084. DOI: 10.1021/acsnano.1c06716.

[14] S. Grafström. "Photoassisted scanning tunneling microscopy." In: *Journal of Applied Physics* 91.4 (2002), pp. 1717–1753. DOI: 10.1063/1.1432113.

[15] W. Demtröder. *Experimentalphysik 3*. Springer Berlin, 2016, p. 116–121. ISBN: 978-3-662-49094-5.

[16] D. Rolf. "Fundamental Properties of Atoms and Molecules on Surfaces." PhD thesis. Freie Universitaet Berlin, 2019. DOI: 10.17169/refubium-1514.

[17] J. Bardeen. "Tunnelling from a Many-Particle Point of View." In: *Phys. Rev. Lett.* 6.2 (1961), pp. 57–59. DOI: 10.1103/PhysRevLett.6.57.

[18] C. Chen. *Introduction to Scanning Tunneling Microscopy: Second Edition*. Oxford Univ. Press, 2007. ISBN: 978-0-1992-1150-0.

[19] S. Lounis. *Lecture notes: Theory of Scanning Tunneling Microscopy*. 2014. DOI: 10.48550/ARXIV.1404.0961.

[20] S. Lounis. *Lecture notes: Theory of Scanning Tunneling Microscopy*. p. 7–9. 2014. DOI: 10.48550/ARXIV.1404.0961.

[21] J. Tersoff and D. R. Hamann. "Theory of the scanning tunneling microscope." In: *Phys. Rev. B* 31.2 (1985), pp. 805–813. DOI: 10.1103/PhysRevB.31.805.

[22] C. Chen. *Introduction to Scanning Tunneling Microscopy: Second Edition*. Oxford Univ. Press, 2007. Chap. 2.2.2. ISBN: 978-0-1992-1150-0.

[23] C. Chen. *Introduction to Scanning Tunneling Microscopy: Second Edition*. Oxford Univ. Press, 2007, p. 152–159. ISBN: 978-0-1992-1150-0.

[24] J. Scofield. "Frequency-domain description of a lock-in amplifier." In: *American Journal of Physics* 62.2 (1994), pp. 129–133. DOI: 10.1119/1.17629.

[25] Zurich Instruments. *White Paper Principles of lock-in detection and the state of the art Zurich Instruments Release*. zhinst.com/sites/default/files/li_primer/zi_whitepaper_principles_of_lock-in_detection.pdf; Accessed 08/22. 2016.

[26] Stanford Research Instruments. *About Lock-In Amplifiers: Application Note 3*. thinksrs.com/downloads/pdfs/applicationnotes/AboutLIAs.pdf; Accessed 08/22.

[27] Xinhua Xie et al. "Attosecond-Recollision-Controlled Selective Fragmentation of Polyatomic Molecules." In: *Phys. Rev. Lett.* 109.24 (2012), p. 243001. DOI: 10.1103/PhysRevLett.109.243001.

[28] J. W. Pomeroy et al. "Phonon lifetimes and phonon decay in InN." In: *Applied Physics Letters* 86.22 (2005), p. 223501. DOI: 10.1063/1.1940124.

[29] M. Dantus et al. "Femtosecond laser observations of molecular vibration and rotation." In: *Nature* 343 (1990), pp. 737–739. DOI: 10.1038/343737a0.

[30] R. Decker et al. "Attosecond-Recollision-Controlled Selective Fragmentation of Polyatomic Molecules." In: *Nature Sci Rep* 9 (2019), p. 8977. DOI: 10.1038/s41598-019-45242-8.

[31] D. Sengupta and T. Sarkar. "Maxwell, Hertz, the Maxwellians, and the early history of electromagnetic waves." In: *Antennas and Propagation Magazine, IEEE* 45 (2003), pp. 13–19. DOI: 10.1109/MAP.2003.1203114.

[32] W. Demtröder. *Experimentalphysik 2*. Springer Berlin, 2009, p. 140 ff. ISBN: 978-3-5406-8219-6.

[33] W. Demtröder. *Experimentalphysik 2*. Springer Berlin, 2009, p. 25–29. ISBN: 978-3-5406-8219-6.

[34] W. Demtröder. *Experimentalphysik 2*. Springer Berlin, 2009, p. 111–119. ISBN: 978-3-5406-8219-6.

[35] W. Demtröder. *Experimentalphysik 2*. Springer Berlin, 2009, p. 267 ff. ISBN: 978-3-5406-8219-6.

[36] W. Demtröder. *Experimentalphysik 2*. Springer Berlin, 2009. Chap. 8.4.3. ISBN: 978-3-5406-8219-6.

[37] W. Demtröder. *Experimentalphysik 2*. Springer Berlin, 2009. Chap. 9.5.2. ISBN: 978-3-5406-8219-6.

[38] "The double-slit experiment." In: *Physics World* 15.9 (2002), p. 15. DOI: 10.1088/2058-7058/15/9/20.

[39] W. Demtröder. *Experimentalphysik 2*. Springer Berlin, 2009. Chap. 10.5.3. ISBN: 978-3-5406-8219-6.

[40] Helge Kragh. "Max Planck: the reluctant revolutionary." In: 13.12 (2000), pp. 31–36. DOI: 10.1088/2058-7058/13/12/34.

[41] Jeff Hecht. "A short history of laser development." In: *Appl. Opt.* 49.25 (2010), F99–F122. DOI: 10.1364/AO.49.000F99.

[42] W. Demtröder. *Experimentalphysik 3*. Springer Berlin, 2016. Chap. 7.1.1. ISBN: 978-3-662-49094-5.

[43] W. Demtröder. *Experimentalphysik 3*. Springer Berlin, 2016. Chap. 8.1. ISBN: 978-3-662-49094-5.

[44] MyNick at Wikimedia Commons. `commons.wikimedia.org/wiki/File:DoubleCladdingFiber.png` and `commons.wikimedia.org/wiki/File:Fiberlaser1.png`; Accessed 08/22.

[45] R. Paschotta. *RP Photonics Encyclopedia: Fiber Lasers*. `rp-photonics.com/fiber_lasers.html`; Accessed 08/22.

[46] R. Paschotta. *RP Photonics Encyclopedia: M2 factor*. `rp-photonics.com/m2_factor.html`; Accessed 08/22.

[47] Gill et al. "RUBY LASER." In: *Science and Education* 12 (2022), pp. 3939–3940. DOI: `10.15680/IJIRSET.2022.1104138`.

[48] M. Eichhorn. *Laserphysik : Grundlagen und Anwendungen für Physiker, Maschinenbauer und Ingenieure*. Springer Spektrum, 2013. Chap. 4.1. ISBN: 978-3-6423-2648-6.

[49] R. Paschotta. *RP Photonics Encyclopedia: Q Switching*. `rp-photonics.com/q_switching.html`; Accessed 08/22.

[50] G. Harigel et al. "Pulse stretching in a Q-switched ruby laser forbubble chamber holography." In: *Appl. Opt.* 25.22 (1986), pp. 4102–4110. DOI: `10.1364/AO.25.004102`.

[51] M. Eichhorn. *Laserphysik : Grundlagen und Anwendungen für Physiker, Maschinenbauer und Ingenieure*. Springer Spektrum, 2013. Chap. 4.2. ISBN: 978-3-6423-2648-6.

[52] W. Demtröder. *Experimentalphysik 3*. Springer Berlin, 2016. Chap. 8.2.4. ISBN: 978-3-662-49094-5.

[53] W. Lamb. "Theory of an Optical Maser." In: *Phys. Rev.* 134 (6A 1964), A1429–A1450. DOI: `10.1103/PhysRev.134.A1429`.

[54] L. Hargrove et al. "LOCKING OF He–Ne LASER MODES INDUCED BY SYNCHRONOUS INTRACAVITY MODULATION." In: *Applied Physics Letters* 5.1 (1964), pp. 4–5. DOI: `10.1063/1.1754025`.

[55] R. Paschotta. *RP Photonics Encyclopedia: Mode Locking*. `rp-photonics.com/mode_locking.html`; Accessed 08/22.

[56] D. Spence et al. "60-fsec pulse generation from a self-mode-locked Ti:sapphire laser." In: *Opt. Lett.* 16.1 (1991), pp. 42–44. DOI: `10.1364/OL.16.000042`.

[57] R. Paschotta. *RP Photonics Encyclopedia: Kerr lens mode locking*. `rp-photonics.com/kerr_lens_mode_locking.html`; Accessed 08/22.

[58] N. Khusnatdinov et al. "Ultrafast scanning tunneling microscopy with 1 nm resolution." In: *Applied Physics Letters* 77.26 (2000), pp. 4434–4436. DOI: `10.1063/1.1336817`.

[59] V. Gerstner et al. "Femtosecond laser assisted scanning tunneling microscopy." In: *Journal of Applied Physics* 88.8 (2000), pp. 4851–4859. DOI: 10.1063/1.1290706.

[60] V. Gerstner et al. "Thermal effects in pulsed laser assisted scanning tunneling microscopy." In: *Journal of Applied Physics* 87.5 (2000), pp. 2574–2580. DOI: 10.1063/1.372221.

[61] O. Takeuchi et al. "Development of Time-Resolved Scanning Tunneling Microscopy in Femtosecond Range." In: *Japanese Journal of Applied Physics* 41 (July 2002), pp. 4994–4997. DOI: 10.1143/JJAP.41.4994.

[62] S. Yoshida et al. "Optical pump-probe scanning tunneling microscopy for probing ultrafast dynamics on the nanoscale." In: *The European Physical Journal Special Topics* 222 (2013). DOI: 10.1140/epjst/e2013-01912-2.

[63] S. Loth et al. "Measurement of Fast Electron Spin Relaxation Times with Atomic Resolution." In: *Science* 329.5999 (2010), pp. 1628–1630. DOI: 10.1126/science.1191688.

[64] P. Tien and J. Gordon. "Multiphoton process observed in the interaction of microwave fields with the tunneling between superconductor films." In: *Physical Review* 129.2 (1963), p. 647.

[65] Olof Peters et al. "Resonant Andreev reflections probed by photon-assisted tunnelling at the atomic scale." In: *Nature Physics* 16 (Dec. 2020), pp. 1–5. DOI: 10.1038/s41567-020-0972-z.

[66] T. Tachizaki et al. "On the progress of ultrafast time-resolved THz scanning tunneling microscopy." In: *APL Materials* 9.6 (2021), p. 060903. DOI: 10.1063/5.0052051.

[67] C. Sirtori. "Bridge for the Terahertz Gap." In: *Nature* 417 (June 2002), pp. 132–3. DOI: 10.1038/417132b.

[68] G. Davies and E. Linfield. "Bridging the terahertz gap." In: *Physics World* 17 (Apr. 2004), pp. 37–41. DOI: 10.1088/2058-7058/17/4/34.

[69] T. Cocker et al. "Tracking the ultrafast motion of a single molecule by femtosecond orbital imaging." In: *Nature* 539 (2016), pp. 263–267. DOI: 10.1038/nature19816.

[70] S. Yoshida et al. "Terahertz Scanning Tunneling Microscopy for Visualizing Ultrafast Electron Motion in Nanoscale Potential Variations." In: *ACS Photonics* 8.1 (2021), pp. 315–323. DOI: 10.1021/acsphotonics.0c01572.

[71] S. Ammerman et al. "Lightwave-driven scanning tunnelling spectroscopy of atomically precise graphene nanoribbons." In: *Nature Communications* 12 (2021), p. 6794. DOI: 10.1038/s41467-021-26656-3.

[72] M. Müller et al. "Phase-Resolved Detection of Ultrabroadband THz Pulses inside a Scanning Tunneling Microscope Junction." In: *ACS Photonics* 7.8 (2020), pp. 2046–2055. DOI: 10.1021/acsphotonics.0c00386.

[73] Y. Luo et al. "Nanoscale terahertz STM imaging of a metal surface." In: *Phys. Rev. B* 102 (20 2020), p. 205417. DOI: 10.1103/PhysRevB.102.205417.

[74] Katsumasa Yoshioka et al. "Real-space coherent manipulation of electrons in a single tunnel junction by single-cycle terahertz electric fields." In: *Nature Photonics* 10 (2016). DOI: 10.1038/nphoton.2016.205.

[75] J. Simmons. "Generalized Formula for the Electric Tunnel Effect between Similar Electrodes Separated by a Thin Insulating Film." In: *Journal of Applied Physics* 34.6 (1963), pp. 1793–1803. DOI: 10.1063/1.1702682.

[76] Nils Krane et al. "Mapping the perturbation potential of metallic and dipolar tips in tunneling spectroscopy on MoS 2." In: *Physical Review B* 100 (2019). DOI: 10.1103/PhysRevB.100.035410.

[77] B. Clough and J. Dai. "Laser Air Photonics: Covering the "Terahertz Gap" and Beyond." In: *Chinese Journal of Physics- Taipei-* 52 (2014), pp. 416–430. DOI: 10.6122/CJP.52.416.

[78] D. Slocum et al. "Atmospheric absorption of terahertz radiation and water vapor continuum effects." In: *Journal of Quantitative Spectroscopy and Radiative Transfer* 127 (2013), pp. 49–63. DOI: 10.1016/j.jqsrt.2013.04.022.

[79] G. Meyer. "A simple low-temperature ultrahig-vacuum scanning tunneling microscope capable of atomic manipulation." In: *Review of Scientific Instruments* 67.8 (1996), pp. 2960–2965. DOI: 10.1063/1.1147080.

[80] specs-group.com/nc/nanonis/products/detail/mimea-base-package-bp5e/.

[81] femto.de/en/products/current-amplifiers/variable-gain-up-to-500-khz-dlpca.html.

[82] zhinst.com/europe/de/products/mfli-lock-amplifier.

[83] techmfg.com/products/cleantopopticaltopsandsupports/performance-series-optical-tables.

[84] Amplitude: Satsuma. amplitude-laser.com/products/femtosecond-lasers/satsuma/.

[85] APE Angewandte Physik und Elektronik GmbH: AVUS. ape-berlin.de/en/opa-optical-parametric-amplifier/.

[86] Thorlabs. thorlabs.com/.

[87] Newport Spectra-Physics. newport.com/.

[88] EKSMA Optics. eksmaoptics.com/.

[89] Edmund Optics. edmundoptics.de/.

[90] Michael Ruby. "SpectraFox: A free open-source data management and analysis tool for scanning probe microscopy and spectroscopy." In: *SoftwareX* 5 (2016). DOI: `10.1016/j.softx.2016.04.001`.

[91] I. Horcas et al. "WSXM: A software for scanning probe microscopy and a tool for nanotechnology." In: *Review of Scientific Instruments* 78.1 (2007), p. 013705. DOI: `10.1063/1.2432410`.

[92] F. Hanke and J. Bjork. "Structure and local reactivity of the Au(111) surface reconstruction." In: *Phys. Rev. B* 87 (23 2013), p. 235422. DOI: `10.1103/PhysRevB.87.235422`.

[93] X. Li and H. Zhu. "Two-dimensional MoS2: Properties, preparation, and applications." In: *Journal of Materiomics* 1.1 (2015), pp. 33–44. DOI: `10.1016/j.jmat.2015.03.003`.

[94] W. Winer. "Molybdenum disulfide as a lubricant: A review of the fundamental knowledge." In: *Wear* 10.6 (1967), pp. 422–452. DOI: `10.1016/0043-1648(67)90187-1`.

[95] Y. Sun et al. "Indirect-to-Direct Band Gap Crossover in Few-Layer Transition Metal Dichalcogenides: A Theoretical Prediction." In: *The Journal of Physical Chemistry C* 120.38 (2016), pp. 21866–21870. DOI: `10.1021/acs.jpcc.6b08748`.

[96] Xiaonan Sun et al. "NaCl multi-layer islands grown on Au(111)-(22x3) probed by scanning tunneling microscopy." In: *Nanotechnology* 19.49 (2008), p. 495307. DOI: `10.1088/0957-4484/19/49/495307`.

[97] W. Paul et al. "Control of the millisecond spin lifetime of an electrically probed atom." In: *Nature Physics* 13 (2016). DOI: `10.1038/nphys3965`.

[98] I. Rau et al. "Reaching the magnetic anisotropy limit of a 3¡i¿d¡/i¿ metal atom." In: *Science* 344.6187 (2014), pp. 988–992. DOI: `10.1126/science.1252841`.

[99] S. Schintke et al. "Insulator at the Ultrathin Limit: MgO on Ag(001)." In: *Physical review letters* 87 (2002), p. 276801. DOI: `10.1103/PhysRevLett.87.276801`.

[100] S. Baumann et al. "Electron paramagnetic resonance of individual atoms on a surface." In: *Science* 350 (2015), pp. 417–420. DOI: `10.1126/science.aac8703`.

[101] N. Krane. "High Resolution Vibronic Spectra of Molecules on Molybdenum Disulfide Allow for Rotamer Identification." In: *ACS Nano* 12 (2018). DOI: `10.1021/acsnano.8b07414`.

[102] S. Grønborg et al. "Synthesis of Epitaxial Single-Layer MoS2 on Au(111)." In: *Langmuir* 31.35 (2015), pp. 9700–9706. DOI: `10.1021/acs.langmuir.5b02533`.

[103] "Moire structure of MoS2 on Au(111): Local structural and electronic properties." In: *Surface Science* 678 (2018), pp. 136–142. DOI: `https://doi.org/10.1016/j.susc.2018.03.015`.

105

[104] F. Tumino et al. "Nature of Point Defects in Single-Layer MoS2 Supported on Au(111)." In: *The Journal of Physical Chemistry C* 124.23 (2020), pp. 12424–12431. DOI: 10.1021/acs.jpcc.0c01477.

[105] B. Schuler et al. "Large Spin-Orbit Splitting of Deep In-Gap Defect States of Engineered Sulfur Vacancies in Monolayer WS 2." In: *Physical Review Letters* 123 (2019). DOI: 10.1103/PhysRevLett.123.076801.

[106] S. Trishin et al. "Moire Tuning of Spin Excitations: Individual Fe Atoms on MoS2/Au(111)." In: *Phys. Rev. Lett.* 127 (23 2021), p. 236801. DOI: 10.1103/PhysRevLett.127.236801.

[107] Markus Ternes. "Probing magnetic excitations and correlations in single and coupled spin systems with scanning tunneling spectroscopy." In: *Progress in Surface Science* 92 (2017), pp. 83–115. DOI: 10.1016/j.progsurf.2017.01.001.

[108] M. Ternes. "Spin Excitations and Correlations in Scanning Tunneling Spectroscopy." In: *New Journal of Physics* 17 (2015), p. 063016. DOI: 10.1088/1367-2630/17/6/063016.

[109] Nathan M. Burford and Magda O. El-Shenawee. "Review of terahertz photoconductive antenna technology." In: *Optical Engineering* 56 (2017), p. 010901. DOI: 10.1117/1.OE.56.1.010901.

[110] T. Papaioannou et al. "THz spintronic emitters: a review on achievements and future challenges." In: *Nanophotonics* 10.4 (2021), pp. 1243–1257. DOI: doi:10.1515/nanoph-2020-0563.

[111] K. Ravi et al. "Theory of terahertz generation by optical rectification using tilted-pulse-fronts." In: *Opt. Express* 23.4 (2015), pp. 5253–5276. DOI: 10.1364/OE.23.005253.

[112] P. Tan et al. "Terahertz radiation sources based on free electron lasers and their applications." In: *SCIENCE CHINA Information Sciences* 55 (2012), pp. 1–15. DOI: 10.1007/s11432-011-4515-1.

[113] Tom S. Seifert et al. "Spintronic sources of ultrashort terahertz electromagnetic pulses." In: *Applied Physics Letters* 120.18 (2022), p. 180401. DOI: 10.1063/5.0080357.

[114] J. Fulop et al. "Towards generation of mJ-level ultrashort THz pulses by optical rectification." In: *Opt. Express* 19.16 (2011), pp. 15090–15097. DOI: 10.1364/OE.19.015090.

[115] Robert W. Boyd. "Chapter 1 - The Nonlinear Optical Susceptibility." In: *Nonlinear Optics (Third Edition)*. Academic Press, 2008, pp. 1–67. ISBN: 978-0-12-369470-6.

[116] R. Paschotta. *RP Photonics Encyclopedia: Mode Locking.* rp-photonics.com/optical_rectification.html; Accessed 08/22.

[117] Steven Byrnes at Wikimedia Commons. `https://commons.wikimedia.org/wiki/File:Electron_asymmetric_motion_animation.gif`; Accessed 08/22. 2014.

[118] X. Zhang et al. "Terahertz optical rectification from a nonlinear organic crystal." In: *Applied Physics Letters* 61.26 (1992), pp. 3080–3082. DOI: `10.1063/1.107968`.

[119] L. Arizmendi. "Photonic applications of lithium niobate crystals." In: *physica status solidi (a)* 201.2 (2004), pp. 253–283. DOI: `https://doi.org/10.1002/pssa.200303911`.

[120] L. Palfalvi et al. "Nonlinear refraction and absorption of Mg doped stoichiometric and congruent LiNbO3." In: *Journal of Applied Physics* 95.3 (2004), pp. 902–908. DOI: `10.1063/1.1635993`.

[121] M. Nakamura et al. "Optical Damage Resistance and Refractive Indices in Near-Stoichiometric MgO-Doped LiNbO3." In: *Japanese Journal of Applied Physics* 41 (2002). DOI: `10.1143/JJAP.41.L49`.

[122] L. Palfalvi et al. "Temperature and composition dependence of the absorption and refraction of Mg-doped congruent and stoichiometric LiNbO3 in the THz range." In: *Advanced Solid-State Photonics* (2005), WB4. DOI: `10.1364/ASSP.2005.WB4`.

[123] J. Hebling et al. "Generation of high-power terahertz pulses by tilted-pulse-front excitation and their application possibilities." In: *Journal of The Optical Society of America B-optical Physics - J OPT SOC AM B-OPT PHYSICS* 25 (2008). DOI: `10.1364/JOSAB.25.0000B6`.

[124] `refractiveindex.info/?shelf=main&book=LiNbO3&page=Zelmon-o`;Accessed 08/22.

[125] W. Demtroeder. *Experimentalphysik 4.* Springer Berlin, 2017. Chap. 4.3.5. ISBN: 978-3-662-52884-6.

[126] Matthias C Hoffmann and Jozsef Andras Fueloep. "Intense ultrashort terahertz pulses: generation and applications." In: *Journal of Physics D: Applied Physics* 44.8 (2011), p. 083001. DOI: `10.1088/0022-3727/44/8/083001`.

[127] J. Hebling et al. "Velocity matching by pulse front tilting for large area THz-pulse generation." In: *Optics express* 10 (2002), pp. 1161–6. DOI: `10.1364/OE.10.001161`.

[128] X. Wu et al. "Highly efficient generation of 0.2 mJ terahertz pulses in lithium niobate at room temperature with sub-50 fs chirped Ti:sapphire laser pulses." In: 26.6 (2018), pp. 7107–7116. DOI: `10.1364/OE.26.007107`.

[129] H. Hirori et al. "Single-cycle terahertz pulses with amplitudes exceeding 1 MV/cm generated by optical rectification in LiNbO3." In: *Applied Physics Letters* 98.9 (2011), p. 091106. DOI: `10.1063/1.3560062`.

[130] Oxide Corporation. `opt-oxide.com/products/prism/`; Accessed 08/22.

[131] J. A. Fülöp et al. "Design of high-energy terahertz sources based on optical rectification." In: *Opt. Express* 18.12 (2010), pp. 12311–12327. DOI: 10.1364/OE.18.012311.

[132] Q. Wu and X. Zhang. "Free-space electro-optic sampling of terahertz beams." In: *Applied Physics Letters* 67.24 (1995), pp. 3523–3525. DOI: 10.1063/1.114909.

[133] Robert W. Boyd. "Chapter 11 - The Electrooptic and Photorefractive Effects." In: *Nonlinear Optics (Third Edition)*. Academic Press, 2008, pp. 511–541. ISBN: 978-0-12-369470-6.

[134] C. Riek et al. "Femtosecond measurements of electric fields: from classical amplitudes to quantum fluctuations." In: *European Journal of Physics* 38.2 (2017), p. 024003. DOI: 10.1088/1361-6404/aa53a2.

[135] M. Nagai et al. "Generation and detection of terahertz radiation by electro-optical process in GaAs using 1.56um fiber laser pulses." In: *Applied Physics Letters* 85.18 (2004), pp. 3974–3976. DOI: 10.1063/1.1813645.

[136] Tydex THz materials. tydexoptics.com/products/thz_optics/thz_materials/.

[137] C. Davies et al. "Temperature-Dependent Refractive Index of Quartz at Terahertz Frequencies." In: *Journal of Infrared, Millimeter, and Terahertz Waves* 39 (2018). DOI: 10.1007/s10762-018-0538-7.

[138] L. Wimmer et al. "Terahertz control of nanotip photoemission." In: *Nature Physics* 10 (2014), pp. 432–436. DOI: 10.1038/nphys2974.

[139] S. Yoshida et al. "Subcycle Transient Scanning Tunneling Spectroscopy with Visualization of Enhanced Terahertz Near Field." In: *ACS Photonics* 6.6 (2019), pp. 1356–1364. DOI: 10.1021/acsphotonics.9b00266.

[140] G. Derry et al. "Recommended values of clean metal surface work functions." In: *Journal of Vacuum Science & Technology A* 33.6 (2015), p. 060801. DOI: 10.1116/1.4934685.

[141] M. Bionta et al. "Laser-induced electron emission from a tungsten nanotip: Identifying above threshold photoemission using energy-resolved laser power dependencies." In: *Journal of Modern Optics* 61 (2013). DOI: 10.1080/09500340.2013.846432.

[142] D. Nikogosyan. "Beta barium borate (BBO)." In: *Applied Physics A* 52 (1991), pp. 359–368. DOI: 10.1007/BF00323647.

[143] W. Su et al. "Field enhancement factors and self-focus functions manifesting in field emission resonances in scanning tunneling microscopy." In: *Nanotechnology* 27 (2016), p. 175705. DOI: 10.1088/0957-4484/27/17/175705.

[144] K.H. Gundlach. "Zur berechnung des tunnelstroms durch eine trapezfoermige potentialstufe." In: *Solid-State Electronics* 9.10 (1966), pp. 949–957. DOI: 10.1016/0038-1101(66)90071-2.

[145] O.Yu. Kolesnychenko et al. "Field-emission resonance measurements with mechanically controlled break junctions." In: *Physica B: Condensed Matter* 291.3 (2000), pp. 246–255. DOI: 10.1016/S0921-4526(99)02884-7.

[146] K. Zhou et al. "Transmittance of high-density polyethylene from 0.1 THz to 15 THz." In: *Proc. SPIE* 111960Y (2019), p. 33. DOI: 10.1117/12.2534490.

[147] R. Hammond and R. Silver. "Temperature dependence of the exciton lifetime in high-purity silicon." In: *Applied Physics Letters* 36 (1980), pp. 68–71. DOI: 10.1063/1.91277.

[148] A. Classen et al. "The role of exciton lifetime for charge generation in organic solar cells at negligible energy-level offsets." In: *Nature Energy* 5 (2020), pp. 1–9. DOI: 10.1038/s41560-020-00684-7.

[149] H. Shi et al. "Exciton Dynamics in Suspended Monolayer and Few-Layer MoS2 2D Crystals." In: *ACS Nano* 7.2 (2013), pp. 1072–1080. DOI: 10.1021/nn303973r.

[150] HQ Graphene. http://www.hqgraphene.com/MoTe2.php.

[151] C. Guo et al. "Probing Nonequilibrium Dynamics of Photoexcited Polarons on a Metal-Oxide Surface with Atomic Precision." In: *Phys. Rev. Lett.* 124 (20 2020), p. 206801. DOI: 10.1103/PhysRevLett.124.206801.

[152] C. Lotze et al. "Driving a Macroscopic Oscillator with the Stochastic Motion of a Hydrogen Molecule." In: *Science (New York, N.Y.)* 338 (2012), pp. 779–82. DOI: 10.1126/science.1227621.

[153] J. Gupta et al. "Strongly coverage-dependent excitations of adsorbed molecular hydrogen." In: *Phys. Rev. B* 71 (11 2005), p. 115416. DOI: 10.1103/PhysRevB.71.115416.

[154] A. Halbritter et al. "Huge negative differential conductance in Au-H2 molecular nanojunctions." In: *Physical Review B* 77 (2007). DOI: 10.1103/PhysRevB.77.075402.

[155] L. Wang et al. "Atomic-scale quantum sensing based on the ultrafast coherence of an H2 molecule in an STM cavity." In: *Science (New York, N.Y.)* 376 (2022), pp. 401–405. DOI: 10.1126/science.abn9220.

[156] M. Pivetta et al. "Measuring the Intra-Atomic Exchange Energy in Rare-Earth Adatoms." In: *Phys. Rev. X* 10 (3 2020), p. 031054. DOI: 10.1103/PhysRevX.10.031054.

Ich erkläre gegenüber der Freien Universität Berlin, dass ich die vorliegende Dissertation selbstständig und ohne Benutzung anderer als der angegebenen Quellen und Hilfsmittel angefertigt habe. Die vorliegende Arbeit ist frei von Plagiaten. Alle Ausführungen, die wörtlich oder inhaltlich aus anderen Schriften entnommen sind, habe ich als solche kenntlich gemacht. Diese Dissertation wurde in gleicher oder ähnlicher Form noch in keinem früheren Promotionsverfahren eingereicht. Mit einer Prüfung meiner Arbeit durch ein Plagiatsprüfungsprogramm erkläre ich mich einverstanden.

ACKNOWLEDGMENTS

Working on a research project and writing a PhD-thesis is nothing that happens just on your own. Many people are involved in supporting such an endeavour. As this thesis would not have been possible without them, I would like to take the chance and thank them for their support!

First of all I would like to thank my supervisor Prof. Dr. Katharina Franke. Obviously without you, this project would not have been possible. Beside hosting it in your working group and labs, your relentless support and broad experience made it possible to tackle the scientific challenges on the way. No less important, the wonderful working atmosphere you have created in your working group makes it easy to deal with personal challenges on the way. I really could not have wished for a better supervisor and am very happy having joined you five years ago for my Master thesis. You allowed me to work on a very complex, new (and expensive) project for my PhD and trusted me to decide on my own how to approach it. This gave me the freedom to grow on this project and the confidence that I will make it work in the end - even when it did not look like it in the moment. This is really not a given and I am very grateful for recieving this chance. And anyway, thank you for being the friendly and cheerful person you are! It has been a great pleasure working for you!

Secondly, I want to thank my second supervisor and co-PI of the project: Tobias Kampfrath: Your expertise in THz-physics is incredible and without it I would not have even known where to start. Thank you for supporting me with theoretical and practical knowledge, for always being there on short nice when discussion was necessary and for giving the project the time it needed. And as for Katharina: Thank you for entrusting me with such a complex project. I remember many "aha"-moment you made possible. Thank you also for guiding me to the right members of your group, who supported me in many ways. Firstly, I would like to thank Tom Seifert, whose unsurpassed optical lab expertise sparked many new approached during the construction and whose door was always open to quickly

discuss an approach. Thank you as well to Yannic Behovits, Oliver Gückstock and Heitz for helping me with many specific THz questions! I know it is once a while difficult to keep the update-rate high when working in two different groups and being busy with different projects, teaching and so on and I for sure not always succeeded in it. But I am very grateful it always came back up when needed!

Of course this project was carried out in the working group of Prof. Franke and many of its members supported it on a daily basis. First, I would like to thank Dr. Christian Lotze. You know basically everything about STMs and basically instant-fixed every problem I could come up with. Also, thank you for just being great to work with, humorous and becoming a friend along the way! Chris will take over the THz-STM after I leave, so I can go assured that it is in good hands. Secondly, I would like to thank the PhD-student on the SFB project: My office mate and best friend Sergey Trishin. We have known each other since the very beginning of our academic journey and I do not even want to imagine how much less fun it would have been and how much less competent I would have become without you. I am very happy we then decided to work together as well and will always remember these years (and all the ones to come). Thank you for helping out a lot on the laser project and learning together with me how to operate optics... it would have been very lonely and impossible to understand otherwise. Furthermore I want to thank all the groups members, present and former, that made the journey so delightful and helped me learn a lot. It is impossible to name them all here, so I will just go with a selected few: Thank you, Olof Peters, for supervising my Master project and hence laying the foundation for my entrance into the world of experimental physics and STM. It has been a great pleasure! Thank you, Laetitia Farinacci, for not only always being open to discuss and having great ideas, but also for being one of the most fun persons to be around with I know! Thank you, Marc Westig, Idan Tamir, Gael Reecht and Nils Krane for sharing your expertise and being so lighthearted! And lastly, I would like to thank Verena Caspari for saving many rounds of Güntherwhen it already seemed lost. ;).

Last not least I would like to thank my family and friends for supporting me on a personal level and bearing with me even in the more stressful times. Firstly, my wonderful wife Jarmila Bogdanoff. Beside helping out directly during writing with many tips and reading all of it, without your level of emotional support (and kicking me when being lazy) I would never have succeeded. You are wonderful and I love you a lot!
I would like to thank my parents, Birgit and Peter Bogdanoff, as well as my sister Kira. Beside putting up with a lot of shared stress as well, thank you for making me who I am! The same goes for my grandparents, of whom sadly only my beloved grandmother Vera Schöbel could still directly witness this project.
Thank you to my friends Katharina L., Tim H., Max K., Max L., Selma B., Pauline B. for always sticking around, even when I dived away for a year again. And thanks to all those I could not or forgot to mention here!